DIGITAL ACCESS TO SCHOLARSHIP AT HARVARD
DASH.HARVARD.EDU

HARVARD LIBRARY
Office for Scholarly Communication

Wetting in Color

Citation
Burgess, Ian Bruce. 2012. Wetting in Color. Doctoral dissertation, Harvard University.

Permanent link
http://nrs.harvard.edu/urn-3:HUL.InstRepos:9876056

Terms of Use
This article was downloaded from Harvard University's DASH repository, and is made available under the terms and conditions applicable to Other Posted Material, as set forth at http://nrs.harvard.edu/urn-3:HUL.InstRepos:dash.current.terms-of-use#LAA

Share Your Story

The Harvard community has made this article openly available.
Please share how this access benefits you. Submit a story .

Accessibility

© 2012 – Ian Bruce Burgess
all rights reserved

Wetting in Color

Abstract

Colorimetric litmus tests such as pH paper have enjoyed wide commercial success due to their inexpensive production and exceptional ease of use. However, expansion of colorimetry to new sensing paradigms is challenging because macroscopic color changes are seldom coupled to arbitrary differences in the physical/chemical properties of a system. In this thesis I present in detail the development of Wetting in Color Technology, focusing primarily on its application as an inexpensive and highly selective colorimetric indicator for organic liquids. The technology exploits chemically-encoded inverse-opal photonic crystals to control the infiltration of fluids to liquid-specific spatial patterns, projecting minute differences in liquids' wettability to macroscopically distinct, easy-to-visualize structural color patterns. It is shown experimentally and corroborated with theoretical modeling using percolation theory that the high selectivity of wetting, upon-which the sensitivity of the indicator relies, is caused by the highly symmetric structure of our large-area, defect-free SiO_2 inverse-opals. The regular structure also produces a bright iridescent color, which disappears when infiltrated with liquid − naturally coupling the optical and fluidic responses. Surface modification protocols are developed, requiring only silanization and selective oxidation, to facilitate the deterministic design of an indicator that differentiates a broad range of liquids. The resulting tunable, built-in horizontal and vertical chemistry gradients allow the wettability threshold to be tailored to specific liquids across a continuous range, and make the readout rely only on countable color differences. As wetting is a generic fluidic phenomenon, Wetting in Color technology could be suitable for applications in authentication or identification of unknown liquids across a broad range of industries. However, the generic nature of the response also ensures chemical non-specificity. It is shown that combinatorial measurements from an array of indicators add a degree of chemical specificity to the platform, which can be further improved by monitoring the drying of the inverse-opal films. While colorimetry is the central focus of this thesis, applications of this platform in encryption, fluidics and nanofabrication are also briefly explored.

Table of Contents

Title Page……i

Abstract……iii

Table of Contents……..iv

Citations to Previously Published Work……...vi

Acknowledgements……..vii

1. Introduction.……..……..……1

1.1. Background……1

1.2. Overview of Wetting in Color technology…….…...6

2. Developing a Scheme for Colorimetry, Part 1: The Selectivity Limits…….....17

2.1. Structural disorder and selectivity……...19

2.2. Modeling the optical response to partial filling……...21

2.3. Selectivity and long-range variability……..27

3. Developing a Scheme for Colorimetry, Part 2: Optimization and Tuning……...28

3.1. Non-destructive quality control……...28

3.2. Continuous tuning of the response……..……..29

3.3. Vertical gradients of wettability……..……..31

3.4. Selective deconstruction to guide the eye……37

4. Enhancing Chemical Specificity……..……39

4.1. The problem of chemical interference……39

4.2. Enhanced specificity with arrays……40

4.3. Drying in color: Further differentiation of liquids based on volatility……49

5. Discussion: Opportunities, Limitations, and Extended Applications……...60

5.1. Outlook: Sensing……..60

5.2. Extended applications……..……65

5.3. Planar lithography on porous surfaces (PLOPS)……68

6. Conclusions and Outlook……...76

6.1. Conclusions.....76

6.2. Suggestions for future studies……..78

Appendix A. Detailed Experimental Techniques……81

A.1. Fabrication of defect-free inverse opals……..81

A.2. Spatially patterning the surface chemistry for encryption (Chapter 1)……...85

A.3. Imaging of wetting interfaces…….86

A.4. Functionalization procedures for Chapters 2&3…….88

A.5. Methods for combinatorial Wetting in Color (Chapter 4)…….89

Appendix B. Mathematical and Numerical Methods…….92

B.1. Principal component analysis (for Chapter 4)…….92

B.2. Numerical percolation simulation……...93

Bibliography……101

Citations to Previously Published Work

Portions of Chapters 1 and 5 have appeared in the following publication:

I.B. Burgess, L. Mishchenko, B.D. Hatton, M. Kolle, M. Lončar, J. Aizenberg, "Encoding complex wettability patterns in chemically functionalized 3D photonic crystals," *Journal of the American Chemical Society* **133**, 12430-12432 (2011).

Portions of Chapters 2, 3, 4, and 5, have appeared in the following publication:

I.B. Burgess, N. Koay[*], K.P. Raymond[*], M. Kolle, M. Lončar, J. Aizenberg, "Wetting in color: Colorimetric Differentiation of Organic Liquids with High Selectivity", *ACS Nano* **6**, 1427-1437 (2012).

Portions of Chapter 4 have appeared in the following publication

K.P. Raymond[*], I.B. Burgess[*], M.H. Kinney[*], M. Lončar, J. Aizenberg, "Combinatorial wetting in colour: An optofludic nose", *Lab on a Chip*, DOI:10.1039/C2LC40489C (2012).

Portions of Chapter 2 discussing optical modeling of partially wetted photonic crystals, portions of Chapter 4 discussing drying in inverse-opals and portions of Chapter 5 covering planar lithography on porous surfaces are presently unpublished, but likely to be included in one or more academic publications in the future.

Acknowledgements

I think the most important advice that I received early on in my career with respect to choosing a PhD project was, “The advisor is more important than the project.” I could not have asked for more from an advisor than I received from Prof. Marko Lončar. From the first day I joined his group, Marko made sure I knew that he was very approachable – the type of person who is genuinely interested in everything that is troubling you, even if it is not the experiment you are currently working on. Over the course of the last four years I have developed the type of working relationship with Marko in which I feel comfortable asking his advice about anything and as a result, I feel his contribution to my personal development has extended far beyond the lab. After four years in Marko’s group, I feel like I have developed a firm grasp on my area of research as well as a more general notion of how one participates in the research community and designs a research program. Most importantly my enjoyment of my research has monotonically increased throughout the course of my PhD. One only has to meet a handful of upper year graduate students (or read PhD comics) to know that in general we can be known as a pretty depressed and discouraged group of people. I feel very fortunate to still have the enthusiasm for my PhD that I had on my first day. This is an attitude that I find disproportionately echoed by other members of the Lončar group and I think it is because we are supported by such an approachable, attentive and dedicated mentor.

I am also very fortunate to have received so much guidance from Prof. Joanna Aizenberg, who became a second-advisor to me. I am grateful that she adopted me to her group, treating me as one of her own, and making herself available to give me guidance both in and beyond the lab. She constantly challenged me and exposed me to a broad range of topics. Her sometimes eclectic, curiosity driven approach to science really inspired me to think outside the box and have more fun doing research, and is a quality I hope to emulate in my future endeavors. I also thank my committee members, Profs Federico Capasso and Steven G. Johnson, for thoughtful and constructive comments on my project at important stages of its development.

I am grateful to all of the students and postdocs from the Lončar and Aizenberg groups who have helped me over the last four years and created a friendly working environment. I thank Dr. Murray McCutcheon, Yinan Zhang, and Lidiya Mishchenko for putting up with my raw, unguided enthusiasm in the beginning and getting me on my feet in the labs. In particular, thank you Lidiya for putting up with my mess at the bench. I am grateful to the many other students, postdocs and professors, that I have had the chance to collaborate and interact with and learn from, in particular: Dr. Qimin Quan, Anna Shneidman, Dr. Ben Hatton, Dr. Alejandro Rodriguez, Dr. Tom Babinec, Dr. Parag Deotare, Jennifer Choy, Raji Shankar, Birgit Hausmann, Dr. Daniel Floyd, Dr. Mathias Kolle, Dr. Philseok Kim, Dr. Michael Aizenberg, Dr. Wendong Wang, Dr. Nicolas Vogel, Dr. James Weaver, Dr. Alison Grinthal, Dr. Mughees Khan, Dr. Yolanda Vasquez, Dr. Igor Aharonovitch, Prof. Frans Spaepen, Michael Burek, Haig Atikian, Katherine Phillips, Dr. Nicolas Vogel, and Leonard Kogos. In addition I am grateful for the constant support of our groups' current and former administrative assistants, Marina Di Donato-McLaughlin, Kathy LaFrance, Xiomara Forbez and Hetchen Ehrenfeld.

I owe special gratitude to Kevin Raymond, Natalie Koay, Mackenzie Kinney, and D. Johann Djanal-Mann, the exceptional undergraduate students with whom I have had the privilege to work. They constantly surprised, enlightened, and inspired me with their thoughtful insights and their untainted enthusiasm for science.

I would not even have ended up in graduate school, let alone graduating, if it were not for the excellent mentoring I received from undergraduate research advisors, Prof. Kalaichelvi Saravanamuttu, Dr. Nicolas Cunningham, Dr. Paul Rochon, Dr. Marco Peccianti, Prof. Roberto Morandotti and Prof. James Martin. In particular, I owe tremendous gratitude to Prof. Saravanamuttu for first introducing me to research, allowing me to first work in her group at the age of 17. I would not be where I am today without her thoughtfulness, patience and dedication to my personal and professional development. I am also especially thankful to Dr. Marco Peccianti for patiently teaching me both the fundamentals of optics and scientific computation.

I would not be anywhere close to where I am today without the unending support of my family. My parents, Caroline and Cliff, have played a defining role in my development, providing the type of loving family atmosphere that will always serve as a model for the family I hope to build, introducing me to science at a young age and helping me with my math and physics homework all the way through to senior year of university. My brothers, Andrew, Matthew and Michael, have provided me with an invaluable support network. In particular, I would like to thank Matthew for reading many drafts of my papers and this thesis, and providing very constructive comments from an ecologist's point of view. Finally, I would like thank my wife, Thy, who has been there to support me every step along the way, providing me with unconditional love and companionship, scientific advice when I needed it, and exceptionally good food.

The research presented in this thesis was financially supported by the United States Air Force Office of Scientific Research Multidisciplinary University Research Initiative (MURI) center, called Bio-Inspired Optics: Offering Physical and Technical Insights into Color and Structure (BIOOPTICS), award # FA9550-09-1-0669-DOD35CAP. I also wish to thank the Natural Sciences and Engineering Research Council of Canada for supporting all four years of my studies through the PGS-M and PGS-D fellowships.

Chapter 1. Introduction

1.1. Background

There is a perpetual demand in society for new diagnostic devices, reflecting our never-ceasing thirst for greater knowledge of what is around us, what we are made of, what makes people sick, etc. There are some general performance metrics whose optimization is desired in many sensing platforms, such as sensitivity, selectivity (resistance to false positives), simplicity (ease of use, cost etc.), and broad applicability of a technique or an approach. However, it is difficult to design a sensing platform in which all of these ideals are achieved, as some of these qualities (e.g. sensitivity/specificity, generalizability and simplicity) generally are considered tradeoffs in a given sensor design [1]. Particularly pronounced is the tradeoff between simplicity/cost and all of the performance ideals [2-5]. A practical way to approach the problem of sensor design is to say "Given that I am willing to spend a fixed amount of money, time, and space on a sensing problem; how sensitive/specific can I make a sensor to address that problem?" For every level of simplicity, there is a range of applications (or customers) and a wide range of prior art. For some applications, specificity and sensitivity are paramount and costs are tolerable. Examples of such applications are the analytical components of synthetic chemistry (e.g. pharmaceuticals), high-quality materials synthesis (e.g. semiconductor device technology) and lab-quality biochemical assays (e.g. for disease detection at a hospital) [6-8]. For these problems, many highly sophisticated chemical analysis technologies have emerged, such as high-performance chromatography, mass-spectrometry, optical spectroscopy (FTIR, UV-Vis, etc.), nuclear magnetic resonance spectroscopy, high-resolution optical microscopy, electron microscopy, enzyme-linked immunosorbent assays, etc. [6-8].

On the other hand, what if simplicity or low-cost was the paramount ideal? There are many sensing problems where this is the case, but most importantly, many of these sensing problems are yet to have an elegant solution. In fact, I would argue that this type of optimization currently dominates the field of chemical sensor

development. Some examples of chemical sensing problems of this type are: detection of hazardous compounds in the field (e.g. at home, on the job, on the battlefield or at the airport) [9], medical diagnostics at home or in the developing world [2-5], and authentication or quality-control of consumer products (e.g. food, fuel, drugs. cosmetics, etc.) at home or in the field [10], to name a few. While usually associated with a sacrifice in absolute performance (e.g. sensitivity or specificity), simple and low-cost diagnostic devices can be used both in more places and by more people, specifically by those who do not have sufficient resources and/or training to have access to the most sophisticated diagnostic technologies [2-5].

Colorimetry, where the readout is simply a change in an indicator's color, is a particularly attractive approach to simple, low-cost diagnostics. Colorimetric litmus tests such as pH paper have enjoyed wide commercial success due to their inexpensive production and exceptional ease of use [11-13]. However, expansion of colorimetry to new sensing paradigms is challenging because macroscopic color changes are seldom coupled to arbitrary differences in the physical/chemical properties of a system. For example, the color changes in pH paper are a result of protonation/de-protonation of dye molecules absorbed in the paper [14]. These dye molecules, which display different molecular absorption (and thus color) in the protonated and deprotonated states, can therefore only be used as a basis for colorimetric detection of chemical conditions that would induce protonation or deprotonation. Here, the inherent chemical specificity of the color change is both friend and foe, allowing exceptionally simple and fairly accurate colorimetric determination of the pH of an aqueous solution, but making impossible the generalization of this type of colorimetry to most other types of measurements.

So how do we design a broadly generalizable platform for colorimetry? To do this, first we require a type of color change that can be induced by a very generic, chemically non-specific mechanism. This forms the basis of the approach, one that is common to any desired application and guarantees a colorimetric response. Then we can add a chemically-specific link between this generic color-change mechanism and the desired unknown property or specific analyte, to tailor the generalizable sensing platform to a specific individual sensing problem (e.g. detection of pentaerythritol tetranitrate at airport security).

Exploiting structural color is one promising route to broadly applicable platforms for colorimetry. Structural color is a result of light scattering rather than absorption, and as the name sounds, is derived from the structure of a material rather than its chemical composition [15]. Structural color is particularly pronounced to the eye when the scattering centers (e.g. roughness or porosity) are spaced on the scale of visible wavelengths and have some degree of spatial coherence (order) [15,16]. Structural color is also readily tuned by any mechanism that tunes the structure. This can be done by changes in the size, aspect-ratio, shape, refractive index, or the degree of spatial coherence in the structure or a component thereof [17-33]. These color changes can be induced by changes in the *physical* properties of a material forming the structure. They do not rely on a specific *chemical* state responsible for molecular absorption in a given wavelength region, as was the case with pH paper. Since the color changes are no longer bound to any one specific material or chemical process (the only requirement being that the material is heterogeneous, rough or porous on a scale that is comparable to the wavelengths of visible light), the chemical composition of the material forming the structure is a degree of freedom that can be tailored to impart colorimetric sensing capability to a particular stimulus.

Tunable structural color has been a topic of interest for over a decade, and many applications both in and away from sensing/diagnostics have been explored [17-57]. In fact, the core requirements for colorimetry and tunable color in general are the same: both require a source of color (in this case a wavelength-scale structuring of the material) and a controlled response of the color to a particular stimulus (generally done by making the structure out of a material whose chemical properties are tuned such that changes in its shape, density, volume, etc. are tied to the target stimulus). Having the chemical and material properties forming a structurally-colored system as a versatile degree of freedom has facilitated the development of systems whose color responds to a wide range of stimuli [17-57].

One of the simplest ways to impart dynamic character onto a structurally-colored material is by infiltration. This can be due to solvent swelling (causing a change in size) or filling of sub-wavelength porosity in the material (causing a change in density or effective refractive index), induced by either direct contact with a liquid [30,53,55] or by vapor adsorption [34,35,48,49,52]. Structurally colored materials based on hydrogels

(weakly cross-linked polymers that can reversibly expand and contract in aqueous media by absorbing or expelling liquid), can be engineered to have tunable color that responds to any stimulus that can induce its volume phase-transition [38,39,41,44-47,50,51,56]. Using hydrogels with wavelength-scale structure, researchers have been able to generate structurally colored materials whose color can tune in response to changes in pH [38,41], humidity [52], electric fields [46,47] and temperature [45]. Tunable color based on hydrogel swelling can also be tailored to respond to the presence of specific dissolved species (glucose, metals, small-molecule biological metabolites, etc.) [38,39,44,50,51]. Multifunctional hydrogels can also be synthesized to produce structural color that can tune in response to more than one of the above stimuli [56]. Color based on structured elastomeric materials is readily tuned by applying mechanical strain and can be used for pressure sensing or even color-fingerprinting [27,40,54]. Structural color can also be tuned by inducing movement of scatterers. For example, the use of magnetic particles as a basis for coherent light-scattering facilitates color that is tunable by magnetic fields, which move the particles [32]. The addition of functional biomolecules as deformable defects in a structurally colored material has also been used to make colorimetric biosensors [57].

While there exist a vast range of functional materials upon which a platform for dynamic structural color can be built (outlined in the above paragraph), equally essential to the design of such a platform is a means to impart wavelength-scale structure to these materials. While there are several routes to such structuring [16,22,58], colloidal crystal templating is by far the most widely used method, owing to its versatility, simplicity and scalability [20-26]. In this approach, a wavelength-scale periodic structure is formed by the self-assembly of monodisperse colloidal particles from a suspension into a close-packed lattice. Monodisperse suspensions of colloidal microshperes are most commonly made of polystyrene (PS), polymethylmethacrylate (PMMA), or silica with sphere diameters that can be readily controlled from synthesis conditions to be anywhere in the range from tens of nanometers to several microns, allowing the color (due to the wavelength-region of strongest Bragg reflection) of the structure to be tuned [20-26]. This self-assembly process can be induced in a variety of ways (e.g. sedimentation, centrifugation, evaporation, confinement etc.) [20]. Once the colloidal crystal is formed, the addition of functional material can be done by infiltrating the interstitial sites of the close-packed arrays. After

infiltration, the original colloidal crystal template can be removed (either by chemical etching or pyrolysis), leaving behind an inverse-opal. This can be done either to increase the refractive-index-contrast, or to open up porosity in the structure [20].

This thesis describes the development of Wetting in Color technology, a versatile platform for structural colorimetry to identify liquids based on highly selective wetting in defect-free inverse-opal films (IOFs). Our IOFs are fabricated by a colloidal co-assembly technique developed by Hatton et al. [59], producing silica IOFs that are exceptionally ordered and crack-free over cm-scales. The scheme of colorimetry is made possible by two main advances described in detail here: 1) The first is the discovery that IOFs display a remarkably sharply-defined threshold wettability for liquid infiltration. This threshold was investigated in detail and was found to be a function of the structure and regularity of the pore geometry. Its sharply-defined nature allows very subtle differences in liquid composition to produce macroscopically different filling behavior in IOFs (e.g. one fills the pores, while the other does not, leaving air-filled pores), which is naturally coupled to the film's color, owing to vastly different refractive-index contrast between air-filled and liquid-filled porosity. 2) The second is the development of a variety of techniques to functionalize the porous IOFs with highly controlled and spatially diverse surface chemistry. This allows the wettability threshold in different regions of an IOF to be tuned to specific liquids. Thus, upon liquid immersion, the pores of these structurally-colored films are selectively infiltrated in a unique spatial pattern – creating an optical fingerprint of that liquid through the color contrast between wetted and non-wetted regions.

Using these advances, the Wetting in Color platform was optimized for use as an inexpensive and highly selective colorimetric indicator for organic liquids. Its performance is analyzed and optimized with respect to the metrics outlined at the beginning of this chapter. With this colorimetric platform, cost, simplicity and portability come easy, as does the breadth of sensing problems for which it can potentially be applied. The latter owes to the fact that the fundamental stimulus for sensitivity is wettability, a generic property that exists for all liquids. These are considered the advantages of the Wetting in Color platform over other sensing options, and effort to preserve

these qualities is maintained throughout the optimization of the other performance metrics (e.g. sensitivity, specificity, etc.), as detailed in the proceeding sections.

1.2. Overview of Wetting in Color technology

"Un appareil révolutionnaire qui est le fruit d'une long collaboration entre les 'scientists' de la NASA et celles de Canadian Tire" – Têtes à Claques

Defect-Free Inverse-Opal Films in SiO_2

The core topic covered by this thesis is the control of wetting in defect-free inverse-opal photonic crystals [59] and, in turn, control of the structural color, referred-to collectively as Wetting In Color technology. While the development of the colloidal co-assembly process to fabricate these inverse-opal films (IOFs) was done prior to my PhD work and is outside the scope of this thesis, it is worth briefly summarizing the key elements of the process and the properties of the films to provide the reader with context. Also included in Appendix A is the detailed experimental procedure that I used to make these films, to ensure that a reader would have all of the necessary information in this thesis alone to reproduce any of the experimental work presented here. A detailed characterization of this fabrication technique can be found in Ref. [59] as well as in Lidiya Mishchenko's PhD thesis (Harvard University, School of Engineering and Applied Sciences, 2012).

IOFs used in this work are made of SiO_2 and are templated via colloidal co-assembly. The highly regular porosity of the inverse-opal structure also serves as a source of color (due to constructive interference from reflections off the close-packed air pores). An outline of the fabrication procedure is as follows: A solution of hydrolyzed tetraethoxysilane (TEOS) (a sol-gel precursor solution to SiO_2) is added to an aqueous suspension of monodisperse polymethylmethacrylate (PMMA) microspheres (d~300nm). This mixture is then allowed to evaporate while containing a vertically-suspended oxidized silicon substrate. The evaporating composite solution leaves behind a close-packed (face-centered cubic) lattice of the polymer spheres with a silica gel matrix filling up the interstitial sites [59]. The polymer template is removed at high temperature (500°C) in air, leaving behind the final IOF structure. IOFs grown by this colloidal co-assembly technique possesses some unique properties

that make them ideal for the applications explored here. Namely, the structure is highly uniform, can be crack-free over cm-scales (they are also single-orientation, with the (110)-growth direction strongly favored), and is flat over large areas with open porosity exposed at the top surface, lacking a silica over-layer [59]. The IOF structure is shown in Fig. 1.

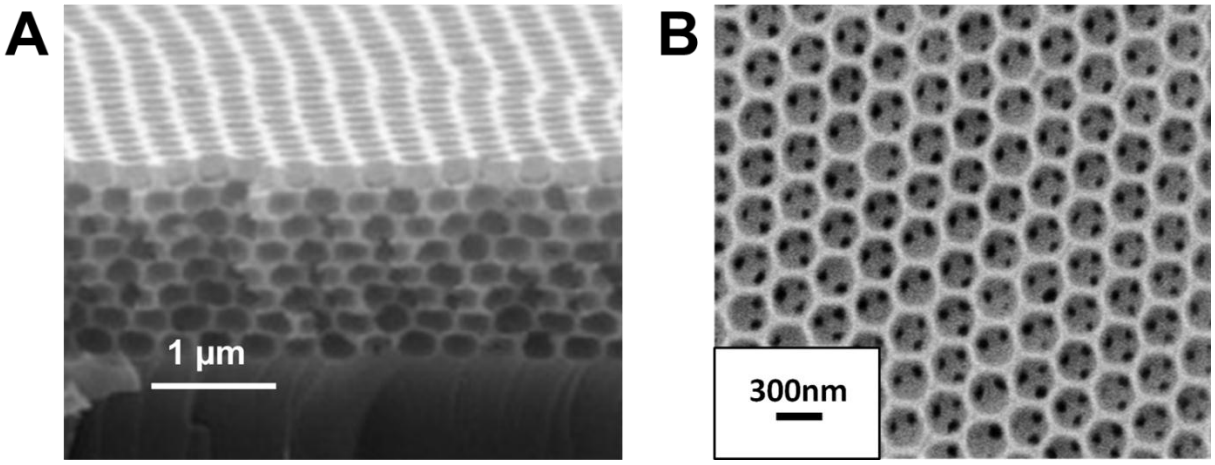

Figure 1. Scanning electron micrographs of inverse-opal films grown by colloidal co-assembly [59]. A: Side view, B: top view, also showing the small necks connecting the spherical pores.

Encoding of Wettability in Inverse-Opal Films

Owing to the scale of their periodic porosity, IOFs display brightly iridescent color. Throughout the work discussed in this thesis, the color displayed by a porous IOF is tuned simply by filling the pores with a fluid. The effect of fluid-filling on the color and normal-incidence reflection spectrum is shown in Fig. 2. A redshifting of the principal reflectance peak is expected as the optical path-length of periodicity increases with the increased refractive index inside the pores. However, the more dramatic effect is a diminishing of the reflectance maximum, with the film becoming nearly transparent. This is evident in Fig. 2B, where the color of the IOF appears visibly indistinguishable from the bare silicon substrate. This increased transparency of the IOF is caused by the approximate refractive-index matching of the sol-gel silica matrix and most common liquids (n ~ 1.3-1.4). While high-quality silica has n = 1.46, the silica that makes up our IOFs is expected to have a slightly lower refractive

index. Spectral measurements (presented in Chapter 3) suggest that IOFs are perfectly index-matched to polydimethylsiloxane (PDMS, $n \sim 1.4$). Thus, wetting of an IOF is coupled with a macroscopic change in the film's color.

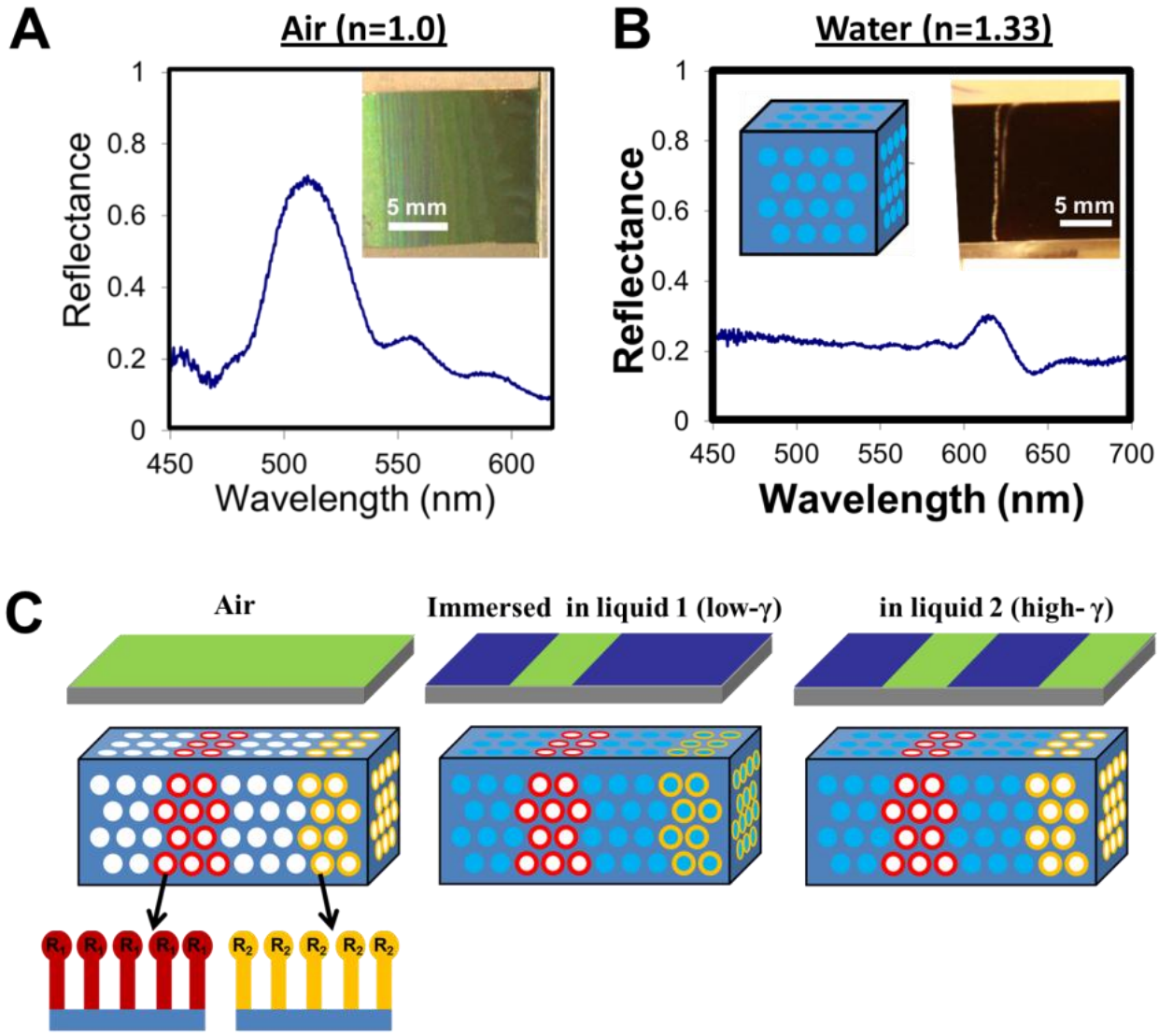

Figure 2. (A) Photograph (inset) and normal-incidence reflection spectrum of an IOF in air. (B) Photograph and normal-incidence reflection spectrum of an IOF (in a hydrophilic state) after immersion of the film in water (the pores are filled). (C) Schematic depicting the core principle of operation of the devices described in this thesis. If different regions of an IOF are locally functionalized with different surface groups, different liquids may penetrate selectively only certain regions, but not others, revealing an optical contrast pattern in the process.

Suppose now that we could selectively functionalize an IOF such that different surface moieties were locally attached to the pore surfaces in different regions, giving each region a different wettability of the pores to a given liquid. When such an IOF was exposed to a liquid (e.g. water), one might expect that the pores in some of the functionalized regions will become filled, but not others (shown schematically in Fig. 2C). It is well known that, when submerged in water, porous structures with sufficiently low surface energies can resist the infiltration of the liquid into the pores. In fact, recently, spatial patterning of hydrophilicity has been used to manipulate the flow of water in three-dimensional porous networks [5,60], a promising approach to simple and inexpensive fluidic and diagnostic devices. Since liquid-filling in the case of our IOFs is tied to a macroscopic color change, exposure of such a functionalized IOF to a liquid could reveal a previously-invisible color pattern. With more than two functionalized regions, multiple liquids (having different surface tensions, for example) could penetrate different combinations of regions, producing different patterns (shown schematically in Fig. 2C).

We developed techniques to encode complex wettability patterns into the pores of IOFs. All variants of the functionalization procedure used in this thesis rely on two core processes: i) exposure to alkylchlorosilane vapor to deposit organic surface groups, and ii) exposure to oxygen plasma to etch organic surface groups and re-oxidize the silica surfaces. Silica is a very convenient material to work with for these studies because of the widespread commercial availability of alkylchlorosilanes with a wide variety of pendant groups. Fig. 3 shows a functionalization protocol that produces the type of multilevel wettability pattern shown in Fig. 2C. The entire IOF structure is first functionalized by exposure to vapors of an alkylchlorosilane bearing a functional group, R_1. This R_1 surface functionality is then locally erased and the surface re-activated by exposing the porous inverse opal to oxygen plasma through a removable mask [61]. As a mask, we used slabs of cured PDMS that were sealed to the surface under slight pressure and peeled off after the exposure without damaging the structure. Exposing the selectively oxidized structure to the vapors of a second alkylchlorosilane bearing a functional group, R_2, now adds a new functionality to surface sites that were not protected by the mask in the previous step. Further plasma-etching through a different mask produces a pattern that is composed of three different surface

functionalities (Fig. 3). This process can be repeated many times to produce a surface with a highly diverse, spatially defined chemistry.

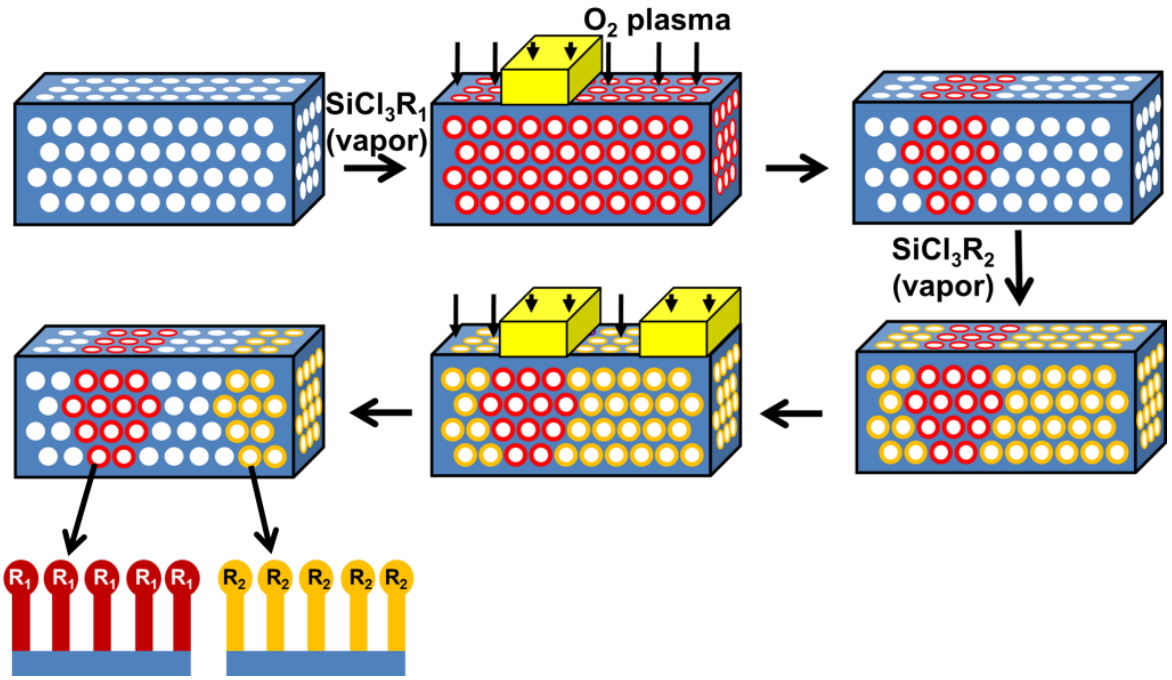

Figure 3. Schematic of the chemical encoding procedure. The inner surfaces of IOFs are functionalized by repeated iterations of exposing the entire film to alkylchlorosilane vapors, followed by selective exposure to oxygen plasma, masked through slabs of PDMS sealed on top of the film.

Although it has been previously shown that such masked plasma etching can be used to locally pattern self-assembled monolayers (SAMs) in 2D [61], the extension of this approach to 3D porous media is less intuitive, and has not been explored. To obtain a high resolution from this type of shadow-patterning process on a 3D porous surface, the modification process should be nearly isotropic to prevent shadowing effects from one pore to the next. In addition, the surface modification front must move sufficiently slowly that its penetration depth can be controlled. Under these conditions we can choose an exposure time that allows modification to occur throughout the depth of the structure, while not spreading too far underneath the mask. For our highly symmetric IOFs, which have a relatively small pore diameter (~300 nm) and inter-pore opening diameter (~80-

100 nm), we found that modification occurs on a timescale of several minutes and the width of the lateral interface is comparable to the film thickness, typically ~5-20 μm (see Appendix A for more details).

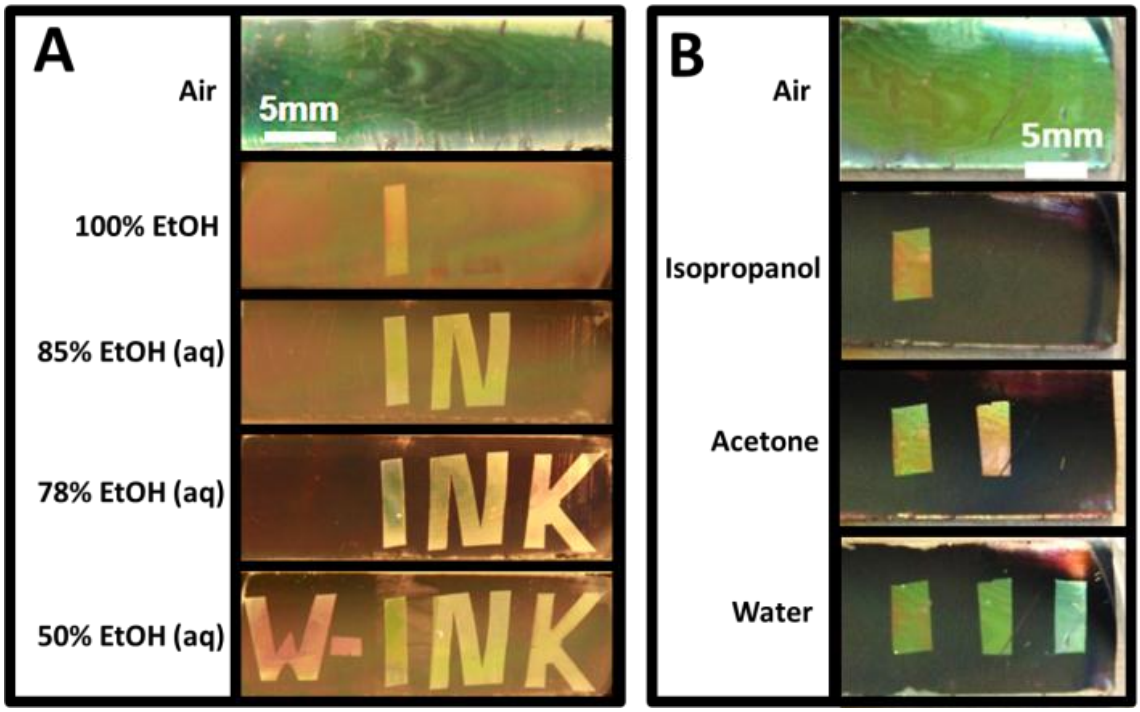

Figure 4. (A) Optical images of an IOF in which the word "W-INK" is encoded via the surface chemistry in an IOF: "W-" trimethylsilyl (TMS), "I" 1H,1H,2H,2H-tridecafluorooctyl (13FS), "N" *n*-decyl (DEC), "K" 3,3,3-trifluoropropyl (3FS), with a plasma-oxidized background (ROH). In different water-ethanol mixtures, different words appear. (B) Optical images of a film encoded with three bars (from left) 13FS, DEC, 3FS, displaying distinct optical patterns when immersed in the common solvents, water, acetone, and isopropanol.

Fig. 4A shows an example of an IOF, functionalized according to this procedure, with encoded messages containing five different local functionalities, the patterning appearing optically invisible when dry, but displaying four different messages when submerged in specific fluids. The word, "W-INK", is encoded in a SiO_2 inverse opal with combinations of the hydrophilic surface functionality left behind after O_2 plasma oxidation (referred to altogether as ROH hereafter for simplicity, see Ref. [61] for a detailed discussion of this type of surface chemistry) and four different surface groups with decreasing hydrophilicity: trimethylsilyl (TMS), 3,3,3-trifluoropropylsilyl (3FS), *n*-decylsilyl (DEC), and of (1H,1H,2H,2H-tridecafluorooctyl)silyl (13FS). While

displaying bright color and no pattern in air, the functionalized 3D photonic crystal reveals four different words when submerged in ethanol (EtOH), 85% (vol.) EtOH in water, 78% EtOH, and 50% EtOH, due to the area-specific wetting of the functionalized IOF by liquids with increasing surface tension and the resulting disappearance of the color in the infiltrated regions. In all cases, the message evaporates rapidly upon drying of the sample (several video examples of these encryption devices can be found on my YouTube channel: www.youtube.com/ibburges). The encoding via surface chemistry of many fluid-specific optical responses into a single material that appears homogeneous when dry is a type of multilevel encryption that could find many applications in security or authentication. This class of applications will be discussed further in Chapter 5.

However, a device that displays many fluid-specific optical responses could also be used as a colorimetric indicator that identifies liquids based on wettability. As an example of such an application, Fig. 4B shows a sample patterned with three stripes (13FS, DEC, 3FS) with an ROH background. Different color patterns are produced when the film is submerged in the three common cleanroom solvents, isopropanol, acetone and water.

While the general function of the IOF with regionally patterned surface chemistry is exactly as it was envisioned in Fig. 2C, a closer look at these proof-of-concept experimental results yields some striking and somewhat surprising results. Notably, (i) that the non-wetting state can be observed even for very low-surface-tension liquids (for example, 13FS-functionalized regions resist penetration of ethanol, γ_{EtOH} = 22.3mN/m, and even liquid precursors to PDMS, γ_{PDMS} ~ 20mN/m) and (ii) the high selectivity of wetting with respect to quite similar liquids or their mixtures (e.g. 78% vs. 85% ethanol (aq)). To explain these properties, Fig. 5A shows measured contact angles for different water-ethanol mixtures on flat silicon wafers (acid-piranha cleaned and O_2 plasma oxidized to ensure a native oxide layer) functionalized with 13FS, DEC, 3FS and TMS groups. These measurements are designed to estimate the intrinsic contact angle (sometimes also called the "equilibrium contact angle" in some sources [62]) corresponding to the onset of the infiltrated state. Notably, for the IOF shown in Fig. 4A, this boundary between the non-wetted and wetted states occurs in the contact angle range $\theta \sim 20^{\circ}$ in all cases.

Resistance to pore-infiltration down to such a low intrinsic contact angle implies that contact-line pinning and metastable states [62,63] must dominate the wetting dynamics of IOFs. This effect can be explained by the reentrant curvature (overhang) associated with the narrow openings between adjacent pores [63]. In an ideal IOF, all pores have the same diameter and spherical geometry and are connected to their nearest neighbors by inter-pore necks of identical radius. In such a symmetric system, the free-energy landscape associated with the propagation of the liquid front from one pore to the next is the same everywhere throughout the structure. Therefore, the global non-wetting state should occur when there is an energy barrier associated with propagation of the liquid front through a single unit cell. Figure 5B shows a schematic of a fluid front advancing through a single unit cell. The azimuthal angle subtended by an inter-pore neck in our IOFs typically fell in the range of φ_0 ~ 15-25º (see Chapter 2 for a detailed discussion of the neck-angle distribution typical of our IOFs). The total free-energy change associated with the liquid front having descended from the top of the pore down to an azimuthal angle, φ, is given by: $\Delta G = \gamma_{la}\pi R^2(sin^2\varphi - sin^2\varphi_0 - 2cos\theta_c(cos\varphi_0 - cos\varphi))$, where γ_{la} is the liquid-air surface tension, and θ_c is the intrinsic contact angle. Since the geometry at the top of the pore is reentrant with respect to the liquid front, there is a tradeoff between the energetically favorable liquid-solid interaction (when θ_c < 90º), and the energy cost of creating liquid-air interface. An energy barrier, and thus a metastable non-wetting state exists when $\frac{d\Delta G}{d\varphi}|_{\varphi=\varphi_0} > 0$. This occurs when $\theta_c > \varphi_0$. Therefore in our geometry, a transition from the non-wetting to the wetting state is expected to occur at $\theta_c = \varphi_0$ ~ 15-25º, well in the wetting range, and in agreement with what is observed in Fig 4A, 5A.

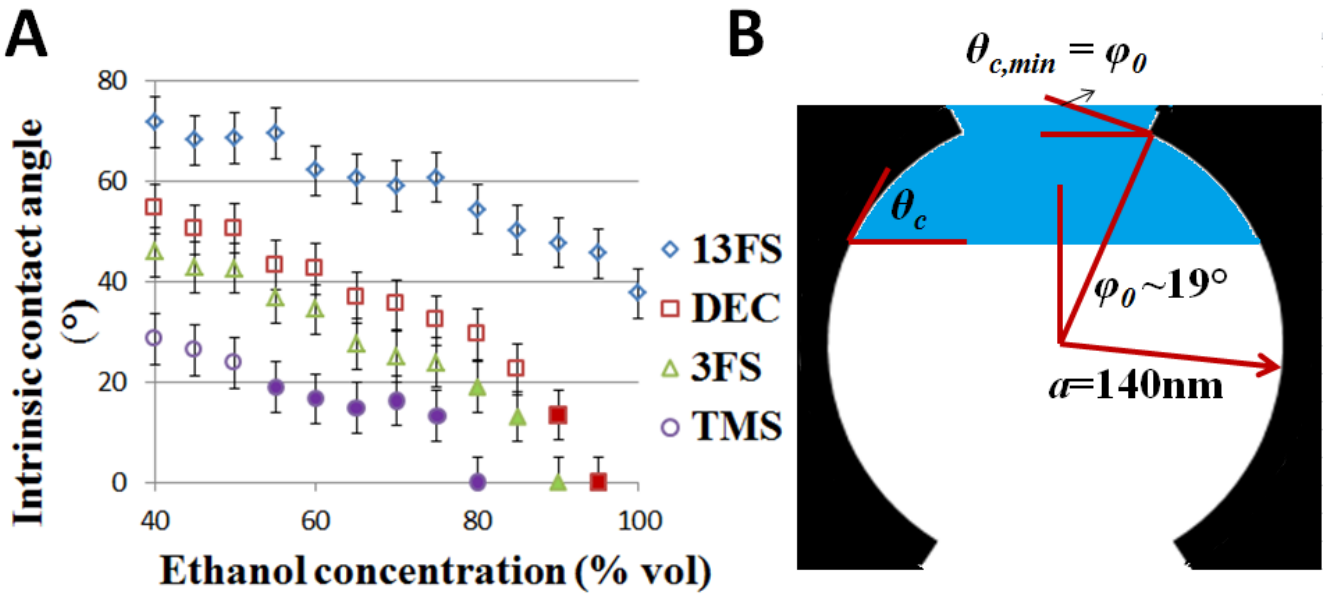

Figure 5. (A) Measured contact angles from different ethanol concentrations in water on flat silicon surfaces after exposure to 13FS, DEC, 3FS, TMS vapors. Filled markers indicate that regions of an IOF functionalized with the same groups are being infiltrated by the corresponding EtOH/water mixture. (B) Schematic of a liquid front propagating through a single unit cell of an inverse opal.

The remarkable selectivity of wetting observed here can be attributed to the highly regular geometry and defect- and crack-free nature of our IOFs [59]. Unlike typical porous materials, inverse-opal photonic crystals fabricated via co-assembly [59] have a particularly regular geometry, with uniform pore and pore-neck sizes, that leads to a high density of localized chemical information and thus sharply defined wetting thresholds for individual liquids. The absence of defects or cracks eliminates the irregular wicking artifacts and enables a high resolution of the wetting patterns.

At first glance, there are several unique properties of this material platform that lend it to many possible applications: (i) the high selectivity of infiltration, (ii) the range of fluid surface tensions across which this selectivity is observed, and (iii) its coupling to an easily detectable optical response. Beyond encryption, this system could find use as an optical litmus test that differentiates liquids based on wetting, as easy to use as pH paper is for detecting pH, but exploiting a property that exists for all liquids (surface tension) and thus could be

used to distinguish between similar liquids of any class (e.g. organic solvents, beverages, liquors, liquid fuels, etc.).

In Chapters 2, 3 and 4, I show how the W-Ink concept was developed for low-cost sensing into a scheme for colorimetry that we called a Wetting-In-Color-Kit (WICK). An effective sensor based on this concept must satisfy more performance requirements than a simple encryption device. In the design of our colorimetric indicator, we needed to consider sensitivity (how small a change in liquid composition can we detect?), the selectivity (how robust is a measurement against unknowns/contaminants?), and the adjustability (how can we tailor an indicator to fit a specific user need, e.g. to differentiate a specific user-defined set of liquids?).

In Chapter 2, we characterize the optofluidic properties of functionalized IOFs and use that characterization to estimate the maximum sensitivity of WICK. As the response is fundamentally sensitive to intrinsic contact angle, the sensitivity is estimated as the minimum difference in intrinsic contact angle that can be colorimetrically distinguished. Chapter 3 describes chemical functionalization techniques that were developed to tailor the response of a WICK to differentiate customer-defined liquids. In an encryption device, such as shown in Fig. 4A, the liquids (e.g. concentrations of water in ethanol) can be post-selected to match the desired patterns that are revealed. However in a useful indicator, this must be done the other way around.

In Chapter 4, the specificity of WICK is discussed. While sensitivity to such a generic property of liquids as wettability gives this type of indicator a potentially broad list of suitable applications (in principle, we could apply it to any low-cost sensing problem involving liquids), it also ensures that the sensor's response has fundamentally poor specificity. This tradeoff between generalizability and specificity is really not unique to WICK, but is ubiquitous to sensing problems in general. Two methods to enhance the specificity of WICK are described in Chapter 4. The first follows the well-studied approach of combinatorial sensing. Namely, an array of sensors, while each being independently weakly-specific, can produce combinations of responses that have much higher specificity [35,36,64,65]. This general approach, when combined with some of the techniques developed in Chapter 3, allowed us to produce WICK arrays that had much improved specificity. The second approach to specificity enhancement that was developed was to combine a wetting-based colorimetric measurement with an

equally simple measurement of a liquid's volatility, a different, but equally generic property of liquids, using a single WICK.

In Chapter 5, I will discuss some of the general pros and cons of the WICK platform applied to sensing, and also introduce some additional applications (not related to sensing) that the Wetting in Color technology may be well suited to. In addition to revisiting encryption, I will discuss some possible further applications of this approach in fluidics and nanofabrication. Finally, Appendix A provides detailed experimental procedures for all of the techniques described in this dissertation. It is my hope that a reader will be able to reproduce any of the experimental work presented here, based on the procedures given in this section. Appendix B gives a description of the theoretical methods used, and includes MATLAB code for the percolation simulation.

Chapter 2. Developing a Scheme for Colorimetry, Part 1: The Selectivity Limits

Structural color, derived from coherent scattering from wavelength-scale roughness or porosity, has received considerable interest in the development of new technologies, largely due to its broad capacity for tuning [17-57]. In particular, the prospect of easy-to-read, self-reporting sensors, which are based on structural color changes induced by specific chemical or physical properties of an unknown, has the promise to greatly expand the availability of portable and inexpensive diagnostics beyond those amenable to specific chemical processes or complex optical readouts [35-57]. Structural color is tied to a wide range of changes in the *physical* properties of a material forming the structure (*e.g*. the shape and density of a material) rather than a specific *chemical* state responsible for absorption in a characteristic wavelength region (*e.g*. a protonated or deprotonated molecule in pH indicators). This color, therefore, has no inherent specific chemical requirements (*e.g*. any material with periodic optical density displays iridescence as long as the periodicity is comparable to the wavelengths of visible light) [35-57]. This gives immense flexibility in the chemical properties of structural colorimetric sensors. Thus, tunable structural color carries the potential for broad applicability in colorimetric sensing. With chemistry as a versatile degree of freedom, structured materials have been engineered to change their shape, volume or density, and thus their color, in response to pH [38,41] magnetic fields [32], vapor adsorption [34,35,48,49,52], and mechanical strain [27,40,54] to name a few [20].

To design a sensitive, self-reporting colorimetric indicator that can be used over a broad class of materials, we must include the following properties in the design. (1) Our indicator should have the ability to elicit multiple responses to broad range of stimuli (e.g. different liquids). This requires the ability to encode complex chemical information into a single material platform [5,22,61,66-74]. (2) To make our indicator platform

applicable to a very broad range of sensing problems, we require high sensitivity to a general property defined for a wide class of materials (*i.e*. mass, density, surface tension, *etc*.) [75,76]. (3) A colorimetric indicator must be cost-effective and easy to use, therefore we require our colorimetric response to be as simple to read as possible.

In Chapter 1, it has been shown that defect-free silica inverse opal films (IOFs) [59] can be encoded to display distinct wetting patterns in different liquids by functionalizing them with a spatial pattern of organic surface groups. These patterns are clearly visible due to the large difference in refractive-index contrast between the wetted and non-wetted regions of the 3D photonic crystal. We used this concept to demonstrate a platform for multilevel encryption that we called W-Ink. The W-Ink encryption platform has the potential to satisfy all three of the above requirements for a colorimetric indicator for liquids. It allows for different liquids to produce distinct color patterns according to wettability, a universal property.

In this chapter, we will provide a thorough analysis of this highly selective wetting phenomenon observed in IOFs, and in Chapter 3, will demonstrate how it can be manipulated through simple and robust techniques to tune the surface chemistry to tailor the response to specific liquids. In Chapter 1, it was suggested that the remarkable selectivity of wetting observed in those preliminary experiments is caused by the unique, highly symmetric pore geometry of IOFs fabricated by colloidal co-assembly [59]. Here, we will use percolation modeling to identify the correlation between the selectivity and the uniformity of the sizes of the IOFs' inter-pore openings. Our model will be compared to wetting experiments and structural analysis of the IOFs. Using these results it is estimated that the colorimetric response is selective to differences in intrinsic contact angle ($\cos(\theta_c) = [\gamma_{sa} - \gamma_{sl}]/ \gamma_{la}$, where γ_{sa} is the solid-air surface tension, *etc*.) smaller than 5° when the surface chemistry is spatially uniform. In Chapter 3, it will be shown that this selectivity can be increased when the surface chemistry is graded vertically. Selectivity is ultimately limited by short-range disorder in the pore-geometry. Using these insights, the W-Ink concept can be expanded to develop a Wetting-in-Color-Kit (WICK) – an indicator that displays distinct colorimetric patterns in liquids in response to subtle differences in their wettability.

2.1. Structural disorder and selectivity

In this chapter, the selectivity limit of WICK is analyzed. Our IOFs each consist of a SiO_2 slab with a regular array of spherical air pores, arranged in a face-centered cubic (fcc) lattice [59]. Nearest neighbors are connected by small openings (necks). Scanning electron microscope (SEM) images of two IOFs are shown in Fig. 6A,B. When a porous material is immersed in liquid, spontaneous filling of the pores requires both an energetically favorable liquid-solid interaction (*i.e.* $\theta_c < 90°$) and the absence of an activation barrier (metastable state) associated with the propagation of the fluid front through the structure [63].

When a liquid front propagates through the narrow inter-pore necks, there is a free-energy tradeoff between the favorable wetting of the solid surface (assuming $\theta_c < 90°$) and the unfavorable creation of liquid-air interface [63]. An activation barrier associated with the propagation of the liquid front through the neck exists if θ_c is larger than the azimuthal angle subtended by the narrow neck in between the pores (shown schematically in Fig. 6C). For a given liquid and pore surface functionality, the corresponding θ_c defines a critical neck angle, smaller-than-which the liquid front will not be able to pass from one pore to the next. Therefore, the ability to precisely control the infiltration of liquids (and thus the colorimetric response to liquids) relies on our ability to control two parameters: i) the surface chemistry (which determines θ_c), and ii) the IOF's neck angles (which determine the critical θ_c for infiltration). Our strategy to maximizing selectivity while maintaining versatility of the indicator will be to exploit surface chemistry, which is treated as a tuning parameter, to illustrate highly liquid-selective control of wetting, while treating the IOF structure as a control parameter (to be kept as constant as possible). The selectivity, therefore, is ultimately limited by our ability to regulate the pore-structure.

In a perfectly symmetric IOF with exactly identical neck-widths throughout, the transition between an IOF that is completely impervious to liquid infiltration (displaying iridescent color) and one that is completely infiltrated (transparent, showing the color of the underlying substrate) at equilibrium would occur over an infinitesimally narrow range of liquid contact angles (θ_c). Given a technique to specify the surface chemistry of the pores with unlimited adjustability and precision, we could design a colorimetric indicator based on such a "perfect" structure that could detect arbitrarily small differences in wettability. An inherent advantage of using

IOFs fabricated by colloidal co-assembly for these studies is that they are characterized by an exceptionally regular structure [59]. However, they do display some degree of both short-range (< mm scale) and long-range (> mm scale) variations in the neck angles (φ_0). These variations must be considered to understand the wetting response, and controlled for as much as possible if we are to reproducibly study the effects of surface chemistry.

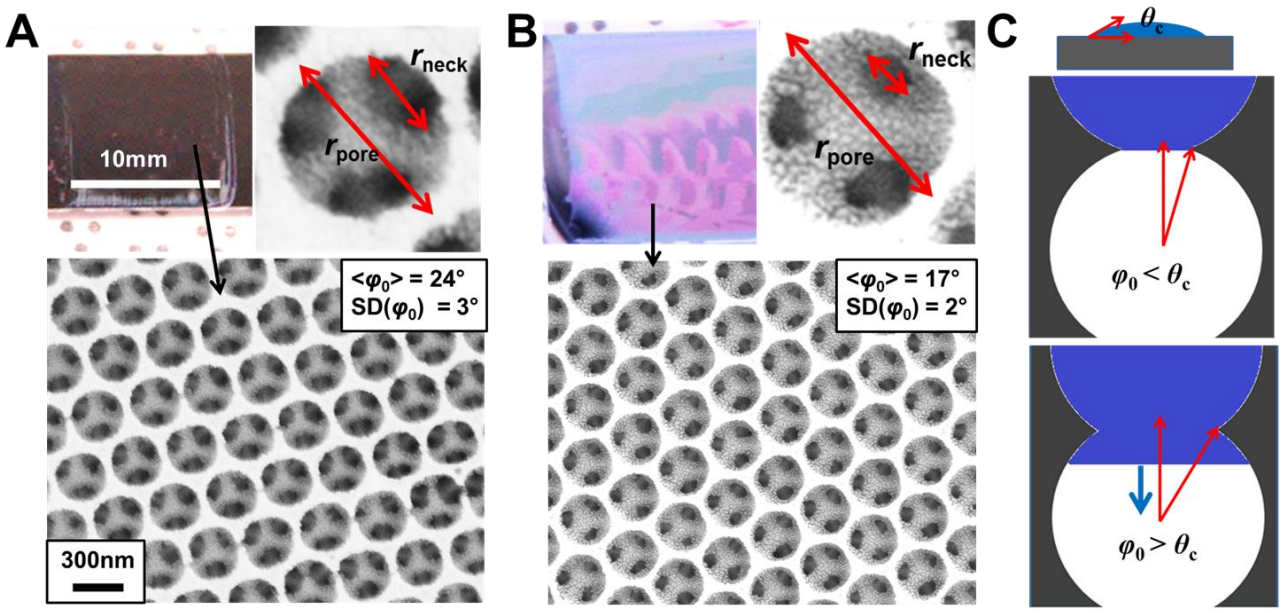

Figure 6. (A,B) Optical images of IOFs uniformly functionalized with DEC groups, submerged in 85% ethanol (aq) (top), and corresponding SEM images of the pore structure (bottom). (C) Schematic illustrating the relationship between the neck angle (φ_0, where $\sin(\varphi_0) = r_{neck}/r_{pore}$) and the wetting response. Infiltration of a pore occurs if the intrinsic contact angle (θ_c, where $\cos(\theta_c) = [\gamma_{sa} - \gamma_{sl}]/ \gamma_{la}$) is less than φ_0 (bottom schematic), while no infiltration occurs for smaller pores where $\theta_c > \varphi_0$ (top schematic).

Fig. 6A,B illustrates the effects of sample-to-sample variability in φ_0 on the wetting outcomes when the surface chemistry is fixed. The samples are functionalized with n-decylsilyl (DEC) groups (from exposure to vapors of the corresponding alkylchlorosilane). Photographs of both (top) show the two IOFs immersed in 85% (vol.) ethanol (EtOH) in water. The film in Fig. 6A is infiltrated by the liquid (discernible from the color), while the film in Fig. 6B is not infiltrated. As shown in the SEM images (bottom), the more easily-infiltrated IOF is

characterized by larger φ_0. We estimated the neck angles by measuring the ratio of the pore and neck widths (measured in the tangential direction), using $\sin(\varphi_0) = r_{neck}/r_{pore}$. This estimation relies on the assumptions that our pores are near-spherical and that the top layer (where the neck-widths can be easily measured) well-represents the structure throughout. As φ_0 is derived from a ratio of lengths, scaling errors (*e.g.* calibration) in our SEM imaging do not affect our estimation. The mean and standard deviation in neck angles measured from the images shown in Fig. 6A,B are indicated on the images. The maximum standard deviation in the neck angles, estimated from the largest value for short-range variability measured from a single SEM image, was 3.2°. This value was further used in theoretical study of the sensitivity limits described below.

2.2. Modeling the optical response to partial filling

Short-range variability in the neck angles is what ultimately limits the selectivity of an IOF's colorimetric response to liquids. Infiltration of a liquid through an IOF with uniform surface chemistry and a random distribution of neck-angles will proceed as percolation through a regular fcc lattice [77] with a bond connectivity determined by θ_c. The final equilibrated infiltration state will be a statistical distribution of filled and empty pores over a range of θ_c determined by the local variance of φ_0. We used a numerical percolation model to derive the expected equilibrium filling states from bond connectivities (see Appendix B). The input parameters that are used to determine the bond connectivity are the intrinsic contact angle and the distribution of neck angles. The model considered an fcc lattice of pores with a uniform thickness (given as the number of close-packed layers) and a large lateral area (10^4 unit cells). Neck-angles were randomly assigned to each nearest-neighbor connection according to a normal (Gaussian) distribution. For the results shown in Fig. 7, we used a neck-angle distribution with $<\varphi_0>=19.6°$, $SD(\varphi_0)=3.2°$, a typical mean neck angle observed in our IOFs and the maximum standard deviation measured from a single SEM image (see section 2.1). We chose the maximum variability in order to get a conservative estimate of the selectivity. Inputting θ_c and starting with a completely filled top layer (as these are half-spheres in our IOFs and have no re-entrant curvature [59], see SEMs and schematics in Figs. 1,6), the simulation filled all pores with paths of inter-pore fluid-connectivity (*i.e.* where $\varphi_0 > \theta_c$) connecting them to the top filled layer.

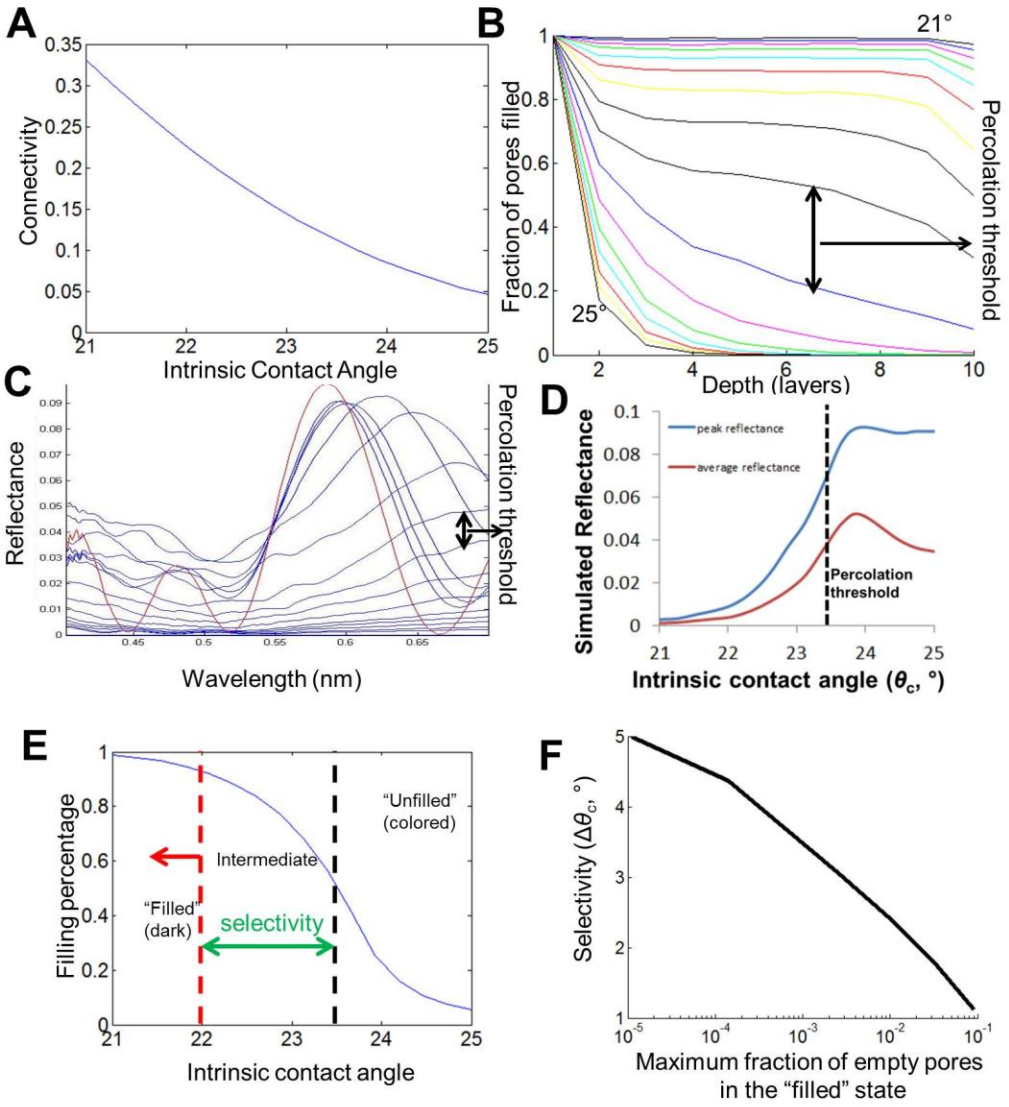

Figure 7. (A) Connectivity as a function of intrinsic contact angle and (B) pore filling profile as a function of depth for different intrinsic contact angles. 2D FDTD optical simulations showing the normal incidence reflection spectra (C) and the total reflectance (D) of an IOF as a function of intrinsic contact angle. The statistical filling profiles (as a function of depth) are taken from the percolation simulation (A,B). (E) Total filling percentage (all layers) plotted as a function of intrinsic contact angle from the percolation simulation. (F) Predicted selectivity limits (expressed in terms of θ_c) as a function of maximum tolerated fraction of unfilled pores defined as the "filled" state. The colorimetric "unfilled" state is defined as having bond connectivities below the percolation threshold (12%). ($<\varphi_0>$=19.6°, SD(φ_0)=3.2° in all simulations)

Fig. 7A shows the pore-to-pore connectivity as a function of the intrinsic contact angle. Connectivity is obtained simply by integrating the φ_0 distribution from $\theta_c \rightarrow \infty$ (for an infinite lattice), and thus was computed analytically. Since the filling of IOFs by fluid using this model is a bond-percolation problem with an ideal standard geometry of possible connectivity (fcc lattice), the percolation threshold for this problem has been previously computed numerically, occurring at 12% connectivity [77]. For an infinite lattice, the percolation threshold connectivity (or the fraction of pores where $\varphi_0 > \theta_c$) defines the value above-which infinite paths of connectivity will exist in the lattice [77].

Fig. 7B shows filling profiles (filling fraction at equilibrium vs. depth in the structure) for θ_c in the range, 21°-25°, where the majority of the range of partial filling can be observed (the thickness is 10 close-packed layers. Interestingly, the form of the filling only follows one of two general qualitative patterns. For connectivity above the percolation threshold (smaller θ_c values), the filling fraction is approximately constant throughout the structure (with the exception of a decrease at the very bottom layer, as a result of lattice sites having fewer nearest neighbors in this layer). This trend holds for any input thickness in the simulation. This reflects the long paths of connectivity typical of this regime, which allows diffusion throughout the structure without a strong effect of proximity to the boundary. For connectivity below the percolation threshold, on the other hand, the filling profile takes on the form of an exponential decay with distance from the top layer (the source of liquid), with the rate of decay increasing with decreasing connectivity. This is reflective of the fact that the average path-length of connectivity should be short in this regime (on the order of the constant of exponential decay).

We used Finite-Difference-Time-Domain (FDTD) optical simulations to qualitatively estimate the correlation between the fluid-filling states shown in Fig, 7B and the observed reflected color. To reduce the computational load, we ran simulations in two dimensions. We collapsed each layer into a one-dimensional row of pores (100 unit-cells long) while maintaining the correct filling fraction for each layer determined by the full 3D percolation simulation. In these simulations, the IOF is considered to be fully immersed in the fluid and the refractive-index matching between the fluid and the IOF was considered perfect (both were given $n = 1.4$). The structure was excited by a plane-wave, propagating at normal incidence and the reflectance was monitored by

transformation to the far-field. Fig. 7C shows the computed reflectance spectrum for each value of θ_c shown in Fig. 7B (the total thickness is 5 close-packed layers in this simulation). In red, the computed spectrum of the IOF in air is shown for comparison.

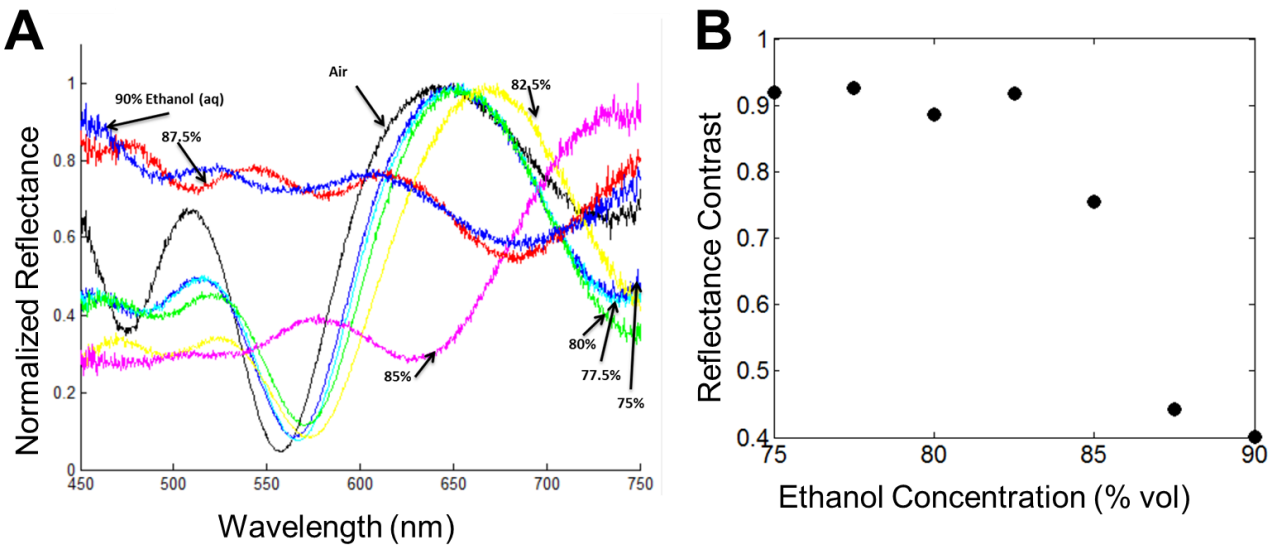

Figure 8. (A) Experimental evolution of partial filling. Normal incidence reflection spectra from a region of an IOF functionalized with DEC groups having a thickness of 5 close-packed layers, taken dry (in air) and submerged in ethanol-water mixtures with concentration of ethanol varying from 75%-90% (vol). (B) Reflectance contrast of the central peak (defined as $[R_{max}-R_{min}]/R_{max}$) as a function of ethanol concentration.

Fig. 7D shows the peak reflectance and the average reflectance as a function of the θ_c determined by these simulations. The saturation of the reflectance occurs near the percolation threshold. This makes sense if we consider that below the percolation threshold, sufficiently thick IOFs must possess completely empty layers at a certain depth (this follows directly from the result that infinite paths of connectivity cannot exist in this regime). Fig. 8A shows measured optical spectra of an IOF (DEC-functionalized) when immersed in different water dilutions of ethanol, in increments of 2.5%. Qualitatively, these spectra resemble the results of the simulations. However, there is not perfect refractive-index matching in the filled state, as evidenced by the small oscillations in the filled state spectrum (90% ethanol). It is also worth noting that only a 2.5% increase in ethanol concentration takes the spectrum from a point likely below the percolation threshold (85%), where a photonic

crystal peak is clearly visible, to a much flatter spectrum (87.5%) more indicative of near total filling. Shown in Fig. 8B, the reflectance contrast of the central peak depletes over an ethanol-concentration range of 5% (corresponding to $\Delta\theta_c \sim 9°$). However, a substantial drop in contrast and a large qualitative change in the spectrum are observable over a half of that range (85% → 87.5%).

To extract a colorimetric selectivity from this continuous distribution of partial filling states we must determine what constitutes "easily visually distinct" color patterns, which is inherently subjective. One way to define what constitutes two visually distinct color patterns in a way that ensures user-friendliness is to specify that they must have countable differences (*e.g.* each region can only be assigned two possible states). We assign this binary scale to the color response of IOFs by allowing a user to only be able to designate a region with uniform surface chemistry as being "unfilled" (bright color) and "filled" (transparent, negligible contrast with the underlying substrate).

To implement this binary evaluation system, we must choose a maximum fraction of filled pores that defines the colorimetric "unfilled" state and a maximum fraction of unfilled pores that defines the "filled" state. In this definition, the colorimetric selectivity (minimum resolvable difference in θ_c) is defined by the range of θ_c over-which the filling fraction does not fit into either of these definitions. To extract this range, we choose lower and upper bounds of connectivity to define the selectivity limit of WICK. The bond percolation threshold (12% connectivity) is a logical upper-bound connectivity to define as the "unfilled" state. For connectivity below the bond percolation threshold all paths of fluid flow have finite length [77]. This means a sufficiently thick IOF will have completely empty layers at equilibrium, thereby producing color that can be easily distinguished from the filled state. This general notion that connectivity below the percolation threshold will produce bright color is also qualitatively supported by our FDTD simulations.

We define the onset of the "filled" state by a maximum tolerance of empty pores. Fig. 7F plots the selectivity (expressed in terms of θ_c) as a function of this tolerance. The smallest tolerance shown in Fig. 7F (10^5 unit cells per unfilled pore) should be a very conservative estimate of this limit. 10^5 unit cells per unfilled pore corresponds to an average distance of >30μm (100 unit cells) between scattering centers and a fractional

scattering cross-sectional area of $<10^{-4}$ for a film of typical thickness of 5 layers illuminated from above. Thus the scattered intensity from empty pores will be very low in this limit (the film appears transparent). Therefore an IOF with uniform surface chemistry has the capacity to colorimetrically differentiate liquids based on differences in θ_c of less than 5°.This corresponds to concentration selectivity of at least 5% in water-ethanol mixtures, in agreement with our experimental observations. Using the leveling of the reflectance at the upper and lower values in Fig. 7D as a less conservative definition of the "filled" state, we get that differences in θ_c of ~3° should be colorimetrically resolvable in an IOF with our simulated distribution ($<\varphi_0>$=19.6°, SD(φ_0)=3.2°). Fig. 9A shows how the selectivity correlates to the short-range variability (SD(φ_0)) for an IOF with $<\varphi_0>$=19.6° (here the "filled" state is defined by an empty-pore tolerance of 1:1000), and gives an estimate of how sensitive the selectivity is to the uniformity of the structure.

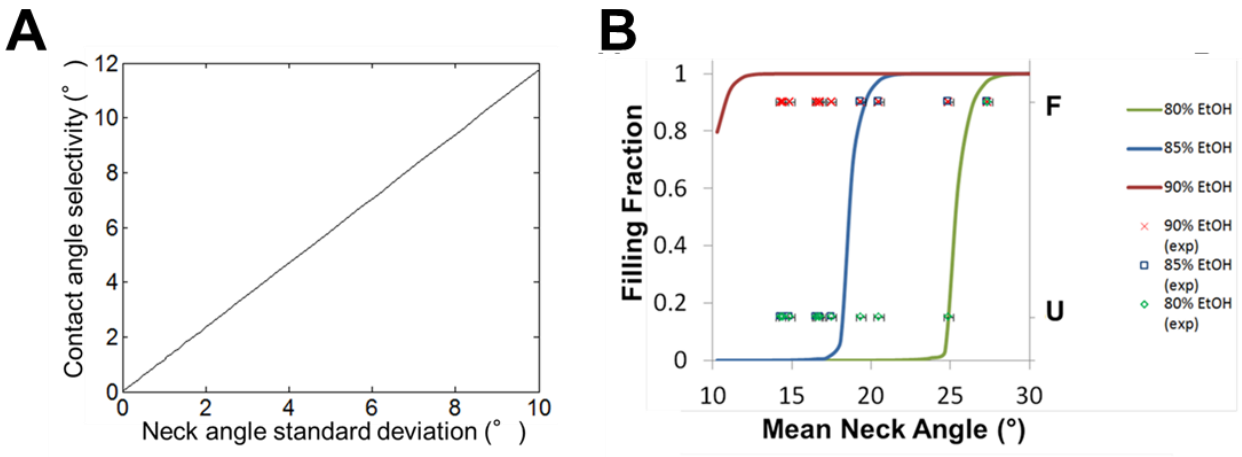

Figure 9. (A) Predicted selectivity limits (expressed in terms of intrinsic contact-angle) as a function of the neck-angle standard deviation (Mean = 19.6°). While we define the colorimetric "unfilled" state as having bond connectivity below the percolation threshold (12% for fcc lattice). In this curve, the colorimetric "filled" state is defined by a maximum tolerance of 1 empty pore per 1000 pores. (B) Simulated equilibrium filling percentages calculated from the neck angle distribution using percolation modeling of IOFs functionalized uniformly with DEC groups immersed in 80%, 85%, and 90% ethanol (aq). Isolated points overlaid correspond to mean neck angles measured from SEM images. The *y*-axis values (right axis) depict the colorimetric state observed (F = filled, U = unfilled) in 80% EtOH (green diamonds), 85% EtOH (blue squares), 90% EtOH (red X's).

2.3. Selectivity and long-range variability

The modeling in the previous section shows the limits on selectivity imposed by short-range variability in φ_0. However, variability can be much larger at larger scales within a sample (e.g. mm-scales) or from one sample to the next (see Fig, 9B). On the other hand, this type of variability may be controllable, either by post-selection of samples/regions or by finer control of the IOF fabrication parameters. Using intrinsic contact angles measured from DEC-functionalized flat surfaces (see Chapter 1, Fig. 5), we used our percolation model to try to correlate variability in filling in IOFs with the same surface chemistry (see Fig. 6) to long-range variability of the structure. For these simulations, a sample 30 close-packed layers thick with a large lateral area (10^4 unit cells) was used. The solid curves in Fig. 9B show the simulated overall filling fraction for 90% ($\theta_c = 13° \pm 5°$), 85% ($\theta_c = 22° \pm 5°$), and 80% ($\theta_c = 29° \pm 5°$) EtOH for DEC-functionalized IOFs as a function of mean neck angle. A standard deviation of 3.2° was used in the simulations.

To verify the correlation between the neck angle and the wetting behavior, we characterized the neck angle distribution (from SEM images sampled randomly across each film) and the infiltration state (from the presence or absence of iridescent color) in 80%, 85% and 90% EtOH of 12 IOFs uniformly functionalized with DEC groups. These measurements are represented by the isolated points in Fig. 9B. Fig. 9B shows good agreement between our theoretical predictions and experimental results, and that the long-range variation in the response of a DEC-functionalized IOF to these liquids correlates to the long-range variation in the neck angles. As will be described in Chapter 3, we can exploit this to develop a non-destructive quality control procedure to limit the effect of long-range variability in the neck-angles.

Chapter 3. Developing a Scheme for Colorimetry, Part 2: Optimization and Tuning

As the colorimetric selectivity only exists at a specific wettability threshold (intrinsic contact angle, $\theta_c \sim 20°$, see Chapter 1), a WICK displaying mutually distinct colorimetric responses in *n* different liquids requires spatial regions containing at least (*n*-1) different surface functionalities. Furthermore, the ability to practically exploit WICK for liquid *identification* requires that IOFs have access to a continuously adjustable range of surface functionalities. This allows for specific colorimetric responses to be designed to distinguish specific liquids that are designated *a priori*. To address these challenges, we describe two protocols in this chapter based on chlorosilane chemistry and plasma-oxidation, which give us the power to generate continuously adjustable surface chemistry within the pores. We also implement a non-destructive quality control procedure to regulate the long-range variability in the pore geometry. These protocols allow us to both maximize the selectivity of the indicator and give us the capability to design a WICK that mutually colorimetrically differentiates arbitrary sets of liquids. We present several examples to illustrate this point: differentiating between water dilutions of ethanol with selectivity down to 2.5% differences in concentration; distinguishing different pure alcohols (methanol, ethanol, isopropanol), and alkanes (hexane, heptane, octane, nonane, decane); and differentiating between grades of automotive fuel (gasoline and diesel).

3.1. Non-destructive quality control

Fig. 9B shows that the variability in the surface chemistry (at least for DEC functionality) is generally below that of the neck angles. However it also illustrates, that while the short-range variability of the IOF neck angles is generally small (SD ≤ ~3°) the variability from one sample to the next can be sufficiently large to skew the effects of surface chemistry. To limit this effect, we introduced a quality control step in the studies described

below: All samples described hereafter in this chapter were first uniformly functionalized with DEC groups and characterized optically in 85% and 90% EtOH. In order to be considered for further use, the IOF must display an unfilled state (no loss of iridescent color) in 85% EtOH and a filled state (no contrast with the blank substrate) in 90% EtOH (see bottom row of Fig. 10B for example). After a sample passes this test, the DEC functionality is removed by oxygen plasma and subsequent acid piranha cleaning, and the samples are re-functionalized in one of the manners described below. This limits the mean neck angles to approximately the range of 14°-18° (see Fig. 9B). Consistent with the statistics displayed in Fig. 9B, roughly one third of our samples showed out-of-range neck angles and were discarded as a result of this quality control process.

3.2. Continuous tuning of the response

To use WICK to differentiate any two liquids, it is essential to be able to encode a continuous range of wettability in the IOFs. In contrast to the encryption-type application of the W-Ink platform described previously (Chapter 1, where the decoding solvents can be determined *a posteriori* based on the availability of specific alkylchlorosilanes), effective design of a solvent *indicator* requires that one can choose two liquids for differentiation *a priori* and then be able to tune the surface chemistry such that the IOF displays different filling states in each liquid. We have developed two different techniques for tailoring surface functionality continuously. In both approaches, one requires only two alkylchlorosilanes, $SiCl_3R_1$ and $SiCl_3R_2$, where the IOF functionalized with only the R_1 groups displays the unfilled state and the IOF functionalized with the R_2 groups displays the filled state in both liquids. To illustrate these techniques, we used 13FS and DEC groups as R_1 and R_2 and ethanol-water mixtures of varying concentration to produce a continuum of surface tensions (and values of θ_c). 13FS-functionalized IOFs display an unfilled state in all water-ethanol mixtures (including 100% EtOH) and DEC-functionalized IOFs display a filled state in EtOH concentrations larger than 85% (as enforced by quality control). In section 3.4 we illustrate the general applicability of these techniques, performing analogous optimizations, but replacing water-ethanol mixtures with several other classes of liquids (pure alcohols, pure alkanes, auto-fuels).

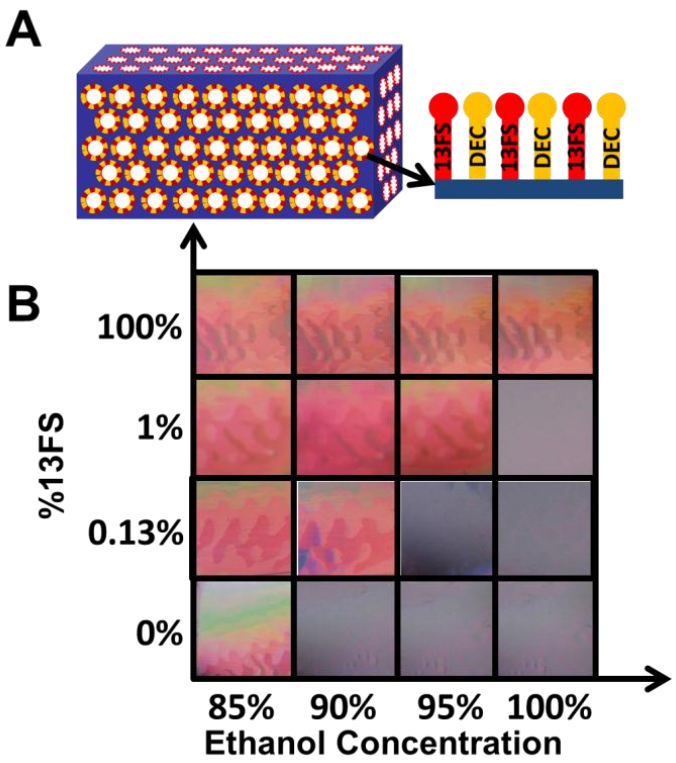

Figure 10. (A) Schematic depicting the formation of mixed functionalities by evaporating mixtures of two alkylchlorosilanes (13FS in red and DEC in yellow) to produce wetting responses that span the range in between that of a homogenous monolayer of each. (B) Color-map illustrating an array of IOFs (each square is 1cm x 1cm), functionalized with various mixed monolayers of 13FS and DEC, that allow mutual colorimetric distinction of 85%, 90%, 95% and 100% ethanol (aq). All photographs in a single row are of the same IOF. The y-axis denotes the vol. fraction of 13FS-trichlorosilane used in the liquid-liquid mixture that evaporated onto the IOF.

Perhaps the most intuitive method to functionalize an IOF such that the wettability displayed lies between that from homogeneous coatings of 13FS and DEC is to deposit a heterogeneous mixture of 13FS and DEC groups on the surface (illustrated in Fig. 10A). We generated mixed 13FS:DEC monolayers by exposing IOFs to vapors from a liquid-liquid mixture of 13FS- and DEC-trichlorosilanes. Adjusting the relative concentration of 13FS- and DEC-trichlorosilanes in the liquid-liquid mixture should alter the relative density of groups on the surface and was used to tune the infiltration threshold to occur at any ethanol concentration between 85% and 100%. Fig. 10 shows a response color-map showing four samples (each row is one IOF) functionalized with

13FS, DEC and different mixtures of the two. Using mixtures of 13FS and DEC groups, we were able to create IOFs whose wetting threshold occurs at 90% and 95% EtOH. By comparing the columns of the color-map, we see that samples with these four functionalities produce an array that colorimetrically identifies the relative concentration of a water-ethanol mixture to a precision of 5% across the full range selectivity offered by DEC and 13FS functionalities (85%-100% EtOH).

3.3. Vertical gradients of wettability

Generating continuous gradients of wettability in an IOF is a second method that can be used to produce distinct colorimetric responses across a continuous range of surface tensions. We generated vertical gradients of wettability using *short* plasma-exposure times (insufficient to completely remove the existing groups throughout the depth of the structure) between successive silane depositions. Lin et al [61] showed surface modification by oxygen plasma that propagates through tightly confined channels and proceeds as a front with a graded boundary through the porous network slowly (several minutes for 20μm-wide channels). Depicted in Fig. 11A, we first functionalized an IOF with the more lyophobic group (R_1, 13FS). Following a short (< 2min) exposure of the structure to oxygen plasma, we expect incomplete removal of the R_1 groups, with the efficiency of removal decreasing with increasing depth. Subsequent addition of less lyophobic groups (R_2, DEC) via exposure to $SiCl_3R_2$ vapors generates a mixed, graded surface chemistry with an increasing ratio of R_2/R_1 from the bottom to the top of the IOF.

We expect IOFs with vertical gradients of chemistry (in which the wettability decreases with depth) display distinct partial infiltration patterns in incrementally different liquids, each penetrating a fixed depth (Fig. 11B). As the total thickness of our IOFs can be made to vary across the sample (naturally occurring in vertical evaporative depositions [59]), distinct depths of penetration are viewed as distinct rainbow patterns whose size and location in the chip is unique to the depth filled. The schematic in Fig. 11C illustrates this principle. The top photo in Fig. 11C shows a film that has been functionalized uniformly with 13FS groups, exposed to oxygen plasma for 45s and then functionalized with DEC groups.

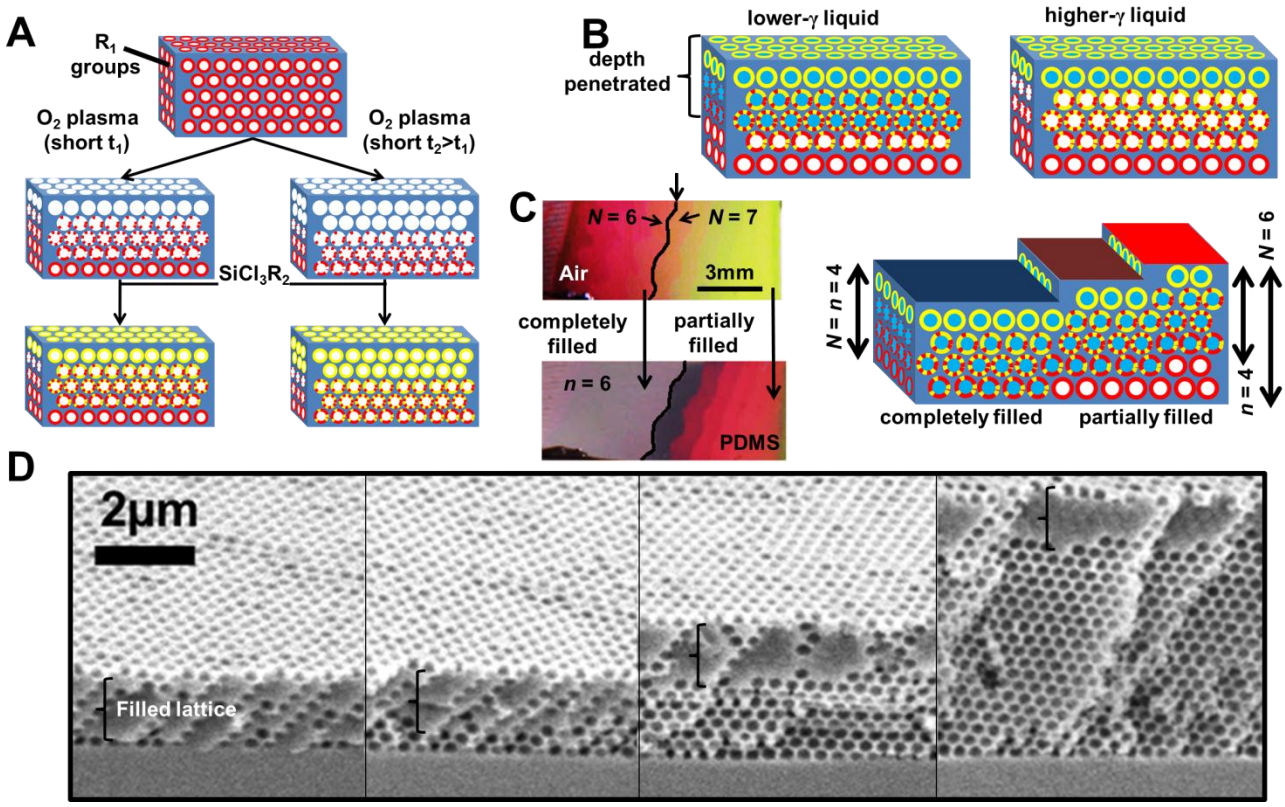

Figure 11. (A) Schematic depicting the use of short O_2 plasma exposure between successive silanizations to generate a vertical gradient of wettability. (B) Using vertical gradients where wettability decreases toward the bottom of the sample, liquids penetrate up to a fixed depth that increases with decreasing surface tension (decreasing θ_c). (C) This depth translates into a distinct color pattern in IOFs having a naturally varying total number of layers (shown in schematic). Photographs show an IOF functionalized DEC→13FS (45s plasma exposure) in air (top) and after soaking in PDMS precursors (cured before imaging). The total thickness of this IOF is increasing from the left to the right of the image. The color completely disappears in the regions where the total thickness is less than the penetration depth (n = 6). The black line on the images indicates the boundary between regions with 6 and 7 total layers (N). (D) Scanning electron micrograph cross-sections illustrating the fixed degree of layer penetration of the PDMS precursors (subsequently cured) over a wide range of film thicknesses.

The total thickness of the film varies from only two close-packed layers on the far left to a large number (>20 layers) on the far right, each visible "stripe" representing a region of fixed thickness, having one more layer than the stripe to the left of it. In thinner regions (N < ~10) these stripes are wide enough to be visible by eye

(~0.5-1mm wide). In the thickest regions very close to the edges, the thickness increases on shorter length-scales and the stripes become harder to resolve. When this sample is immersed in liquid precursors to polydimethylsiloxane (PDMS, Sylgard 184, subsequently cured to allow visualization by SEM), the liquid completely penetrates the first 6 layers ($n = 6$) and the IOF becomes transparent (displaying the grey of the silicon substrate) in regions where $N \leq 6$. The SEM cross-sections in Fig. 11D show the consistent penetration depth from the top of the IOF that is independent of the total thickness.

The color displayed by an IOF having N layers, the top n of which are filled ($n < N$), should match the color produced by an empty ($N - n$)-layer IOF, since the filled regions become transparent, provided there is sufficient index-matching between the fluid and the silica. Fig. 12A shows four segments of an IOF, which are all functionalized with a DEC→13FS vertical gradient using different plasma-exposure-times, immersed in PDMS precursors (subsequently cured). Owing to the varied oxygen plasma exposure time, the PDMS completely filled the lattice up to a different depth in each sample. However, as illustrated by the normalized reflectance spectra in Fig. 12B-D, the apparent color in a given region depends only on the number of unfilled layers (N-n) and is relatively insensitive to the total thickness (N).

While at face value, this technique is far less simple and straightforward than the uniformly mixed functionalities described in section 3.1, it possesses two important advantages with respect to the colorimetric differentiation of liquids: i) the minimum colorimetrically discernible difference in wettability can be smaller for vertical gradients than for uniformly functionalized IOFs (for the same short-range variability in the neck-angle, φ_0); and ii) a single vertical gradient produces many distinct patterns in many different liquids. Vertical gradients allow enhancement of the colorimetric selectivity, not by decreasing the range of θ_c over which partial infiltration patterns are observed, but by transforming partial infiltration patterns to a form that becomes easy to mutually distinguish visibly (*i.e.* have countable differences).

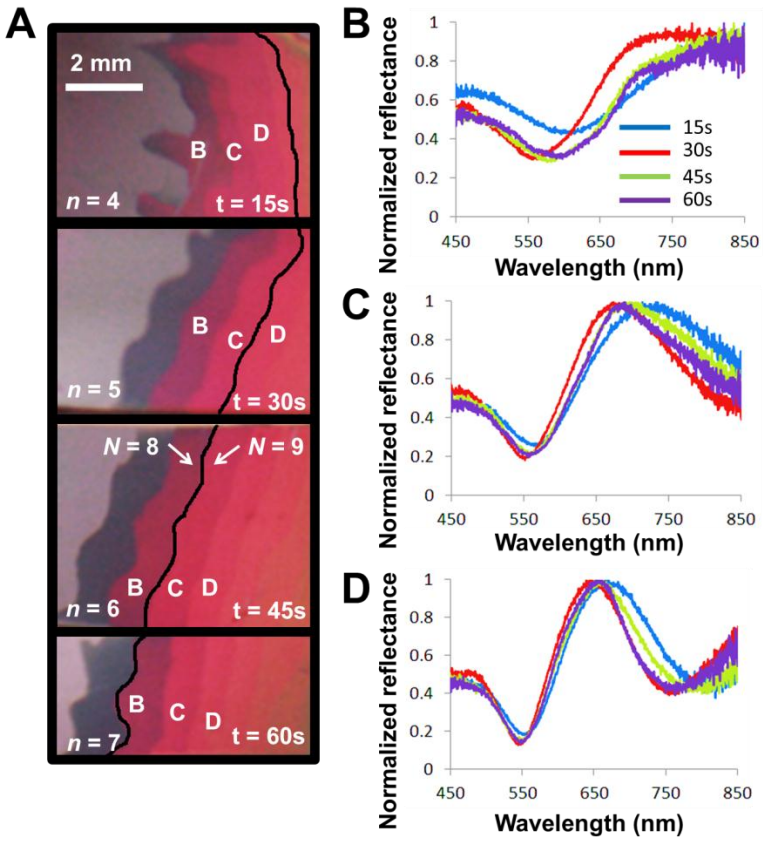

Figure 12. (A) Photographs of four segments of an IOF functionalized with a DEC→13FS vertical gradient using different plasma-exposure times, from top: 15s, 30s, 45s, 60s, submerged in PDMS precursors. The number of completely filled layers (*n*) is listed on each image. The black line drawn on the images indicates the boundary between regions with 8 and 9 total layers (*N*). (B-D) Normalized reflectance spectra for the three colored stripes indicated in (A) showing that the color is sensitive to neither *N* nor the *n* independently, but depends only on (*N* - *n*).

Fig.13B shows two percolation simulations (using the model described in section 1 with 15-layer IOFs) comparing IOFs with uniform and graded surface chemistry that illustrate this effect. Fig. 13A shows the filling fraction as a function of the depth in an IOF ($<\varphi_0>$ = 19.6°, SD(φ_0) = 3°) with spatially homogeneous surface chemistry for liquids with all integer θ_c values over the range of [12°-27°]. Fig. 13B shows simulated infiltration profiles for the same IOF structure with θ_c increasing with depth. To approximate the type of gradation that might be produced by short oxygen plasma exposure, we let θ_c obey a cumulative normal distribution (mean = 7 layers, SD = 3 layers) as a function of depth, having the same values as Fig. 6A (shown for each curve in Fig. 13B) at the

top layer, but increasing with depth by a total magnitude of 10° over 15 layers (12°-27° at layer 1, 22°-37° at layer 15). As shown in Fig. 13A, partial wetting in uniformly-functionalized IOFs takes on two qualitative forms. For θ_c higher than the percolation threshold ($\theta_c > 23°$ for this IOF), the filling fraction decays exponentially with depth. These filling profiles can be colorimetrically identified as "unfilled" because regions of sufficiently large total thickness will contain completely unfilled layers. For θ_c lower than the percolation threshold ($\theta_c \leq 23°$ in Fig. 13A), the filling fraction is roughly homogeneous throughout the structure.

Since the iridescent color of IOFs, like most structurally colored materials, depends on the viewing angle, the comparison of colors in a non-binary fashion (*e.g.* using a color guide) could prove difficult. In contrast to uniformly functionalized IOFs, partial filling patterns produced by vertical chemical gradients are easy to distinguish by eye in our IOFs, because they contain natural variations in total film thickness. What is notable about the curves in Fig. 13B is that most (*e.g.* θ_c = 13°-21°) display the same filling profile, but successive curves are shifted by one or more layers. Recalling that, as shown in Figs. 11 and 12, completely filled layers do not contribute to the color of an IOF, adjacent curves in Fig. 13B would appear as identical "rainbow" patterns that are shifted in space by one layer-step in an IOF having a varying total-thickness such as in Fig. 12A. These patterns could be easily visually differentiable at any angle because instead of comparing colors (each of which are viewing-angle dependent), the problem has been reduced to that of measuring the distance (or counting the number of layer steps) to the start of the "rainbow" pattern.

Fig. 13C shows a DEC→13FS (45s etch time) vertical gradient in which 92.5% EtOH, 95% EtOH, 97.5% EtOH and 100% EtOH are distinguished colorimetrically. In this sample, a 2.5% increase in ethanol concentration is sufficient to increase the final filling depth by enough to produce a clearly different visual pattern. An array of hydrophilic "teeth" have been defined via selective oxidation to aid in the visualization (*i.e.* increase the countability).

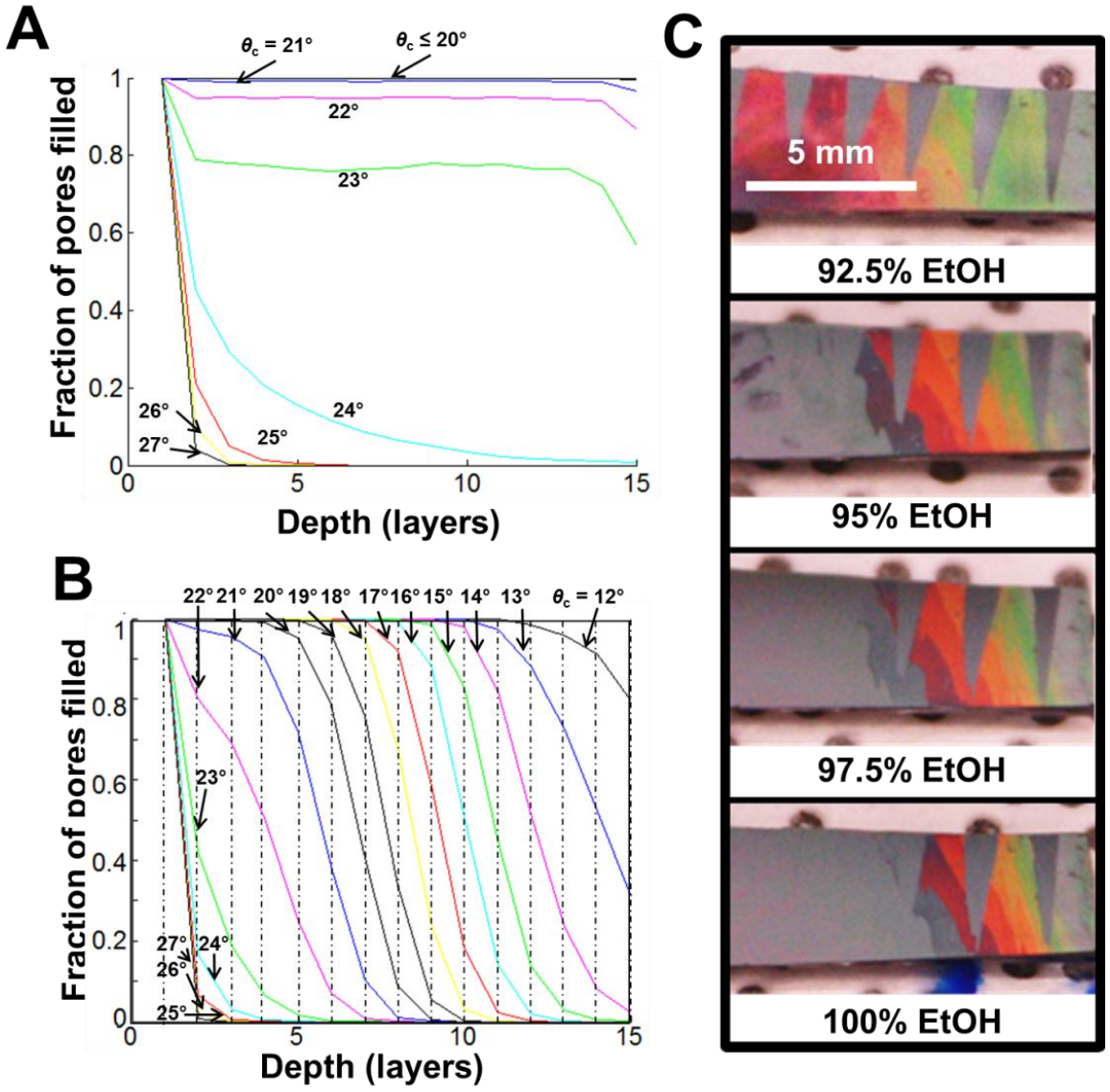

Figure 13. (A,B) Simulated layer-by-layer wetting profiles for liquids differentiated by one degree of intrinsic contact angle (12°-27°), in an IOF (<φ_0>=19.6°, SD(φ_0)=3°) with spatially uniform wettability (A), and a graded wettability (B), where the intrinsic contact angle increases with depth by 10° (12°-27° at layer 1, 22°-37° at layer 15) according to a cumulative normal distribution (mean = 7 layers, SD = 3 layers). The boundary condition of a completely-filled top layer (half-spheres) is assumed in all simulations. (C) Photographs illustrating the colorimetric distinction of different ethanol-water mixtures using an IOF functionalized with a vertical gradient DEC→13FS (45s plasma exposure).

3.4. Selective deconstruction to guide the eye

An important ingredient in the design of any colorimetric indicator is that it is as easy to read as possible. We can enhance the visual perceptibility of WICK readings by selectively oxidizing (to make lyophilic) certain regions of the IOFs as a last step to control the patterns that appear in the different test liquids. Fig. 14 shows four examples of indicator strips using both homogeneously mixed monolayers (Fig. 14A) and vertical gradients of wettability (Fig. 14B-D), where this extra step has been incorporated to enhance the readability of the strips.

Fig. 14A and B both show indicators that mutually distinguish methanol (γ = 22.1mN/m), ethanol (γ = 21.8mN/m) and isopropanol (γ = 20.9mN/m). The sample in Fig. 14A consists of two chips, held together: on the left, the letter "M" has been defined in an IOF that is functionalized with 1% 13FS (99% DEC); on the right, the letter "E" has been functionalized with 16.7% 13FS. When the two are submerged together, they read "ME" for methanol, "E" for ethanol and appear blank in isopropanol. In Fig. 14B, the same alcohols are distinguished in an IOF that has been functionalized with a DEC→13FS vertical gradient. In this sample, the IOF thickness increases from the left to the right, thus increased penetration depth of the liquids shifts the colored rainbow to the right. To enhance the readability of patterns produced by vertical gradients, we patterned the functionalized region into an array of "teeth" by selectively oxidizing the background. This patterning reduces a "measuring" problem to a "counting" problem, which is easier to do roughly by eye (*i.e.* without a ruler). Methanol, ethanol, and isopropanol are distinguished simply by counting the number of "teeth" visible. As each "tooth" contains only two or three layer steps, a change in penetration depth of ~1 layer (*e.g.* ethanol vs. isopropanol) induces the disappearance of a large fraction of the third tooth from the left. Fig. 14C shows the same strategy applied to differentiating aliphatic compounds. Distinct "teeth" profiles are viewed in hexane (γ=18.6mN/m), heptane (γ=19.9mN/m), octane (γ=21.4mN/m), nonane (γ=22.6mN/m), and decane (γ=23.6mN/m).

Figure 14D illustrates how regions of uniform functionality and vertical gradients can be combined in the same IOF. The IOF is patterned with two stripes on an oxidized (ROH) background. The rightmost strip is functionalized with 13FS while the leftmost stripe is comprised of a vertical gradient of DEC→13FS. This is accomplished by masking the left half of the IOF during the short oxygen-plasma step. The sample displays one

stripe when immersed in regular unleaded gasoline and two stripes when immersed in diesel. These examples illustrate how a final oxidation step enhances the user-friendliness of WICKs. Through the use of a small legend sheet accompanying the chip, users could compare patterns or simply count the number of visible bars to quickly and reliably differentiate the set of liquids for which a given WICK has been optimized. These examples also illustrate how the design protocols developed in this chapter for EtOH-water mixtures are generalizable to any list of liquids, from pure substances, to complex mixtures.

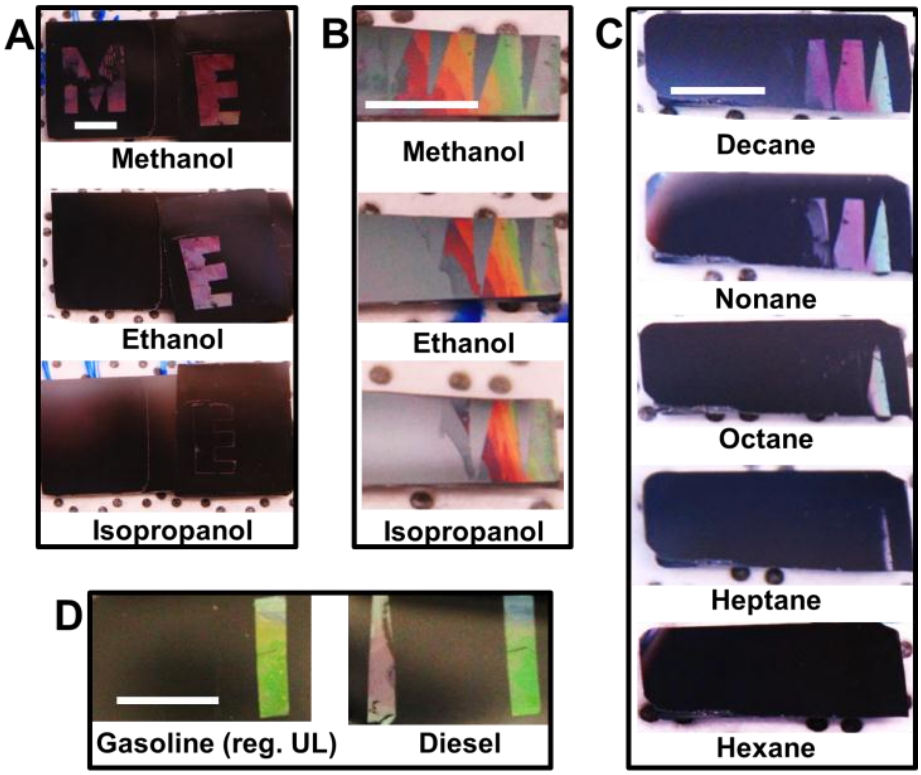

Figure 14. (scale bars: 5mm) (A) Two IOFs patterned with 99:1 and 5:1 ratios of DEC and 13FS are used to distinguish between alcohols. The background of the IOF has been selectively oxidized to reveal "ME" in methanol, "E" in ethanol, and no color in isopropanol. (B,C) Photographs of strips functionalized with a vertical gradient of wettability (DEC→13FS) to distinguish between alcohols and alkanes. An array of "teeth" is oxidized (to render wetting) to make the patterns easier to visibly distinguish. (D) Photographs of an IOF regionally functionalized with 13FS (right stripe) and a vertical gradient of DEC→13FS (left stripe) on an oxidized background, that shows different patterns in regular unleaded gasoline and diesel.

Chapter 4. Enhancing Chemical Specificity

"Mais là, tu dis 'Whoa, une minute Uncle Tom là! 'It's impossible' là!' Mais je comprends parfaitement ton 'skepticism'" – Têtes à Claques

4.1. The problem of chemical interference

In the previous two chapters, we have demonstrated how WICK can be used to differentiate different closely related liquids with remarkable selectivity (ethanol-water mixtures with varying concentrations, different pure alcohols and aliphatic compounds, and different grades of auto fuel). As WICK differentiates liquids based on wettability, a general property of a liquid, this platform could be applied to any class of liquid. However, sensitive response to such a generic property of liquids also means that chemical interference presents a significant challenge in WICK's application to chemical sensing. We envision that the WICK platform could be applied as an inexpensive and easy-to-use field test for: 1) the authentication of liquid formulations (*e.g.* for anti-forgery or quality control) and 2) the identification of unknown liquids (*e.g.* chemical spills, unlabeled containers *etc*.). It is worth making the distinction between these two types of applications because of how the potential for chemical interference influences their applicability.

The key design characteristic that distinguishes liquid authentication from liquid identification is that the target liquid is known beforehand. In this case it is possible, using the techniques presented in this paper, to design a strip that shows one pattern (*e.g.* two stripes) in the target liquid, but different patterns when the wettability is lowered (*e.g.* three stripes) or raised (*e.g.* one stripe) with respect to the target formulation. The fact that a change in the wetting properties of a liquid mixture can be induced by changes in any of the components of a given formulation is actually an advantage of WICK with respect to liquid authentication. An example of such an application would be to use WICK to protect against forgeries of a given pharmaceutical formulation.

Chemical interference is an important limitation to consider when applying WICK's for identification of unknown liquids. As with any sensor that detects changes in a generic property of a substance (*e.g.* density [75,76], pH in pH paper [14]), it is not possible to deduce the specific chemical nature of an unknown without any prior information. However, it is rare that absolutely no information is given *a priori* about an unknown in practice. For example, an unlabeled beaker containing an unknown organic liquid in a lab that commonly uses a finite number of solvents (*e.g.* acetone, isopropanol, hexane) most likely contains one of these. In this case, a WICK designed to have distinct responses only in these liquids would be sufficiently selective to identify the unknown. As is illustrated in several examples in the previous two chapters, this type of indicator could also be useful for rough determination of the relative concentrations of effectively two-component mixtures. Liquor would be an example of this type of mixture, where ethanol and water are the primary components, and the surface-tension contrast of the two components is very high. In this case, we could expect interference to restrict the precision of ethanol concentration measurement somewhat, but not prohibitively, and would also not be able to give any information about the minor components (*e.g.* sugars, *etc*.) unless there was extremely precise prior knowledge of the ethanol concentration.

4.2. Enhanced specificity with arrays

Colorimetry is a powerful form of chemical sensing. Without expensive equipment or extensive training, a colorimetric test gives a user at-home access to increasingly sophisticated chemical and biological diagnostic methods [35-57]. The color response provides an elegant visualization to this class of sensor, but also poses the greatest challenge to its development. While some target properties of an unknown can be easily coupled to color change in an indicator material (e.g. pH), it is generally challenging to couple a colorimetric response that is sensitive to a general physical or chemical property.

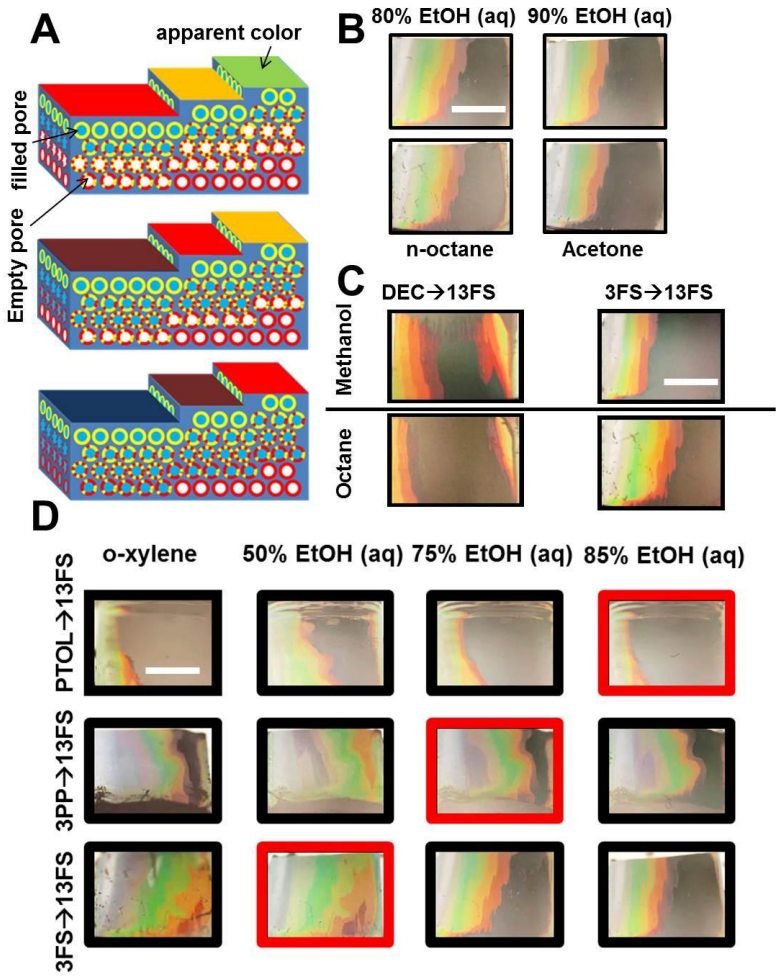

Figure 15. (A) Schematic depicting the color response to partial infiltration of liquids in IOFs with vertically graded wettability. (B) Illustration of the chemical non-specificity of WICK: while the sample shown (3FS→13FS functionalization) shows distinct patterns in 80% ethanol and 90% ethanol, these two color patterns can also be reproduced in entirely different liquids (n-octane, and acetone, here). (C) Chemical specificity derived from a WICK array (WICKAr): Comparison of the color responses of two WICKs (left: DEC→13FS, right: 3FS→13FS) in methanol and octane. The methanol penetrates fewer layers than the octane in the DEC→13FS WICK, but penetrates more layers than octane in the 3FS→13FS WICK. (D) Using reference liquids to assign numerical values to the colorimetric response: The color response of a test liquid (o-xylene shown) in an element in the array is quantified by identifying ethanol-water mixtures that produce the same degree of wetting. In this example, o-xylene is given the following scores: PTOL→13FS: 85, 3PP→13FS: 75, 3FS→13FS: 50. Scale bars: 5mm.

In the preceding chapters, we have developed a platform for colorimetry based on wetting in silica inverse-opal films (IOFs), whose surface chemistry was graded such that the lyophobicity of the porous network increased with depth, which we called a Wetting In Color Kit (WICK). When immersed in a liquid, the structure is infiltrated up to a fixed depth, and displays a structural color pattern that is highly sensitive to the liquid's wettability to the surface chemistry. When this procedure is applied to an IOF that varies in total thickness laterally across the sample (and where the individual layers steps can be seen as regions of distinct color), distinct depths of infiltration can be visualized by a shift in the rainbow pattern corresponding to the number of unfilled layers, as shown in Fig. 15A. Intuitively, this shift will proceed in the direction of the thicker area as more of the lattice is filled.

A scheme of colorimetry that is sensitive to wettability (a generic property of liquids) can be applied in principle to any sensing problem that involves liquids. However, the sensitivity of WICK to such a generic property of liquids also means that no chemical information about the unknown can be discerned without any prior-given information. Fig. 15B illustrates this principle in a WICK, whose vertical gradient of wettability is applied by first functionalizing the IOF with 13FS groups (by exposure to vapors of the corresponding trichlorosilane), then exposing it to oxygen plasma for a short time (30s), and then functionalizing it with 3FS groups (this type of functionalization will hereafter be abbreviated 3FS→13FS, see Appendix A for a more detailed description of this method). While the two ethanol-water mixtures shown (80%EtOH, 90%EtOH) produce visibly distinct color patterns, it is relatively easy to find different liquids whose wetting behaviour exactly mimics those of the above ethanol-water mixtures. In this WICK, n-octane and acetone mimic the response of 80% EtOH and 90% EtOH respectively, as shown in Fig. 15B. In this example, if it is known beforehand that the unknown is a mixture of ethanol and water, WICK would be able to measure the ethanol concentration colorimetrically (with up to 2.5% sensitivity, see Chapter 3). However, if no information is given beforehand, then it is impossible to identify the unknown.

In this section, it is shown that chemically specific information can be extracted from a combination of colorimetric wetting responses displayed by a WICK array, with each element displaying a vertically graded

wettability that is designed to exhibit a partial wetting response in most organic liquids (e.g. surface tension in the 20-30mN/m range), but each using distinct types of surface groups to achieve the wetting gradient. Combinatorial sensing, exploited in our olfactory system as well as by several synthetic systems, is a useful approach to extracting chemically specific responses from an array of individual weakly-specific sensors [1,35,36,64,65]. A wetting-based response is potentially ideal for combinatorial sensing because of the broad range of materials that can elicit the response (any liquid) and its weakly specific dependence on the chemical interactions between the liquid components and the surface chemistry. Fig 15C shows how chemical specificity is added by comparing the responses of two different WICKs employing different surface groups to achieve the wetting gradient (left: DEC→13FS, right: 3FS→13FS) in methanol (γ = 22.1 mN/m) and octane (γ = 21.4 mN/m). In the sample on the right (3FS→13FS) the octane is less wetting than the methanol, showing more colored layers, while the trend is reversed on the left. The combination of patterns in the two samples gives more information about the liquid than one sample alone. For example, a water-dilution of methanol could have produced the pattern mimicking octane at right, but not the one on the left.

We produced WICK arrays consisting of six samples, whose chemistry was vertically graded, each using different surface groups. When choosing the surface groups for IOF functionalization, it was important that all elements produce non-trivial wetting responses in most organic liquids (i.e. partially filled IOFs; trivial responses occur when all layers are filled or all layers are unfilled). To ensure that this condition was satisfied, we used 13FS as the first group deposited on all IOFs, since this functionality, by itself, facilitates a nonwetting response to nearly all liquids. After the oxygen plasma exposure, each element of the array was functionalized with a different (less lyophobic than 13FS) surface group: pentafluorophenylpropyl (5FP), 3,3,3-trifluoropropyl (3FS), n-decyl (DEC), p-tolyl (PTOL), trimethylsilyl (TMS), 3-phenylpropyl (3PP). The plasma exposure time (30s) was chosen to eliminate trivial responses and maximize the range of penetration depths observed in our library of organic liquids.

To facilitate interpretation of the results, we developed a system to translate qualitative wetting patterns to numerical values. Each element of the WICK array was first characterized in a series of reference liquids. To

serve as ideal reference liquids, a set of liquids would have to induce a wide range of wetting responses in each element, ideally covering the broad range of penetration depths observed in test liquids. Most importantly, the relative order of wettability of the reference liquids would ideally be the same in each element in the array. For example, methanol and octane would make a bad set of reference liquids because methanol wets more than octane in 3FS→13FS samples, while the reverse is true in DEC→13FS samples (shown in Fig. 15C). As reference liquids, we chose the set of water-ethanol mixtures (in increments of 5% EtOH by volume) and isopropyl alcohol (IPA). IPA was found to wet more than ethanol in all elements, and is thus a suitable addition to extend the effective range of detectable responses covered by the reference liquids. Color patterns produced by unknown liquids (test liquids) were then assigned a numerical score for each element of the array based on the reference liquid(s) that produced the most similar pattern. The scoring system is illustrated in Fig. 15D for o-xylene as a test liquid, having scores of 50 (3FS→13FS), 75 (3PP→13FS), and 85 (PTOL→13FS) in three elements of the array. To integrate IPA into the scoring system, it was assigned the numerical value of 110. When a test liquid produced a wetting response that fell in between that of adjacent reference liquids, a midpoint score (ending in 2 or 7) was assigned (e.g. a liquid that wet more than 80% EtOH but less than 85% EtOH in a given element would be assigned a score of 82, or 87 for a liquid whose response fell in between 85% EtOH and 90% EtOH).

Fig. 16 shows the complete sample set of color patterns and reference liquid scores from an array tested in 17 different organic solvents. Notably, each liquid yielded a unique combinatorial color response and thus a unique set of scores. Fig. 18A shows the ethanol scores for a wide range of organic solvents in the 3FS→13FS and DEC→13FS elements of the array. Aliphatic compounds displayed higher scores (i.e. more wetting relative to reference liquids) in the DEC→13FS element than they displayed in the 3FS→13FS element. As a general trend, the elements of the array with fluorinated surface groups (3FS, 5FP) produced lower scores relative to the other elements of the array in the nonpolar hydrocarbons, with deviation from the reference line (given by the reference liquids) negatively correlating with polarity of the liquid.

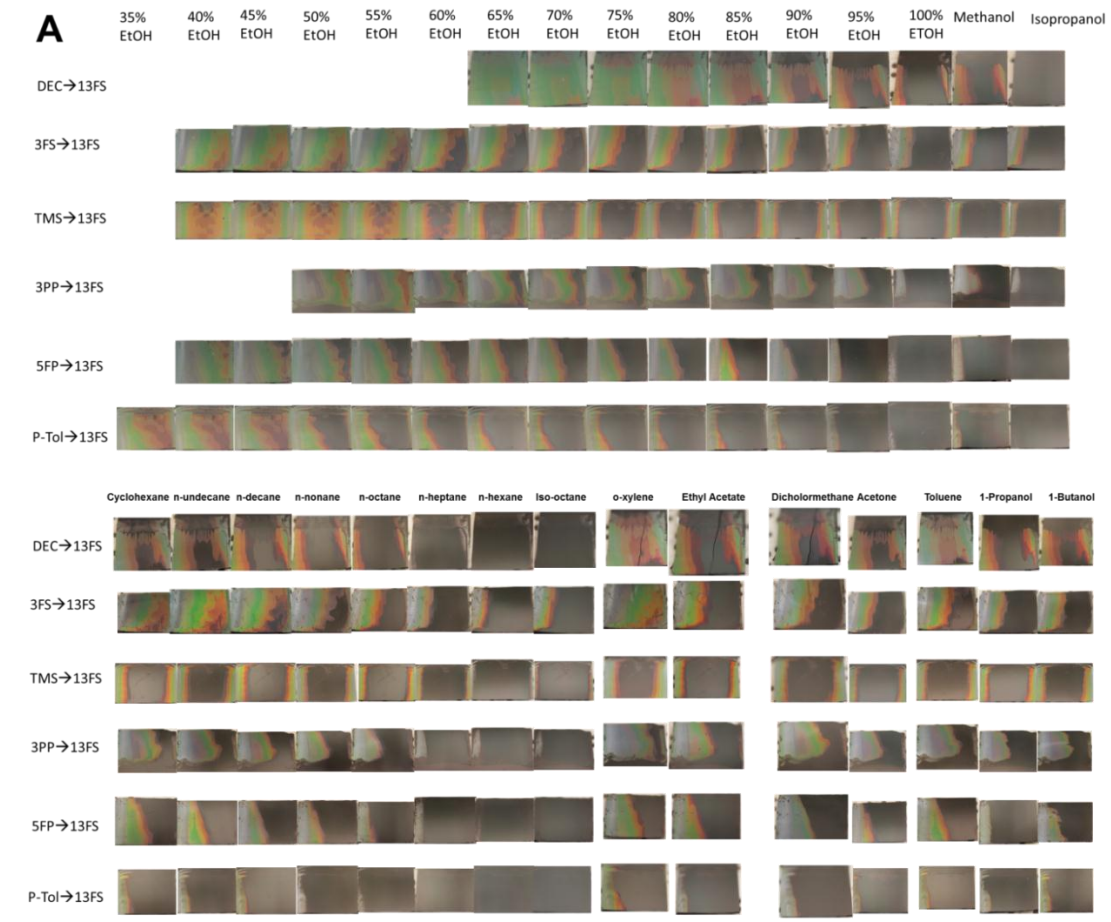

B

	o-Xylene	Dichloromethane	Cyclohexane	Iso-octane	Acetone	Ethyl Acetate
5FP	70	85	80	110	92	87
3F	50	77	50	97	90	82
DEC	87	92	92	105	95	95
P-Tol	85	92	87	110	97	97
TMS	77	87	87	115	97	95
3PP	75	90	82	115	95	95

	n-hexane	n-heptane	n-octane	n-nonane	n-decane	n-undecane
5FP	105	97	92	92	87	82
3F	115	97	80	62	57	50
DEC	110	105	100	97	97	92
P-Tol	110	110	100	97	97	92
TMS	115	110	97	95	92	85
3PP	115	100	97	95	92	90

	Isopropanol	Methanol	1-Butanol	1-Propanol	Toluene	Linear Alkane Mixture (C6-C10)
5FP	110	97	87	95	85	95
3F	110	97	87	92	67	85
DEC	110	97	95	97	85	100
P-Tol	110	97	92	97	95	105
TMS	110	97	95	95	95	100
3PP	110	97	92	97	90	97

Figure 16. Reference liquid scoring system: (A) Photographs of a six-element array, tested in reference liquids (ethanol-water mixtures and isopropyl alcohol) and several organic test liquids. (B) Reference-liquid scores for each liquid extracted from the photographs in (A).

Also as expected, the scores of the linear alkanes in all elements decreased monotonically with increasing chain length (increasing surface tension), since the chemical affinity for the different surface groups should be of the same type. The monotonically varying scores of the linear alkanes form a nearly straight line in this plot.

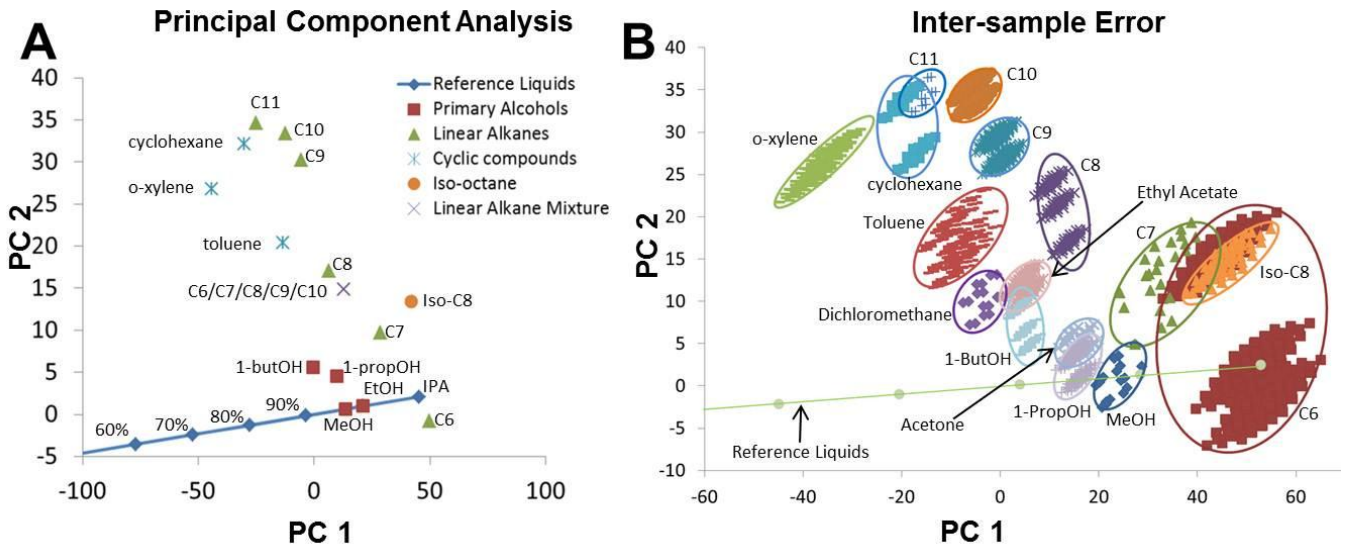

Figure 17. (A) 2D principal component analysis of the reference liquid scores of all six elements of an array, showing differentiation of the different liquid classes. (B) Estimation of inter-sample error using the reference liquid scoring system. Three WICKs with each type of chemistry gradient were tested. All mutually distinct combinations of scores from every possible "array" combination (made by one sample with each chemical functionality) are plotted. There are 729 such combinations possible, however not all produce distinct sets of scores. Although the plot shows the presence of some variability from array to array, the scoring system preserves the general trends that provide chemical information about the unknowns from one array to the next. There are relatively few areas of response overlap between different liquids.

Fig. 17A shows a two-dimensional principal component analysis (PCA) [35,36,64,65] where the aforementioned 6-dimensional set of numerical wetting scores are projected onto a new two-dimensional set of principal component axes (see Appendix B for more detail on our principal component analysis). These two axes account for 98% of the total variance. Qualitatively Fig. 18A and Fig. 17A look similar, indicative of the fact that the contrast between the wetting behaviour in fluorinated and non-fluorinated elements of the array was the largest source of variability between the different liquids. However, the principal component analysis, which

includes contributions from all six elements, is able to distinguish iso-octane and cyclohexane from the linear alkane line. Principal component analyses using fewer elements of the array (Fig. 18B-D) show that even three elements are able to differentiate the 17 test liquids successfully, thus suggesting that the 6-dimensional set is largely redundant.

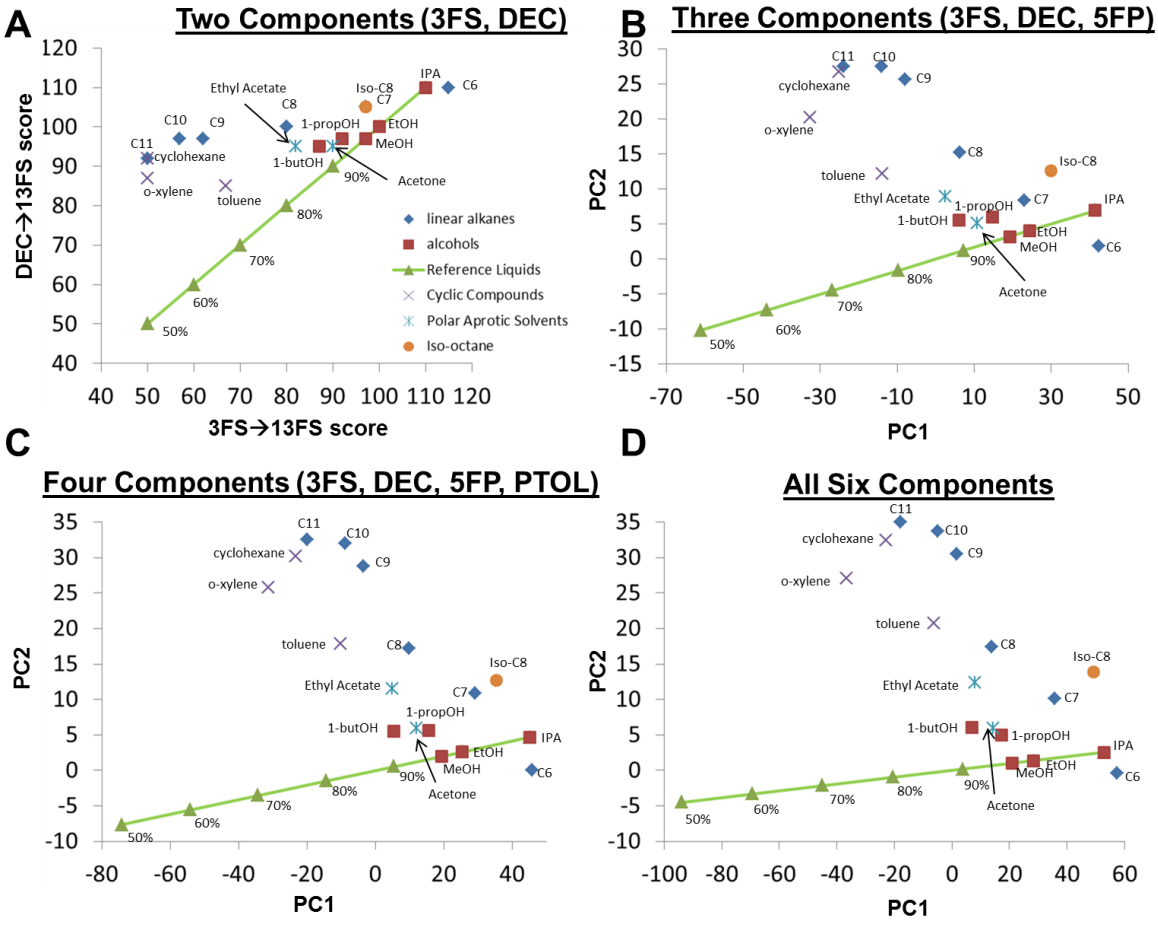

Figure 18. Redundancy of the Array: Comparison of the information given from just two components of a WICK array (3FS→13FS, and DEC→13FS) (A), and 2D Principal component projections of arrays where three (B), four (C), and all six (D) elements are included. Much of the information distinguishing the different types of liquids can be obtained from relatively few elements, meaning that the increased specificity garnered by an array versus a single element can come at a minimal sacrifice in simplicity.

A hallmark of ideal combinatorial sensors is that they give information as to what the chemical makeup

of an unknown (not previously entered in the library) is likely to be [35,36,64,65]. To test the applicability of this principle to our WICK sensor, we tested the array in a randomized mixture of the linear alkanes between C6 and C10. Its response is shown in Fig. 17A. Naïvely, we would expect that its response should fall along the arc (nearly straight line) connecting the responses of consecutive linear alkanes and this is exactly what is observed.

While the sophistication and selectivity of this array-based sensor is below that of many other previously reported "artificial noses" that have a much higher effective dimensionality of the variability [35,36,64,65], the value of WICK array lies in its ease of use and technical simplicity relative to the information it is able to extract. Unlike most artificial noses [35,36,64,65], the reference-liquid scoring system allows measurements to be done easily by eye, by simply comparing the response produced by a test liquid to that of reference liquids. Shown in Fig. 17B, the relative nature of the reference-liquid scoring system also facilitates measurements that are fairly robust against sample-sample variability, potentially eliminating the need for costly quality-control procedures. Notably, unlike previously reported color-based combinatorial sensors [35,36,64,65], it does not require image analysis, RGB subtraction, or any other complex analysis technique that places constraints on the type of equipment amenable for use in the field. Furthermore, as shown in Fig. 18, a significant enhancement of chemical specificity can be achieved by using an array with only two or three elements. This requires a minimal increase in complexity compared to the original WICK litmus paper concept.

Using arrays of WICKs, each with distinct chemical functionality, but exhibiting a nontrivial wetting response over a common range of liquids, we are able to extract chemical specificity from a sensing platform whose widespread applicability is derived from sensitivity to wettability, a general (non-chemically specific) property of all liquids. Furthermore, through the use of a simple-to-use reference-based scoring system, we are able to translate qualitatively perceptible degrees of wetting to numerical values that can be assigned by eye (using a reference card), without the need for sophisticated equipment or software, in a manner that simultaneously desensitizes the system to inter-sample variability. In addition to the ability to differentiate a wider range of liquids, our WICK arrays also allow users to make rough predictions about the chemical nature of a previously uncharacterized unknown liquid by comparing relative degrees of wetting of the different elements.

4.3. Drying in color: Further differentiation of liquids based on volatility

At the beginning of this thesis, we motivated the development of WICK in the broader picture of developing a simple field-test technology that allows one to gain as much information as possible about an unknown liquid. We identified specific performance ideals for the technology, most importantly: i) the sensing mechanism had to be very simple, low cost, portable, and easy to use; ii) without requiring a significant sacrifice in the previous category, the specificity (the amount of information on the unknown discernible from a measurement) of the sensing platform should be as high as possible; iii) we wanted the technology to be applicable to a broad range of sensing problems. We satisfied requirement iii) by choosing a generic property of liquids (wetting) as the basis for a colorimetric response. In Chapters 2 and 3, we showed that a highly selective colorimetric response to wettability existed in highly symmetric IOFs with spatially patterned surface chemistry. This formed the basis for our Wetting In Color Kit (WICK) technology. WICK, as it stood at the end of Chapter 3, had satisfied ideals i) and iii) very well, however, as was pointed out in the beginning of this chapter, it lacked in specificity. This was a direct, but unfortunate consequence of choosing such an inherently weakly-specific property of liquids as the basis for sensing. The general question addressed in this chapter could be expressed as "How can the specificity be improved without significantly sacrificing its simplicity?"

In the previous section, we showed how comparing responses from a few WICKs with different chemical bases provided chemically specific combinatorial signatures. It is well-known that combinatorial analysis is a good way to extract specificity from weakly specific measurements [35,36,64,65]. The specificity of an array of weakly specific measurements scales with the effective dimensionality of the array, that is the number of principal components that encompass all or most of the variability in the responses [65]. Another way to think of the effective dimensionality is it is a measure of how different the measurements in the array are from one-another.

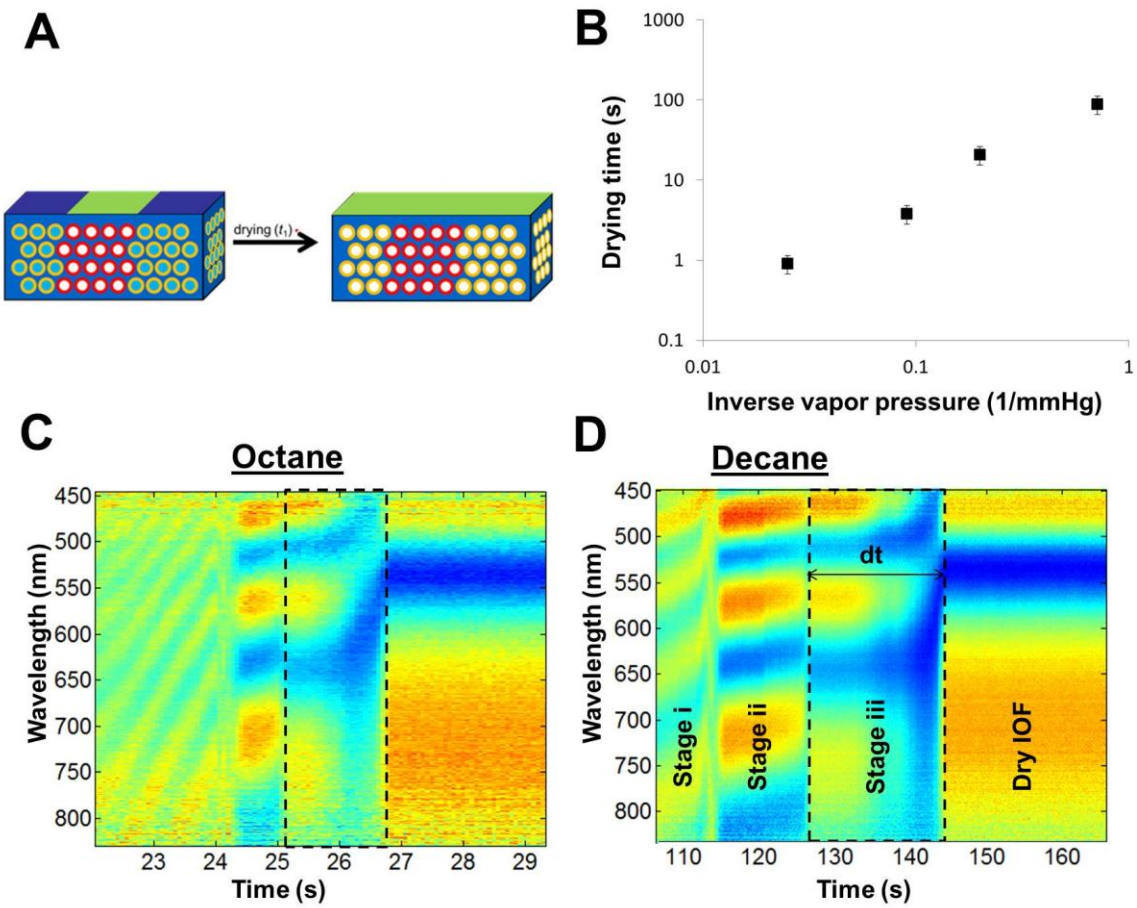

Figure 19. (A): The drying in color concept: (A) In addition to the information on a liquid's composition offered by WICK's colorimetric sensitivity to wettability, additional information about a liquid can be derived from a WICK (or WICK array) by measuring the time it takes for the sample to dry. As drying correlates with the reappearance of color in the originally wetted regions, the drying time in samples which are wetted in a reproducible manner can be estimated by eye, providing a crude measure of the volatility of the liquid in addition to its wettability. (B) Average drying times for linear alkanes C6-C10. To remove most of the liquid over-layer, the IOF was flushed with water (which does not wet the pores, nor is miscible with the alkanes) immediately after being flushed with the alkane. (C,D): Time-resolved spectral evolution of an IOF (uniformly functionalized with DEC groups) that is drying after being exposed to n-octane (B) and n-decane (C). The spectral evolution during drying displays several distinct stages: i) the 'thick-droplet' phase, ii) the thin-film overlayer phase, and iii) the pore emptying phase. Stage iii, indicated by the dashed box (presumed to start at the point where the top of the IOF becomes exposed to the air) shows the same spectral evolution in both cases. In fact, the spectral can be perfectly overlaid in this region if by expanding the time-frame of octane to fit that of decane.

For example, in the WICK arrays described in the previous section, it was found that the majority of the variability (and thus the chemically specific new information) could be derived from looking at two elements, one containing a fluorinated second surface group and the other without one (e.g. 3FS→13FS, DEC→13FS). These produced different behavior because of the difference in relative affinity to polar and aliphatic liquids.

However, since all elements of a WICK array measure wettability (intrinsic contact angle between a liquid and a surface chemistry) certain information (e.g. the general trend of decrease in wetting with increasing surface tension of the liquid) is inherently redundant. If the effective dimensionality of WICK arrays is inherently limited, one simple way to greatly increase the specificity of the platform would be to find additional, equally generic, but orthogonal properties of liquids that can be easily estimated with WICK. While the unique properties of the WICK platform enable highly selective wetting measurements, a selectivity/sensitivity that would not necessarily extend to measurements of other properties, even a very crude measurement of an orthogonal property might add great value to a WICK array measurement. This is because we would already have the specificity of the WICK array to build on, and so this orthogonal measurement might only need to help the user tell the difference between two specific liquids (e.g. n-undecane and cyclohexane) that happen to have overlapping combinatorial wetting signatures.

We note that colorimetric wetting information from WICK (or WICK arrays) can be complimented in the same platform, simply by taking note of time-dependent phenomena that occur as a wetted IOF dries. The simplest and most obvious observation to make is that more volatile liquids dry more quickly, and thus recording the drying time will provide at least a coarse indication of volatility. Drying of a wetted IOF (or most other surfaces) typically occurs over timescales that are sufficiently slow to measure with a stopwatch with some relative degree of precision. Furthermore, the structure couples the drying process, the inverse of the wetting process, to an easy-to-read color change (the reappearance of color, shown schematically in Fig. 19A).

To design as accurate as possible of a drying measurement based on WICK, we must be mindful of the fact that this is a measurement that is likely to be much more sensitive than wetting to ambient conditions (e.g. airflow, humidity) and initial conditions (how much liquid is on top of the pores). While recognizing that crude

measurements may still give very useful information, when added to a WICK array response, it is in our best interest to try to control some of these variables where possible.

The first variable we aimed to control was the volume of the liquid in the pores. Fig. 19A shows the drying time recorded for the linear alkanes C6-C10. To limit the variability in amount of liquid above the pores for this experiment, we adopted the following procedure: The IOF was uniformly functionalized with DEC groups. The functionality was chosen such that water would not wet the structure, but most aliphatic compounds could penetrate the pores. The IOF was first exposed to the aliphatic compound by flushing with a syringe, and then immediately flushed with water while held at a tilt angle. The water, both immiscible with the alkanes and unable to penetrate the pores served to flush off as much as possible of the alkane over-layer, while preserving the alkane layer inside of the porous network. Drying time was measured from the end of the water flushing step until the time that the IOF color had completely returned (no visible trace of pore-filling). Video analysis was used to ensure accurate drying times. Fig. 19B shows a plot of the average drying times and variability for linear alkanes C6-C10. As expected, an inverse monotonic correlation was observed between volatility and drying time. For this type of measurement, in a single environment (all measurements were done on the same day at the same lab location), an average error of 26% was observed.

Time-resolved spectra of the IOF during drying were taken and shown in Fig. 19C,D for octane and decane. Across all four liquids the spectra show three common phases: i) the ‘thick-droplet’ phase, ii) the thin-film overlayer phase, and iii) the pore emptying phase. While not necessarily informative for our discussion of liquid identification, it is worth briefly discussing the information given by these spectra, because they reveal information about the general dynamics of drying porous films, and could serve to validate current models that describe this type of phenomenon [78]. Phase i) is characterized rapidly changing and very closely-spaced reflection peaks, consistent with interference fringes from a ‘thick’ film. Phase ii) begins with a sharp collapse in the thickness of the film. This may be evidence of a bistable film thickness, where the thick films can be considered thin droplets that leave behind a much thinner film as they recede. The abruptness of this transition is consistent with such receding drop behavior.

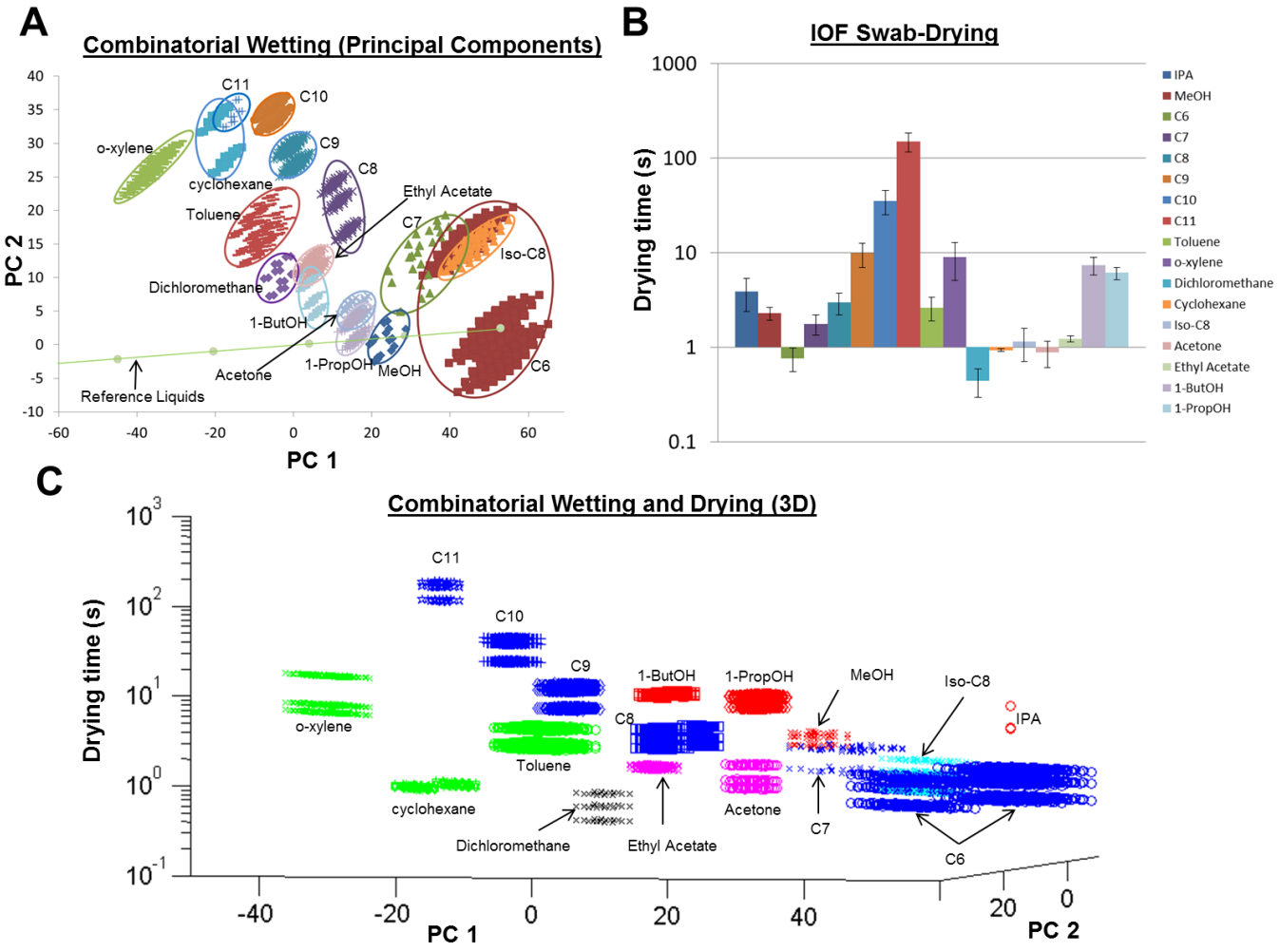

Figure 20. Drying time of an IOF (ROH-functionalized) as an added "element" of a WICK array (A): A reproduction of Fig. 17B (reproduced here for easy comparison with drying results), showing, with error, the ability of WICK arrays to differentiate 17 different organic liquids based on wetting. (B): Average drying time (standard deviation shown as the error bar) of the same liquids after swabbing an IOF uniformly functionalized ROH. (C): Data from (A) and (B) shown as a 3-dimensional plot (the two principal components of the 6D WICK array measurement with IOF drying time as the z-axis). All combinations of individual wetting (729 in total per liquid) and drying (3 per liquid) measurements are shown as distinct points on the graph to estimate the volume in this parameter-space covered by a given liquid. With the exception of n-hexane (C6) and iso-octane, all of the liquids occupy a mutually exclusive volume in this plot. Most notably cyclohexane and n-undecane (C11), having overlapping wetting profiles, have drying times that differ by several orders of magnitude (cyclohexane is much more volatile). Color scheme: blue-linear alkanes, red-alcohols, green-cyclic compounds, magenta-polar aprotic solvents, cyan-iso-octane, black-dichloromethane.

This type of bistable thickness is not unusual for liquid films on surfaces [62,79]. Since the IOF and these liquids are refractive-index-matched, any state in which all of the pores remain filled (with or without an over-layer) should display a reflection spectrum of a simple thin film, with associated interference fringes. Therefore thinning of the over-layer during drying should show up spectrally as continuous shifting and spreading of equally-spaced reflectance peaks. With the exception of the abrupt transitions between stages, the spectral evolution within stages i) and ii) is consistent with this picture.

We attribute the beginning of stage iii) to the disappearance of the over-layer and the beginning of the pore-emptying process. We know that stage iii) ends with the film completely dry because all spectral changes cease at its end and the spectra matches that of the dry film. The spectral evolution during this phase proceeds differently from the others and possesses some unique characteristics that are seem to be liquid-independent. In particular, by choosing the correct relative time-rescaling, corresponding spectral maps from different runs, even when different liquids are used, can be nearly perfectly superimposed.

The evolution is characterized by both spectral shifts and a washout of the reflection peak/through contrast during the intermediate stage between the completely filled and completely dry states, both of which are characterized by pronounced reflection peaks. This is consistent with an expected increase in the degree of disorder in partially filled photonic crystals. Qualitatively, reduction in peak/trough contrast is expected with decreased spatial coherence of the light scattering since the structural bias toward certain length-scales washes out. We also expect the degree of disorder to be maximal at an intermediate degree of filling, since both the completely empty and filled lattices are perfectly ordered structures.

While the water-flushing technique incorporates a measure to somewhat control the liquid volume in the pores at the start of the drying (it eliminates the presence of large droplets), it possesses the significant drawback that it can only be used on test liquids that have no miscibility with water. Granted that it also does not produce impeccably small errors, we sought out simpler techniques that might display comparable degrees of variability, but be applicable to a broader range of liquids. Perhaps the simplest method to wet an IOF with a thin film of

liquid (without leaving behind large droplets) is to swab it with a cloth that is damp with the test liquid. Samples were wiped with a lint-free wipe from one side to the other with sufficient pressure to ensure that large droplets were not left behind. Drying time was measured (video analysis was used to ensure accuracy) from the time the wipe left contact with the sample to the time the sample was completely dry. All measurements were done on the same ROH-functionalized IOF in the same ambient environment.

Fig. 20 shows the average drying time (standard deviation shown as error bars) of three runs using the 17 test liquids used in the previous study of WICK arrays. The maximum variability measured in drying times for a single liquid was 43%. The drying times are compared with the combinatorial wetting measurements of the same liquids from the previous section. Despite the relatively large relative error, the drying times actually add information that makes easily-distinct some liquids that had overlapping ranges of response across several combinatorial wetting measurements. The most notable such example is n-undecane (C11) and cyclohexane. While their wetting profiles largely overlap (Fig. 20A), their vastly different volatility results in drying times that differ by more than two orders of magnitude. Fig. 20C shows the liquid test results expressed in a three-parameter space, consisting of the two principal components of the combinatorial wetting measurement with the drying time as the third axis. To give an estimate for the maximum total volume covered by each liquid in this parameter space, all possible combinations of the 7 measurements (6 elements of the WICK array + drying time) for three repeats of each are plotted as separate points. Inclusion of the drying data results in a significant improvement in the separation of the liquid responses; with only n-hexane and iso-octane as the only remaining liquids with significant overlapping volume (separation between the other apparent overlaps visible in Fig. 20C can be seen by rotating the plot).

Despite its weak specificity (further weakened by large variability in measurements), measuring the drying time of an IOF adds valuable information to a combinatorial wetting profile from a WICK array because it measures a separate, largely independent, property of liquids. The utility of this added parameter may be most pronounced in the identification of mixtures. Fig. 21 shows the comparison of a WICK array wetting profile and the drying times for several different grades of gasoline from different stations (Mobil and Shell gas stations), a

sample of diesel fuel and our randomized C6-C10 alkane mixture from the previous section. As an aside, one noteworthy trend, visible in Fig. 21A is that the wetting response of the gasoline samples was more closely tied to their source (Shell or Mobil) than to their grade. Comparing diesel with our alkane mixture, we see that they exhibit markedly similar wetting responses, yet their drying times differ by nearly 2 orders of magnitude. Drying may be a particularly useful additional measurement to make when trying to identify or authenticate types of petrol, since they are often specifically defined by their volatility in manufacturing, as a fractional distillation of crude. On the other hand, as evident in Fig, 21A, an individual grade (e.g. premium unleaded) may often have variable wetting properties from sample to sample, or from source to source.

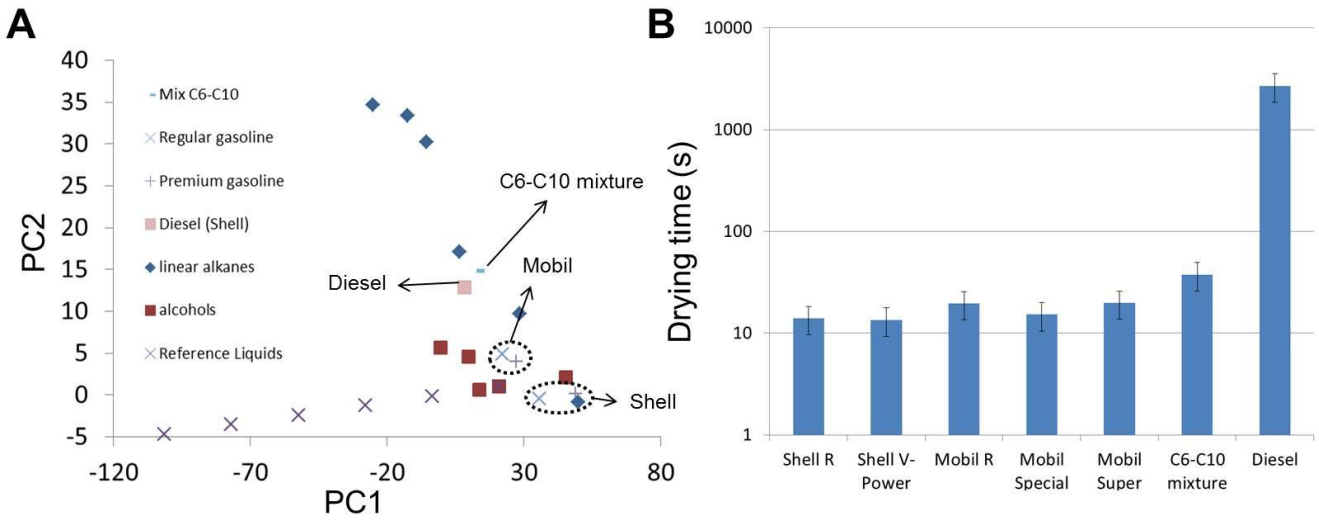

Figure 21. Comparison of WICK array wetting (A) and drying times after swabbing (B, ROH-functionalized IOF) of regular and premium gasoline from two different sources (Mobil and Shell), diesel, and our randomized mixture of linear alkanes C6-C10 from section 4.2.

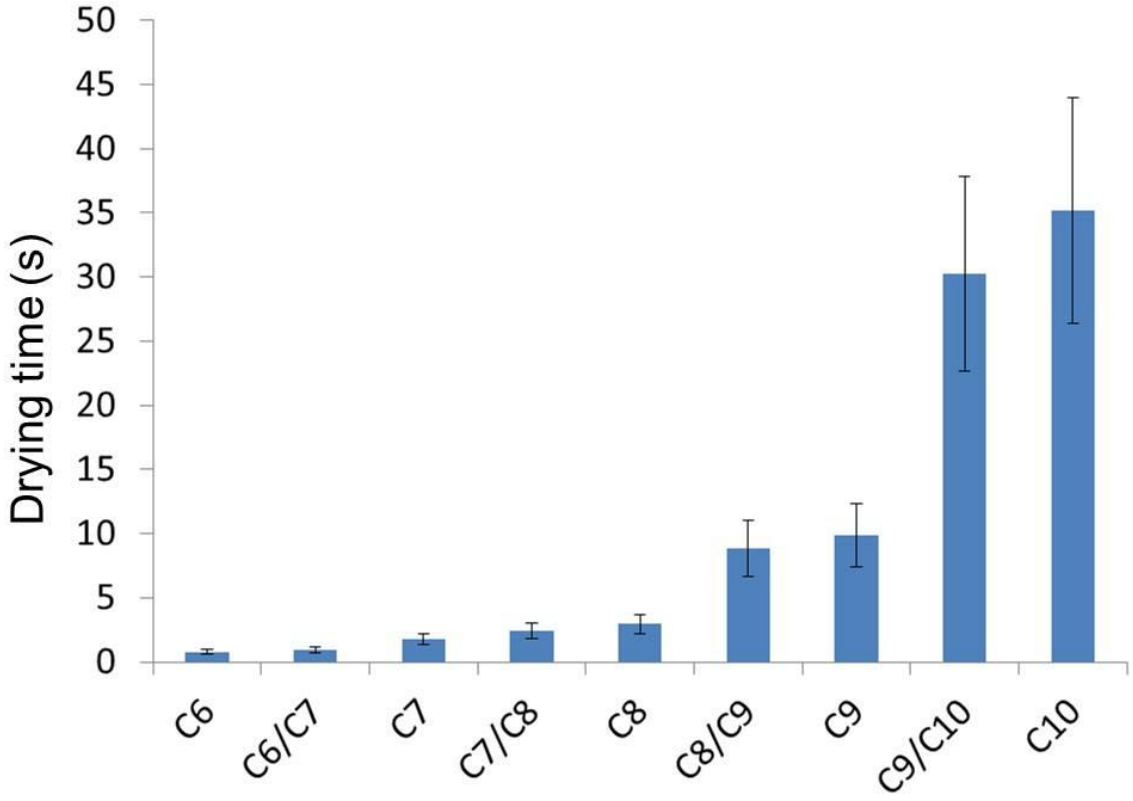

Figure 22. Comparison of drying times in a IOF (ROH functionalized, wetted by wiping) for linear alkanes from C6-C10 and 50:50 mixtures of different alkanes. Particularly for the more non-volatile compounds, drying times of the mixture was closer to that of the less volatile component.

While one could imagine a variety of factors being influential in the wetting response of a mixture (e.g. the presence of even a small amount of surfactant), we expect the total drying time to be most heavily influenced by the least volatile major components. Thus wetting and drying measurements may give vastly different results relative to other liquids. For example, diesel fuel, typically containing aliphatic compounds in the C8-C21 range [80], shows a wetting signature resembling that of octane, but takes about 45 minutes to dry, over an order of magnitude longer than n-undecane. Fig. 22 compares the drying times (measured in the same IOF as above) of 50:50 mixtures of linear alkanes with the corresponding pure liquids. Particularly pronounced for the longer-chain, less-volatile liquids, the drying time of the mixture is closer to that of the less volatile component.

By looking at how fast an IOF dries after being wetted by a liquid, we add an additional dimension to a combinatorial wetting measurement from a WICK array. While the specificity of the drying time measurement is

reduced by the inherent sensitivity of drying time to the precise initial conditions associated with wetting the IOF, it provides valuable additional information based on sensitivity to a properties of the liquid that are more decoupled from what is probed by the WICK array. This additional degree of freedom may be helpful in identifying mixtures, particularly if different components of a mixture have the largest effects on the wetting and drying responses respectively. Furthermore, similar to the combinatorial wetting approach discussed in the previous section, the improvements in specificity offered by this approach come at a minimal cost in terms of simplicity and cost (the major addition is the requirement of a stopwatch or other time-measuring device). One potential shortcoming of the particular wiping technique used above, is that it has the tendency to cause damage to IOFs after repeated wiping. This would limit how many times an IOF could be used in the field for that purpose. However, in the absence of expensive cleaning supplies, wetting measurements in the field will be only practical for one-time use anyway.

This brief study of drying in IOFs also motivates further studies on dynamic processes associated with the interaction between a fluid and a porous photonic crystal, both from a scientific and a technological standpoint. From the scientific standpoint, the liquid-independent evolution of the reflection spectrum as the pores empty during drying suggests that this phenomenon could be described by a relatively simple percolation model. A better understanding of the partial filling statistics (the distribution of filled pores) at various intermediate time-points would allow us to learn more about the role disorder plays in the modifying the optical properties of a photonic crystal.

From the point of view of development of simple and inexpensive techniques for fluid identification, monitoring of dynamic wetting processes that cause the color response of a WICK to change over time (resulting from an increased degree of wetting) may yield powerful new information in some liquid mixtures. Although having not conducted an exhaustive search, we have found relatively few cases where such a change can be observed. For example, we have not observed time-dependent wetting in our WICKs in ethanol-water mixtures. We reason that this is because wettability is expected to decrease over-time as the more volatile alcohol evaporates more quickly than the water. Since the observed wetting in IOFs is governed by pinning and

metastable non-wetting states, we generally expect that only an increase in the degree of wetting could be observed as a color that changes over time, as a decrease in wetting is generally energetically unfavorable. For most liquids of the same class (e.g. linear alkanes) the surface tension and volatility generally correlate inversely, meaning that in mixtures thereof, the surface-tension would also tend to increase over time (thus decreasing the wettability to most surfaces) as the volatiles evaporate first. In these cases, we would not expect to observe dynamic wetting behavior in a WICK. However, when mixing liquids of different classes, it should be possible to find miscible combinations of liquids where the surface tension of the mixture is expected to decrease over-time as the volatile component started to evaporate. One only has to look at Fig. 20 to make good guesses as to which combinations might work. Fig. 23 shows one such example, a mixture of acetone (γ = 23.6 mN/m, VP = 184 mmHg [81]) and octane (21.4 mN/m, VP=11 mmHg [81]). After a WICK functionalized DEC→13FS is left in the mixture for 24 minutes the number of non-wetted layers noticeably decreases.

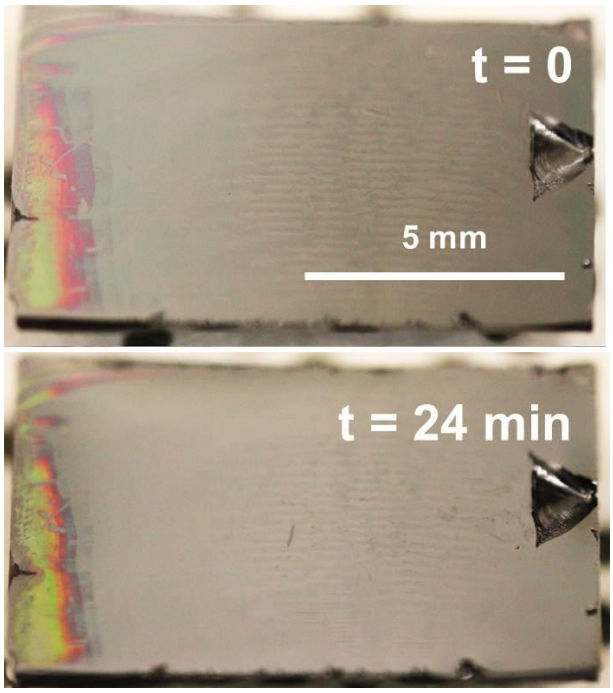

Figure 23. Dynamic wetting in a mixture of acetone and n-octane in a WICK functionalized DEC→13FS.

Chapter 5. Discussion: Opportunities, Limitations, and Extended Applications

"Destroy 99% of household pests with pre-sliced, rust-proof, easy-to-handle, low-calorie Simpson's Individual 'String-ettes', free from artificial coloring, as used in hospitals!" – John Cleese, Monty Python

5.1. Outlook: Sensing

In the last three chapters, I have described in detail the performance capabilities of the Wetting in Color technology in the context of sensing. From a technical standpoint, the system has been characterized in detail and performance characteristics (e.g. selectivity, specificity) have been demonstrated for a few specific examples (determination of the relative concentrations of an ethanol/water mixture, differentiation of simple pure organic solvents). In this section, I discuss the vision of practical implementation for the WICK sensor. Using specific examples of how WICK could be applied to sensing problems for-which preliminary commercial interest in our technology has been expressed, I will highlight what I think are the strengths and weaknesses of this approach, and how they may compare to existing approaches. In general, WICK can be used as a sensor in one of two ways: 1) authentication of known liquid formulations; or 2) identification of unknown liquids.

WICK as a Liquid Authentication Device

As an authentication device, WICK somewhat benefits from the inherent chemical non-specificity of a wetting-based measurement. For this type of application, it is assumed that the 'correct' liquid formulation is a known quantity. A WICK would be designed to display a specific pattern in the known formulation, and a different pattern in incorrect formulations (either due to forgery attempt or poor quality control of the formulation). To make a WICK best serve this purpose, wettability thresholds for some regions of the IOF would

have to be designed to exist very near the properties of the known ‘correct’ liquid formulation on either side. The goal is to make the smallest change possible to the formulation (that either increases or decreases the wettability) result in the appearance of a different pattern (either a greater or lesser extent of wetting). The strengths of this authentication approach are its simplicity and portability. It would be relatively straightforward to incorporate a small WICK into the packaging of a liquid product along with a small sticker showing the authentication pattern for comparison (an IOF could even perhaps be grown on a sticker placed directly on the packaging). Putting a drop of the liquid on the WICK would provide an instant, simple measure of the formulation quality.

For this type of application, it is likely to not be chemical specificity, but rather quality control that most limits the performance and applicability of WICK. Let us consider first chemical specificity. In the example in Fig. 15B, it was shown how a WICK designed for differentiating different ethanol concentrations in water could be ‘fooled’ by completely different mixtures, mistaking acetone and n-octane for 90% and 80% ethanol. If this single WICK was used for the purpose of authenticating the ethanol concentration of an aqueous mixture (for example, in liquor), then it is highly unlikely that the liquid will turn out to be something completely different (e.g. one will probably not find pure acetone in the bottle). From an initially infinite array of possibilities, the response of single WICK measurement narrows (within its error) the possible formulation down to a smaller subset of liquids with matching wettability to the particular chemistry gradient used. However, the more precise this single measurement is, the more different the chemical nature of two liquids that produce the same pattern are likely to be.

For example, outside of the range of error, one would not expect two different ethanol-water mixtures to be able to produce the same pattern in any WICK. To mimic the authentication pattern with an incorrect ethanol concentration in that example, one would probably have to add a third liquid (e.g. methanol) with a very specific concentration. In general, a sensitive, but poorly specific indicator such as WICK is expected to do a better job at identifying the liquid with every extra piece of prior information as to the rough chemical composition. In an authentication setting, usually the deviations from the correct formulation are expected to be relatively small. This means that there is much prior information about the liquid formulation. However, assuming that a liquid

authentication device needs to be able to identify small deviations from a known formulation, sensitivity and quality control are likely to be important sources of limitation. While a cost-effective quality-control procedure was implemented in Chapter 3 based on post selection, and resulted in the loss of only ~1/3 samples, we have yet to study scale-up protocols and their potential impact on the variability of our pore geometry.

It may prove difficult to practically implement WICK as a field-test for authentication of complex mixtures, particularly those in which the chemical composition of a 'good' sample can vary enough to produce a wide range of wetting responses (gasoline is one good example). As shown in Fig. 21 for example, gasoline samples from different sources differed more from each other than gasoline samples of different grades from the same source in the responses of a WICK array. In this example, WICK may not be a useful test for authentication of gasoline grade quality since the definition of 'good' quality fuel is independent of wetting properties and surface tension, and wetting properties of 'good' quality gasoline shows a fairly large variability of response in WICK measurements (Fig. 21). On the other hand, in some complex mixtures such as liquors, limited authentication (e.g. a rough verification of ethanol concentration) could be possible if the wetting properties are likely to be predominantly controlled by the concentration of one or two components (e.g. ethanol for liquors).

This approach to liquid authentication would have to compete in the marketplace with several other competing technologies, most-notably additives used as tracers, which can be easily identified (e.g. by fluorescence) [82]. The detection of injectable tracers is decoupled from the composition of the liquid, which can be an advantage for authentication of compositionally variable liquids such as gasoline. Tracer additives can act as a signature of the supplier, validating that the product is in fact coming from them and that it passes their quality standards. The presence of such tracers also makes forgery difficult. One tradeoff is that the verification of these tracer molecules/nanoparticles by the user requires a more sophisticated measurement than the simple colorimetric response of WICK, thus limiting the number of customers that can perform the validation.

WICK as a Liquid Identification Device

For application as a liquid identification device, chemical specificity of the WICK indicator(s) is likely to be the most important limiting property. While it is unlikely that there is absolutely no prior knowledge about the

possible composition of an unknown sample in practice, there is certain to be more possibilities than there would be for a liquid-authentication application. The less there is known about the liquid in advance, the more important the specificity-increasing measures discussed in Chapter 4 (combinatorial measurements with WICK arrays and monitoring of dynamic behavior to elucidate rough estimates of orthogonal properties such as volatility) will be in extracting any useful information from this technology.

Using the identification of the contents of an un-labeled beaker in a chemistry lab as an example, I envision the ideal practical application of the technology to resemble the following general form: 1) A WICK array, where the gradients of wettability are optimized as in Chapter 4 to respond to a broad range of liquid surface tensions, would first be used to map the response of the unknown liquid against a library of known chemicals (e.g. Fig. 17). This would be used to gain rough information about the chemical class of the unknown (e.g. it is probably aliphatic, or an alcohol, etc.). Depending on how little is known beforehand (e.g. what is the total inventory of chemicals known to exist in the lab), the WICK array could be supplemented with a timed drying to further group the unknown. 2) If necessary, fine-scale differentiation between closely related liquids (e.g. beyond the selectivity of the WICK array, which was optimized for dynamic range) could be done with a second WICK (single sample) that is optimized for selectivity rather than dynamic range.

A WICK could be optimized for dynamic range by making a vertical gradient of wettability in a thick sample using a long plasma-exposure time, where the two surface functionalities have vastly dissimilar wettability. On the other hand, a WICK could be optimized for selectivity (at the expense of dynamic range) by applying a vertical gradient of wettability using two very similar surface groups. Comparing Figs. 13 and 15, one can see the tradeoff between selectivity and dynamic range. In the WICK shown in Fig. 13, a 2.5% change in ethanol concentration produces a shift in the infiltration pattern by 1 layer step, but non-trivial responses are only observed for a range of ethanol concentrations spanning about 10%. In the WICK shown in Fig. 15 the same single-step shift is accomplished by a 10% change in ethanol concentration indicating a poorer selectivity. On the other hand, nontrivial responses are observed over a concentration range of nearly 50%.

In comparison to other means of analyzing similar compounds (e.g. identifying an unknown organic liquid), simplicity and cost are the main advantages of this approach. If performance enhancements (e.g. to sensitivity or specificity) came with significant tradeoffs in simplicity, cost or portability, the sensitivity and specificity required for practical use would then have to compare to the many established and sophisticated laboratory-based technique (e.g. mass-spectrometry). On the other hand, in its current form, there are no currently-existing technologies that can be used with the same degree of simplicity and portability that can be applied to as broad a range of compounds. The best applications are those where a simple end-user analysis would be useful, and the specificity or sensitivity requirements are not that high (i.e. one can probably forget about using WICK to detect ppb-levels of a contaminant). In my opinion, the most promising current application, from the standpoint of technical feasibility, is the use for identifying unknown organic solvents in a lab or workplace setting. In this type of setting, the number of possible liquids that could make up the unknown is not likely to be prohibitively high, with a low likelihood of encountering mixtures with the compositional complexity of something such as diesel fuel. This type of setting is also one that currently sees widespread use of pH-paper as a simple diagnostic for acid-base discrimination. Using WICK for identifying hazardous organics shares many of the advantages that pH-paper has for acid-base discrimination (simplicity, cost) as well as the drawbacks (poor chemical specificity). The widespread use of pH-paper in this setting suggests that a sizeable market could exist for WICK.

The next step of development required for practical application of this technology in the commercial world is the scale-up of the co-assembly fabrication protocol [59]. We are capable of synthesizing very high-quality IOFs, suitable for very high selectivity of wetting, however we currently can only produce six ~1cmx5cm films in one batch. The deposition, as it takes place by evaporation, is also very slow (takes 1-2 days on average, see Appendix A). While there are many different protocols we could use for scale-up, such as dip-coating with controlled withdrawal speed [83] (this also allows thickness-control), or spin-coating a suspension containing the polymer microspheres and the silica precursor [84], how the quality and the regularity of these films would be affected by these protocols, and how the colorimetric wetting selectivity would be affected, has not been studied.

5.2. Extended applications

Thus far, the central focus of this thesis has been the study of highly selective wetting in inverse opals and its relation to the displayed structural color, with particular emphasis on applications in colorimetric sensing. This section describes other applications of this platform, not directly related to colorimetry, that we have explored. Broadly speaking, there are two fundamental original scientific advances that underlie the results presented in this thesis. The first is the discovery that defect-free inverse opals display a remarkably consistent and abrupt threshold wettability for infiltration of the pores, which due to the highly re-entrant geometry at the inter-pore necks, occurs in a surprisingly low range of intrinsic contact angles ($\theta_c \sim 20°$). Secondly, to facilitate greater manipulation of wetting, we have developed several straightforward protocols to spatially pattern the surface chemistry of the porous network in 3D. In addition to colorimetry based on wetting, these advances may be useful to several unrelated technological problems.

The ability to encode complex chemical information in a single system underlies much of modern technology, from encrypting messages and data [66-68] to designing sensors that can distinguish among a wide range of stimuli [35,36], to creating templates that direct the assembly or growth of materials [60,61,69-71,85-89]. The development of self-assembled monolayers (SAMs) [69,90,91] as a means for generating intricate surface chemical patterns, combined with the vast array of available chemical functionalities, has greatly expanded the capacity for embedding chemical information on 2D surfaces [60,61,69-71,85-91]. However, extending chemical patterning of this nature to 3D surfaces would not only enable much higher complexity but would introduce an entirely new range of properties that arise from the 3D configuration. In particular, the surface area of 3D microporous materials confers material properties that are useful for many applications in optics, scaffolding, energy storage, catalysis, etc. [20,22,92,93]. While recent advances have enabled the fabrication of porous films with increasingly complex 3D architectures and function [20-22,92,93], to our knowledge, a versatile technique for local patterning of multiple, site-specific, arbitrary surface functionalities in their pores has yet to be developed prior to this work, and thus this the techniques developed here to generate highly controlled

an spatially diverse surface chemistry within 3D porous structures may be useful in some of these areas. In the following sub-sections, I list a few that we have briefly explored.

Multi-level Encryption

As was briefly discussed at the end of Chapter 1, one direct application of the technology developed here that is unrelated to sensing is multi-level encryption (W-Ink). An encryption device really works in the same way that a sensor would: different optical messages are revealed in response to different liquids, all of which would be invisible when the sample is dry. In principle, any device that displays a previously-encoded visual response to a stimulus can be considered an encryption device (the same can be said about sensors!). One consequence is that there are many other ways to make an optical encryption device. Encoding of secret messages for security or authentication applications is a very crowded market with many technological options available [27,66,67,68,94,95]. It is worth listing the pros and cons of W-Ink against the plethora of other options available for encryption to assess the viability of this technology in this market.

The unique feature of this approach to encryption that could be advantageous for some applications is that it is a form of multi-level encryption. It is relatively easy to encode a large number of different messages (at least as many different messages as there are distinct functionalized regions) that would be revealed in response to different liquids, but would remain invisible when dry or when immersed in the wrong decoding liquid. Fig. 4 (Chapter 1) shows a simple example where four different messages are encoded. The ability to layer encrypted messages provides a substantial increase in complexity (making forgery much more difficult with each additional encryption), while minimally increasing the cost (the same protocol can be repeated over and over to make new messages). The primary disadvantage of this technology compared to other possible encryption devices is that it requires liquids for decoding. For applications such as bank note authentication, it seems unlikely that tellers will want to replace the current dry techniques (e.g. blacklight illumination) in favor of an approach that constantly requires getting the bank notes wet.

As mentioned in the previous section, one authentication application where the advantages of W-Ink/WICK versus other technologies may outweigh the disadvantages is in the authentication of liquid formulations (e.g. liquid pharmaceutical formulations, high-end alcoholic beverages etc.). Here the liquid product could itself act as the decoding liquid. An appropriately functionalized strip included in the packaging (e.g. as a sticker) would add two layers of security to the product: 1) the standard anti-forgery protection for the packaging (analogous to the watermark on some bank notes), and 2) anti-forgery protection against the liquid contents themselves, if the response was sufficiently selective to produce a different "failure" message if any changes were made to the formulation that influenced the liquid's wetting properties.

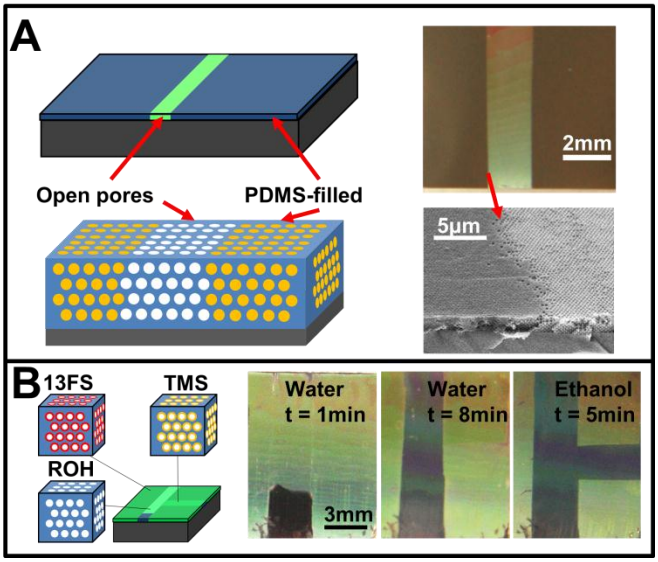

Figure 24. Integrated porous, chemically functionalized fluidic channels. (A) "Visible" microporous fluidic channel defined by selective PDMS-filling in the channel walls. Optical and SEM images of a "visible" porous microfluidic channel, showing the PDMS-filled (dark) regions of the channel walls and the unfilled (bright) regions of the porous channel. (B): "Invisible" microporous fluidic channels defined by contrasting solvent compatibility. The entire system has open porosity. Vertical (ROH) and horizontal (TMS) channels were patterned in a 13FS background. The drop of water placed at the end of the ROH channel spreads only through the vertical channel via capillarity. Repeating the experiment with ethanol results in fluid flow into both the vertical and horizontal channels.

Microfluidics (directed wicking)

This wetting-in-color concept can be extended to create a new kind of microfluidic platform that contains porous, chemically functionalized channels. While synthesizing a highly ordered porous medium inside of a prefabricated microfluidic channel is very challenging [74], we can define channels in an initially homogeneous inverse opal in two different ways, denoted here as "visible channels" and "invisible channels". The former are formed by patterning an IOF with 13FS functionality in the channel regions and ROH functionality outside. Submerging the sample in un-cured PDMS prepolymer results in selective infiltration into the ROH regions while the 13FS regions remain clear. After curing, a microfluidic device with a visible porous channel is generated ("visible" due to its bright photonic color in contrast with the dark, PDMS-infiltrated channel walls, see Fig.24A). The 13FS functionality can then be erased by plasma and the channels further functionalized to allow or resist infiltration by different fluids. Invisible channels are defined using 13FS-functionalitzed regions, resisting infiltration by most liquids, as the channel walls. Invisible channels can be both chemically and configurationally re-patterned, through the same erasing-rewriting procedure. Fig. 24B shows an example of invisible channels making a "T" junction. While water travels via capillarity through the vertical ROH channel, ethanol travels both vertically and horizontally across a second channel defined by TMS surface groups, which is completely invisible (uninfiltrated) in the water experiment.

5.3. Planar lithography on porous surfaces (PLOPS)

Top-down nanofabrication based on planar lithography has been the workhorse of modern nanofabrication, enabling the current microelectronics industry as well as the development of a wide range of device architectures for many other types of technology (photonics, microfluidics, etc.). However, while planar lithography allows the designer sculpting of a wide range of materials in 2D, the extension of such capabilities to truly 3D architectures has proved challenging [96]. The ability to tailor the shape of materials in 3D would open the door for many exciting technologies that have already been proposed. Perhaps most notably, the prospect of 3D-photonic crystals (dielectric superlattices with wavelength-scale periodicity) with designer defects has the promise to enable devices that channel the flow of light without losses due to diffraction [16,96-100]. This could,

for example, lead to the development of defect-tolerant ultrahigh-Q optical resonators. Presently, there are very few techniques that allow truly 3D nanofabrication, and those that do exist are presently limited in their applicability. Focused ion-beam milling can be used to mold a wide variety of materials in 3D, however, this technique is both not scalable (very time consuming, cannot be done in parallel), and generally results in material damage due to ion implantation [101]. Direct-laser writing [96] and two-photon lithography [102] can be used to imprint designer 3D patterns in appropriate resist materials (these patterns can be transferred to other materials by infiltration and inversion), however their resolution is inherently limited by diffraction.

Bottom-up techniques based on self-assembly have emerged as a powerful platform for templating structures that are patterned in 3D with feature sizes ranging from a few nanometers to several microns [20-26,87,92,93]. Unlike their top-down counterparts, they allow scalable 3D-patterning of materials, however the variety of patterns that can be made through bottom-up techniques are very limited in comparison to top-down lithography (generally restricted to periodic or polycrystalline patterns with random defects). For example, while self-assembly has enabled the realization of 3D photonic crystals with complete photonic band-gaps [103], the incorporation of designer defects has thus far been very limited [104], preventing the experimental realization of many of the device properties that initially generated excitement about 3D photonic crystals [16].

In this section we develop techniques to build 3D-periodic nanostructures that contain lithographically patterned planar defect layers. Recent proposals [97-99] have shown that many of the attractive properties of 3D photonic crystal circuits (such as diffractionless control of light flow) can also be accomplished in hybrid 3D-2D-3D structures, consisting of 2D photonic crystals with designer defects sandwiched between two uniform 3D photonic crystals. We developed two techniques to incorporate lithographically patterned planar layers on-top of or inside of self-assembled 3D porous inverse-opal films.

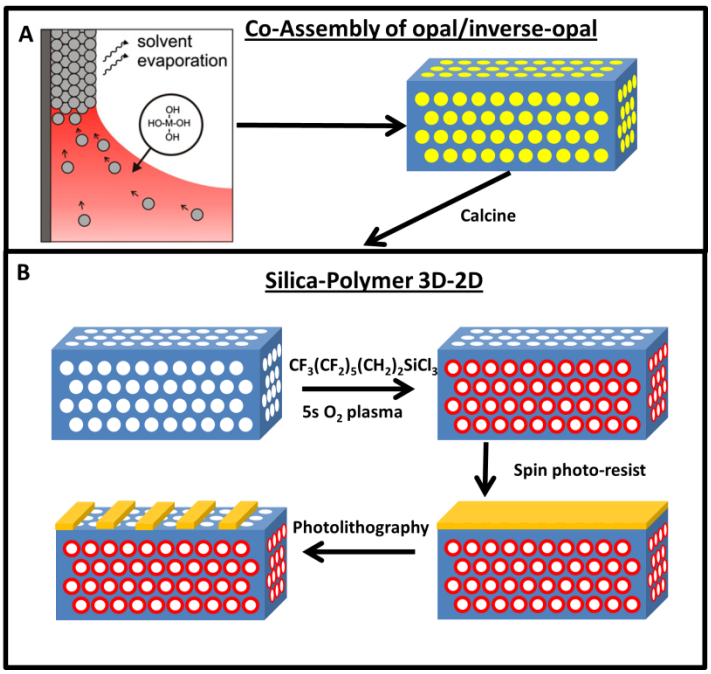

Figure 25. PLOPS-1, exploitation of selective wetting to facilitate the fabrication of 2D-planar structures on top of a porous IOF. After standard IOF fabrication (A), the porous network is functionalized with 13FS to facilitate prevention of solvent and resist infiltration. 5s of oxygen plasma is applied to make the top-surface sufficiently adhesive for the resist, while preserving the 13FS functionality further down the structure. Photoresist (or electron-beam resist) can then be spun and patterned using standard lithographic techniques.

PLOPS-1: Selective wetting as a means to separate planar and porous films

We used the chemical patterning techniques developed in Chapters 1,3 to exploit selective wetting to direct the deposition of resist on the top of the IOFs without penetrating the porous structure. The fabrication protocol is shown in Fig. 25. IOFs are functionalized first with 13FS groups. These groups provide the structure with the ability to resist infiltration of nearly any liquid, including the precursors and solvents for most resists. We then exposed to the surface to oxygen plasma for a very short time (5s), much shorter than would be used even to form a vertical gradient of wettability in the structure. The purpose of this step is to activate the top surface just enough for sufficient adhesion of the resist to occur, while not enough to let the resist penetrate beyond the first row of necks. Finally the resist can be spun and patterned. Fig. 26A shows a cross-section of an IOF with a film of SU-8 photoresist spun on top of it. The SU-8 resist was deposited from a 1-methoxy-2-propyl-

acetate (PGMEA) solution. While delamination was not observed, even during cleaving, indicating some adhesion between the film and the substrate, penetration of the SU-8 is not observed beyond the top layer of half-pores. In particular, no resist is observed beyond the top row of necks. Fig. 26B,C show a patterned film of ZEP520 resist (Zeon corp., patterned by direct electron-beam lithography) suspended on top of an IOF. The resist was deposited from an anisole solution. Again, adhesion of the resist to the film was observed, but no infiltration of the pores beyond the top row of necks.

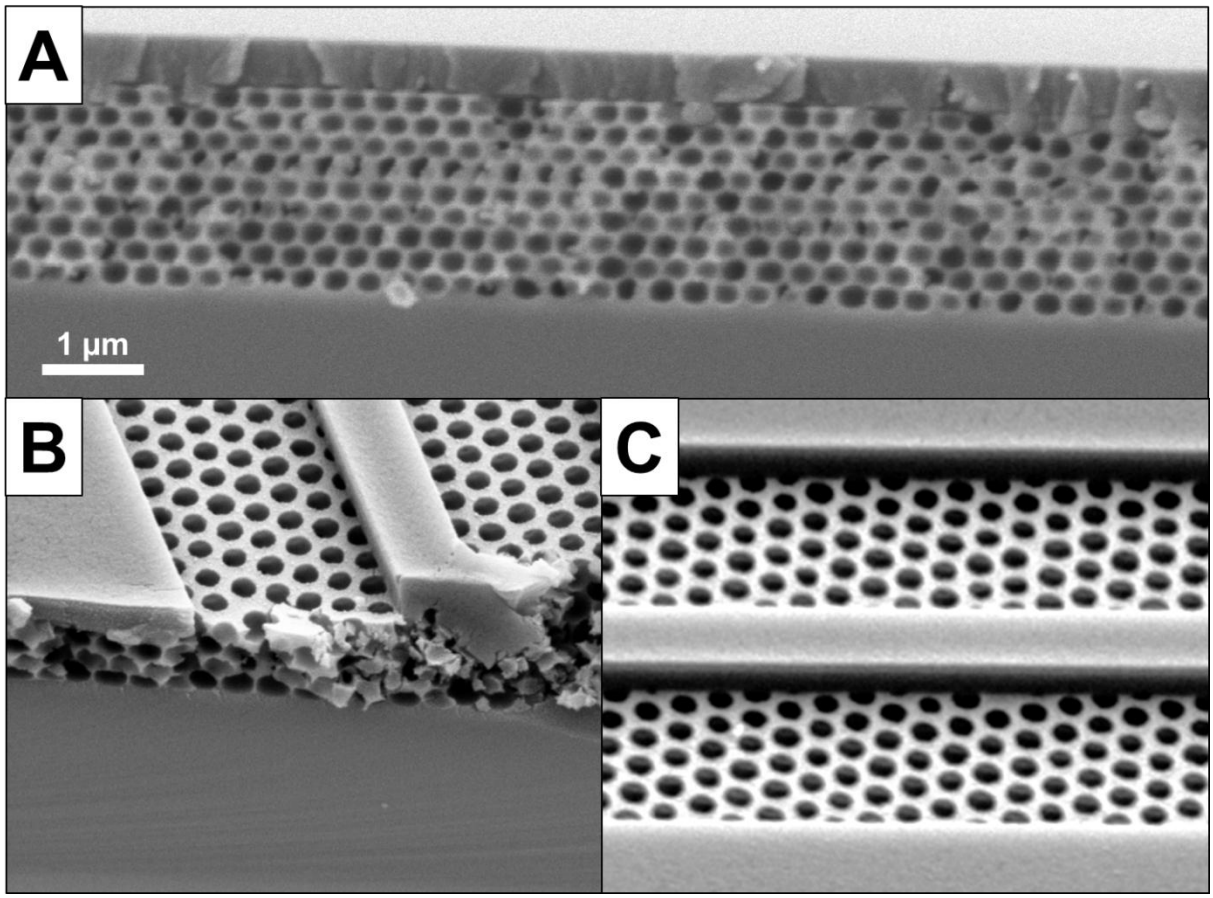

Figure 26. PLOPS-1, SEM images. (A) Cross-section showing a planar SU-8 film deposited on top of an IOF. The SU-8 does not penetrate the pores beyond the top layer of half-spheres. (B,C) SEM images of a film of ZEP520 resist, patterned by electron-beam lithography, suspended on top of an IOF.

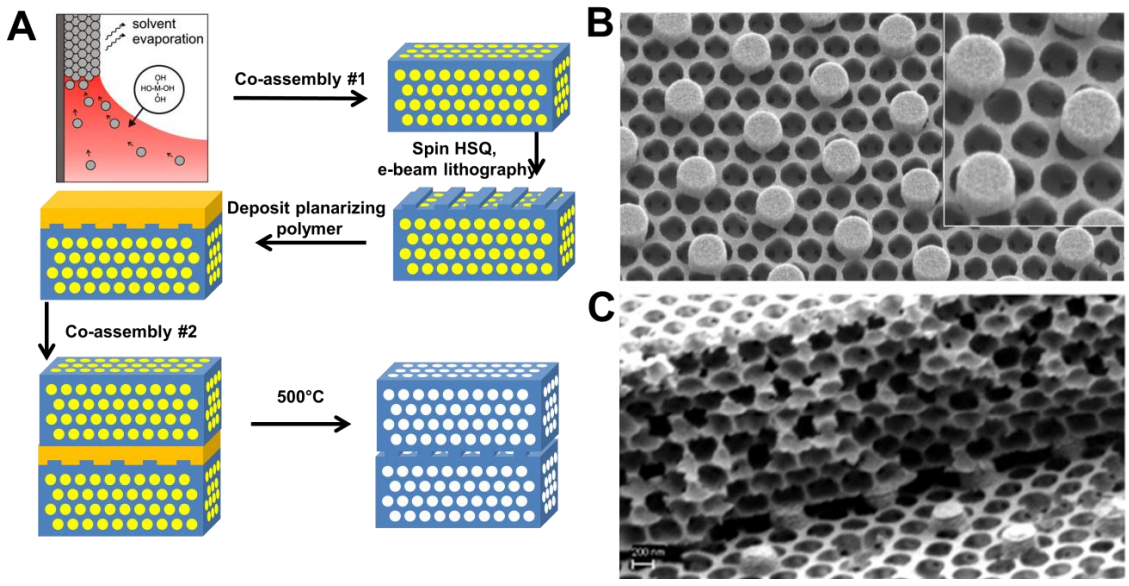

Figure 27 – PLOPS-2: (A) Schematic showing the PLOPS-2 route to stacking of IOF and 2D-patterned planar layers. Co-assembly of the polymer colloidal crystal template and the silica interstitial matrix is performed [59], but the polymer spheres are not immediately removed, resulting in a solid, non-porous film (plugged IOF). A spin-on-glass electron-beam resist (hydrogen silsesquioxane, HSQ) is deposited on top of the plugged IOF and patterned by electron-beam lithography. A thick polymer film is then spun on top of the 2-D patterned layer to planarize. Following the activation of the planarizing film surface, a second co-assembly step is done to deposit a second plugged IOF. Finally all polymer components are removed by a slow calcination procedure (ramp up to 500°C over 5hr), leaving behind a stack consisting of a 2D-patterned planar layer wedged between two IOFs. (B,C) SEM images 3D-2D and 3D-2D-3D stacks prepared by the PLOPS-2 method. (B) A 3D-2D structure is formed by removing the polymer template right after the electron-beam lithography. An array of 500nm wide posts are shown suspended on top of an IOF with a ~300nm pore diameter. (C) A cross-section of a 3D-2D-3D structure showing adhesion between the layers. The same array of 500nm wide posts is used in this structures.

PLOPS-2: 3D-2D-3D silica stacks from plugged IOFs and planarized 2D layers

While possessing the highly selective wetting properties that enable the PLOPS-1 technique, IOFs fabricated by co-assembly also benefit from the advantage of having very flat top surfaces after deposition [59]. Before removal of the polymer template (a state I refer to as a plugged IOF), plugged IOFs are completely flat and solid films of material [59]. Owing to the flatness and lack of porosity in plugged IOFs, 2D patterned-resist

layers can be easily deposited before removal of the polymer spheres. However, this order of fabrication steps requires the use of a resist that can withstand the conditions used to remove the polymer spheres (this rules out many organic polymer-based resists). We used spin-on-glass (hydrogen silsesquioxane, HSQ) as a resist for this demonstration since upon curing it becomes chemically similar to the sol-gel silica material that makes up the IOF. The resist was patterned by electron-beam lithography. When the structure was calcined after this e-beam patterning, a 3D-2D hybrid structure similar to the type formed in PLOPS-1 is left behind.

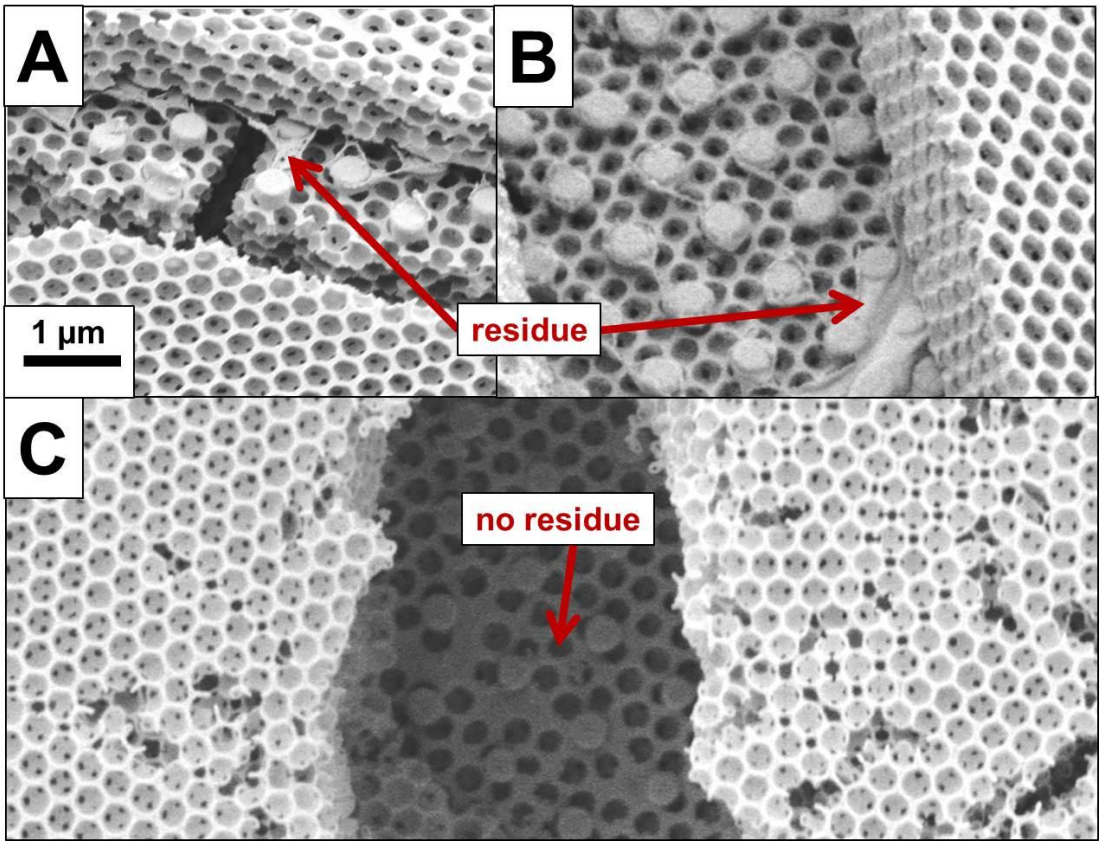

Figure 28. Planarizing layer residue: (A,B) While SU-8 served as a planarizing layer that remained hydrophilic after activation for a sufficiently long time to allow deposition of IOFs, it had the tendency to leave behind residue after calcination. (C) PMMA (the same material used in the polymer sphere template) was found not to remain activated long enough for film deposition, however if a thin layer of silica was vapor-deposited on the PMMA film immediately after activation [105], the surface remained hydrophilic for sufficient time for growth of the second IOF. After calcination, this protocol left behind fewer residues and also seemed to enhance adhesion between the layers.

However, if the IOF remains plugged, a second IOF can be grown on top of the patterned HSQ layer, sandwiching this lithographically 2D-patterned layer between two 3D-periodic structures, producing the type of 3D-2D-3D architecture proposed in Refs. [97,98]. Successful deposition of the second IOF requires first planarizing the patterned 2D HSQ layer. This can be done by spin-coating a thick film on top of the HSQ pattern. We deposited a planarizing film with ~5μm thickness for a ~250nm thick resist layer. In order for the second IOF to grow successfully, the surface of this planarizing layer must be able to be rendered very hydrophilic (zero-degree contact angle) for a long time. We found that while the hydrophilicity of many common polymers did not last for sufficiently long times after oxygen-plasma activation for a successful deposition of a second IOF (we tried polymethyl methacrylate, polystyrene, and polypyrrole), SU-8 (flood exposed with UV-light to cure) did retain long-lived hydrophilicity after oxygen-plasma exposure and successful growth of IOFs was possible on these films. After deposition of the second plugged IOF, the entire structure was calcined to remove the polymer spheres and the planarizing polymer. To facilitate gentle removal of the planarizing polymer, allowing for the top layer IOF to fall on top of the lower layers without large amounts of cracking, the temperature was ramped up to 500°C over five hours. Before deposition of the second IOF, the planarizing layer could also have been thinned down using reactive-ion etching, however this process, if not strictly necessary, would add significant complexity to the otherwise simple fabrication procedure. Fig. 27C shows a cleaved section of a 3D-2D-3D stack formed using an SU-8 planarization layer. As evident from the cross section, the top layer IOF manages to rest flush against the surface of the 2D layer after calcining.

Although SU-8 was found to be a polymer planarizing layer that could remain activated for sufficiently long times to allow for successful deposition of the top layer IOF, it was also found to leave behind a significant amount of residue after calcining. Fig. 28A,B show examples of this residue. Due to the highly aromatic structure of SU-8, the appearance of significant amounts of carbonaceous remnants after pyrolysis is not unexpected. To limit the appearance of residue, we searched for an alternative to SU-8 for the planarizing layer. Based on the absence of residue observed after calcination of a standard IOF (one 3D layer only), PMMA (the same material used in the spheres) would be expected to leave no residue behind as a planarizing layer, however we were unable

to grow IOFs successfully on plasma-oxidized PMMA films, since their hydrophilicity degrades over time. To enhance the lifetime of a PMMA film's hydrophilicity, we performed a sol-gel vapor-deposition immediately after activation of the surface that can deposit a very thin layer of silica (~5-10nm) [105]. This protocol, developed by Hatton et al [105] (colloquially referred to as the 'poor man's ALD') consists of two steps, both performed under ambient pressure and humidity in air: 1) the activated film was suspended in a closed test tube for 1 minute, with a small amount of the silica precursor, tetramethyl orthosilicate (TMOS), at the bottom. This step facilitated the chemisorption of a small amount of TMOS vapor on the surface. 2) The second step consisted of reactivating the TMOS-covered surface through base-catalyzed hydrolysis by exposure to a saturated atmosphere of ammonium hydroxide (this exposure was done for 10 minutes). This cycle can be repeated many times to control the thickness of the film, with ~5nm deposited per cycle [105]. We found that two cycles of deposition provided a significantly long-lived, uniform activated surface, sufficient to allow the successful growth of IOFs on PMMA films. Fig. 28C shows a 3D-2D-3D stack fabricated using a PMMA planarizing layer that was activated using two 'poor man's ALD' deposition cycles. This protocol eliminated the residue that was observed with SU-8 as a planarizing layer.

In this section, we have demonstrated two techniques to integrate 2D-lithographically-patterned planar layers on top of or in between 3D-periodic inverse-opal films. Both of these techniques are enabled by the uniform, crack-free and flat-surfaced nature of these films when grown by colloidal co-assembly [59]. Using simple chemical surface-modifications and the unique wetting properties of the IOFs (these properties are characterized in Chapters 2 & 3), we have shown that we are able to spin-coat and pattern resist layers on top of IOFs that show good adhesion to the top of the porous surface, but no penetration inside of the pores. These fabrication procedures, combining advantages of both top-down and bottom-up fabrication, may prove useful in the development of 3D-2D photonic crystal devices [97-99].

Chapter 6. Conclusions and Outlook

6.1. Conclusions

This thesis has provided a detailed description of the development of Wetting In Color technology, exploring the principles behind and the applications of the highly spatially selective infiltration of liquids in defect-free inverse-opal films (IOFs) grown by colloidal co-assembly. At a fundamental level, there are two significant advances developed here. The first is the discovery and characterization of the highly selective nature of wetting in IOFs and its natural coupling to an easy-to-detect optical response, owing to the vast difference in refractive-index contrast between air-filled and fluid-filled films. Using a combination of percolation modeling and optical modeling to corroborate our experimental observations, it has been shown that fluids differing by only ~3° of intrinsic contact angle to the pore surfaces can induce macroscopically distinct structural color responses (with uniform pore surface chemistry). The second major advance described here is the development of techniques, based only on chlorosilane chemistry and oxygen plasma, enabling us to define highly controlled 3D spatial patterns of wettability within the porous network.

While many potential applications of this platform have been briefly introduced here (multilevel encryption, fluidics, nanofabrication), the primary focus of this thesis has been in sensing, the development of a Wetting In Color Kit (WICK), a colorimetric indicator for simple and at-home identification of organic liquids based on their wetting properties. With this application in mind, we have performed optimizations of the Wetting In Color platform with respect to several performance metrics. Broadly speaking, we can list the most important of these metrics as follows (in order of decreasing importance): 1) Ease-of-use and cost; 2) Versatility and adjustability (to how many sensing problems can we tailor this technology to); 3) Selectivity (how small a change in wettability can we detect?); 4) Chemical specificity; and 5) Reproducibility (how robust is our technology to variability in fabrication and what kinds of quality control can we implement?).

The progress made on each of these fronts is as follows: 1) Ease-of-use and cost are paramount to all other performance metrics because they are what enables WICK to be used at home or in the field by users with minimal training and/or access to resources. The fact that WICK gives instant colorimetric readouts is an advantage that essentially comes for free. However, to ensure that WICKs can be read and interpreted easily without sensitivity to lighting conditions and viewing angle (a general drawback of sensors based on structural color), we have ensured that all of our readouts are based on *countable* changes in color (e.g. binary readout). Complete determination of our response can be done based on analyzing *where* on the WICK iridescent color can be observed, without a need to identify *what* color is shown.

2) An attractive property of WICK is that its colorimetric response is sensitive to wettability, a generic property of liquids that makes this approach suitable, in-principle to any sensing paradigm involving liquids. However, the threshold wettability of an IOF only occurs at one value ($\theta_c \sim 20°$), meaning that a region with a fixed surface chemistry only produces two distinct countable responses to liquids that are either above or below this threshold. The techniques we developed to control and spatially pattern the surface chemistry is what has allowed us to tailor many responses to many different liquids, all within a single WICK.

3) The high selectivity of this indicator is a result of the unique, highly-regular geometry of our IOFs, which we have characterized in detail here. However, it was shown in Chapter 3 that we can actually further increase the selectivity of the response by vertically grading the wettability. This does so, not by shrinking the range of liquids that produce partially filled responses (in fact it does the opposite), but by making closely related partial filling profiles produce countable differences in the color pattern.

4) As the response of WICK is based on wettability, a generic, non-specific property of liquids, identifying unknown liquids with chemical specificity (i.e. requiring minimal prior knowledge of the possible composition) is the greatest challenge in the development of WICK. In Chapter 4, we have shown here that the chemical specificity can be improved by comparing combinations of wetting responses in an array of WICKs, each of which is designed to exhibit non-trivial colorimetric responses to the same range of liquids, but using different chemical surface groups to define the wetting gradient. Further improvement of the specificity can be

attained by observing the time it takes for the film to dry after having observed the wetting responses to a WICK or a WICK array.

5) In Chapter 3, we showed how the sample-sample variability in the pore geometry can be limited based on post-selection using wetting in liquid standards and a control surface functionality. In Chapter 4, it was shown that the use of combinatorial measurements based on WICK arrays gave the sensing platform an added robustness against variability in the response.

6.2. Suggestions for future studies

There are many scientific advances and potential applications of Wetting In Color technology that have been mentioned in the preceding chapters of this thesis, particularly relating to sensing, but also in encryption, fluidics and nanofabrication. However there are also a number of promising opportunities for this technology that are yet to be looked-at. In this section, concluding this thesis, I will outline several future studies relating to this work that I think are promising.

Enantioselective Colorimetry

Related to sensing, I think there are a few exciting avenues that could be explored in the future. One notable example is the application of WICK for enantiospecific colorimetric identification of chiral compounds. While enantiospecific surface interactions between a chiral liquid (or solute) and a chiral surface group are well documented and have been long exploited for applications such as chiral chromatography, it is only recently that enantiospecificity has been observed directly in wetting (measured as differences in contact-angle) [106]. The sensitivity of the WICK platform to changes in intrinsic contact angle may be sufficient in some cases to observe a large color difference between different enantiomers of the same structure. With even higher contrast, it may even be possible to design a WICK that can colorimetrically estimate the degree of racemization of a mixture of enantiomers. In addition to attaining sufficient sensitivity to observe this effect in WICK, a primary challenge likely to be faced in this implementation would be tuning of the IOF's wettability threshold precisely to the difference between enantiomers, while simultaneously preserving the type of surface chemistry that facilitates

enantiospecificity. In this case, it might prove easier to tune the liquid composition (e.g. by dilution with a known liquid) or even the pore geometry (e.g. by conformally thickening the walls [105]).

Enhanced Selectivity with Liquid-Liquid WICK

Another interesting future direction that may be worth exploring is the use of a liquid background medium (replacing air) in WICK measurements, with the potential to greatly enhance the sensitivity of the wetting threshold to the chemical composition of the liquid. With a structure whose response is sensitive to differences in intrinsic contact angle [$\cos(\theta_c) = (\gamma_{sa} - \gamma_{sl})/\gamma_{la}$], the sensitivity to chemical differences is proportionally reduced with increasing liquid-air surface tension. Conversely, replacing the liquid-air-interface with a liquid-liquid interface would greatly reduce γ_{la} (this can be by an order of magnitude [106]), resulting in a large increase in the wetting selectivity. Two large challenges with this approach, however, would be finding a suitable background fluid/surface-chemistry combination (this would have to be both immiscible with the test liquid, and exhibit a solid-liquid-liquid contact angle in the range of the threshold wettability), and coupling this sensitivity to an easy-to-detect optical response. The latter would be difficult because there may be a minimal or even absent change in refractive-index contrast associated with the displacement of one liquid by another. This could be mitigated perhaps by adding a chromophore to either the test liquid or the background liquid. Alternatively, building on recent work by Wong et al. [107], the displacement could be monitored by observing whether or not a stable drop of the test liquid can rest on (and easily rolled off of) a thin film of the background liquid, held in place by an IOF, without displacing it in the pores.

Dynamic Wetting

With the exception of some very primitive examples of dynamic wetting behavior discussed at the very end of Chapter 4, this work has largely been restricted in scope to the study of static pore-filling states. The high sensitivity of the colorimetric wetting response near the threshold wettability could potentially also be used to induce changes in the filling behavior in response to subtle dynamic changes in either the liquid or the pore surface chemistry. At the end of Chapter 4, a very simple example of this type of behavior was shown, consisting of a liquid mixture whose wettability increased over time as the more volatile component evaporated. However,

much more interesting would be if a macroscopic wetting response could be induced to track *chemical* changes in a system, either in the liquid or on the surface. One potential application of this type of a system would be in monitoring stages of chemical reactions colorimetrically where no current indicator material exists. This could be taken further if the IOF in the non-wetted state was used as a physical barrier to sequester reagents until broken by a chemical change. One could envision the design of an integrated multi-step microfluidic reaction vessel based on this type of architecture, where the progress of one step of a reaction triggered wetting of an IOF barrier, which, in turn, released new reagents to induce the next step of the reaction.

Application to Other Porous Materials

The methods developed in Chapters 1-3 for generating controlled spatial pattern of surface chemistry should be applicable to many different types of porous materials, their use potentially enabling many applications when implemented in different types of porous structures (periodic mesoporous materials for example [92,93]). The spatial selectivity of patterning in both the vertical and lateral dimensions is possible because oxygen plasma modification fronts are found to move very slowly when the reactive species must move through highly confined porous geometries. This allows the timing of plasma exposure and the location of the inlets (unmasked regions of top-surface in our case) to be tuned to let the oxidation to reach only specific regions of the pore structure. This property of oxygen-plasma modification is not unique to our pore geometry and seems to be quite generalizable.

For example, Lin et al [61] showed slow-moving oxidation fronts when the plasma was confined to move in a maze of micron-scale channels. Comparing our results to theirs, we expect the general trend that the front propagation speed positively correlates with the size of the pores. This suggests that spatial control of surface chemistry should work best in structures that have a highly regular pore-geometry. Very recently, we have shown that shadow-masked plasma oxidation can be used to pattern wettability in periodic mesoporous organosilicas [108]. Mesoporous materials, having vastly sub-wavelength porosity and very high surface area are useful for gas sensing because macroscopic changes in refractive index can be coupled to small amounts of vapor adsorption [35]. Incorporating spatial patterns of many different surface groups in these materials would potentially enable a versatile platform for combinatorial gas sensing, analogous to WICK arrays for liquid identification.

Appendix A. Detailed Experimental Techniques

The primary purpose of this Appendix is to provide sufficiently detailed accounts of our experimental procedures to make it easy for a future student or postdoctoral fellow who is new to the lab to be able to repeat any of these experiments to continue this work. Therefore, while some of these procedures are outlined in previous literature (e.g. ref [59]), the variants of these procedures that we used for these studies are described here in detail as well. As a second note, since the work described here was conducted over a long time-span (several years), some of the protocols underwent small modifications during the process. For this reason, after describing the general preparation of IOFs, methods will be generally divided by Chapter, with small chronological modifications of the procedures from one chapter to the next pointed out.

A.1. Fabrication of defect-free inverse opals

Synthesizing colloids

Monodisperse aqueous suspensions of polymethylmethacrylate (PMMA) microspheres (d ~ 300nm) were synthesized according to the following procedure:

A bath of silicon oil was prepared and heated to 80^{o}C on a hot plate (the temperature is measured with a thermocouple immersed in the silicone oil). The bath was stirred by a magnetic stirrer at 400 RPM. A clean 500 mL 3-neck round-bottom flask was added to the bath connected to a condenser on the leftmost hole, as shown in the figure. 90 mL of DI water was added to the round bottom flask. 0.2 g of ammonium persulfate (APS, the free-radical initiator) was added to the middle hole of the flask. A large football-shaped stir bar was added to the mixture and let stir at 400 RPM for at least 1 hour. In a separate vial, 10.5 mL of methyl methacrylate (MMA), 0.0948 mL of ethylene glycol dimethacrylate, and 0.0473 mL of 1-dodecanethiol were combined. The mixture was sonicated for 5 minutes. After an hour of stirring the APS and water, a 12 mL syringe (with large needle) was used to inject the MMA mixture into the flask as fast as possible without creating too many bubbles. It was

ensured that the metal tip of the needle does not touch the contents of the flask. The total mixture was left to stir at 400 RPM for at least 3 hours (5-6 hours is ideal before removing from heat). If executed correctly, at this time, the contents of the flask appeared white, and opaque. As a quick test of the monodispersity of the suspension before cleaning, a small drop was left to dry on a glass slide and iridescence of the residue was verified.

Before the colloidal suspension can be used to make good quality inverse opals, it has to be cleaned to remove any residual monomer and other unreacted reagents from the previous step. This was done via dialysis. The suspension was decanted into a dialysis bag. After sealing the bag, it was placed into a large (2L) beaker filled with DI water with a large clean stir bar. The bag was left in the water, gently stirring for at least 7 days. The water was replaced every 24hr. After 7 days, a small amount of the suspension was tested each day (while the remainder of the suspension remained in dialysis) by depositing an opal (no silica) on a clean, oxidized silicon wafer. The observation of uneven 'banded' growth (vertically alternating regions of many layers and regions with no growth), was used as an indicator that the dialysis cleaning needed to take place for longer. Consistent growth of good quality films was used as the indicator that the suspension was clean.

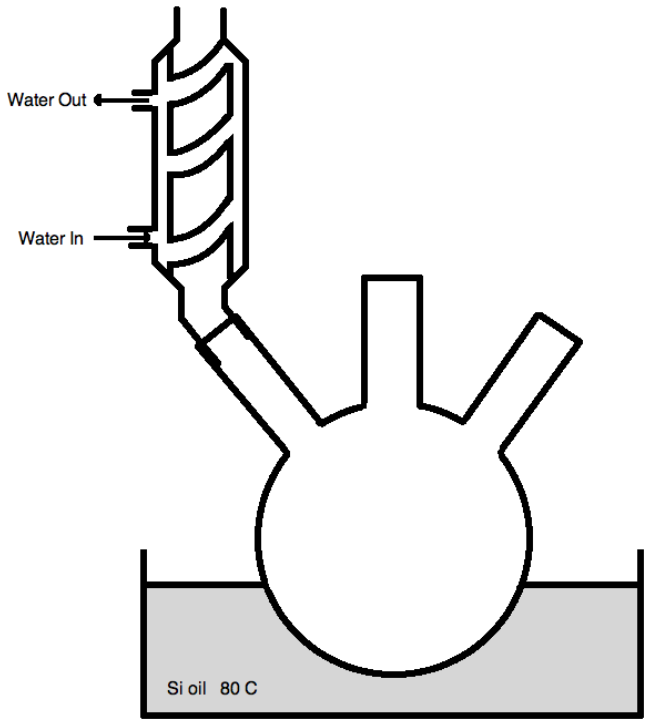

Figure A1 – Diagram of the three-neck flask and attached condenser used in the colloid synthesis.

Preparing TEOS solution

A solution of 0.01M HCl was periodically prepared by diluting an aliquot of a 1M stock solution. The pH of the solution should be checked periodically (every 2-3 weeks, pH paper is sufficient) before use. 5.00g of the 0.01M HCl solution, 7.50g of ethanol and 5.00g of tetraethyl orthosilicate (TEOS, also called tetraethoxysilane, $Si(OCH_2CH_3)_4$, Sigma-Aldrich) were added to a clean, unused 20mL vial (in the above order) along with a small clean magnetic stir bar. The TEOS solution was left to stir at 300rpm for 1hr in order for the TEOS to hydrolize. If control of inverse opal film thickness is desired, a TEOS solution should only be used the same day it was made.

Preparing and Cleaning Substrates

Fresh silicon wafers were cut it into ~5cm x 1cm strips using a diamond scribe, by cleaving along crystal planes. After air-blowing to blow away any loose shards, substrates were cleaned in acid-piranha solution (3:1 concentrated sulfuric acid, 30% hydrogen peroxide) at 90°C for 5-10 mintues, followed by rinsing with DI water and then ethanol. Clean substrates were stored in a clean (unused) glass jar filled with ethanol.

Depositing the Film:

Clean, unused 20.5mL vials were filled with 20 mL of DI water. After briefly sonicating the stock colloidal suspension to ensure that nothing has settled (about 2 min), an aliquot of the stock suspension was added to the vial (typically 0.1-0.5mL of suspension, optimized by concentration measurements and trial & error, depending on the desired film thickness). Fig. A2 is a guide to this optimization.

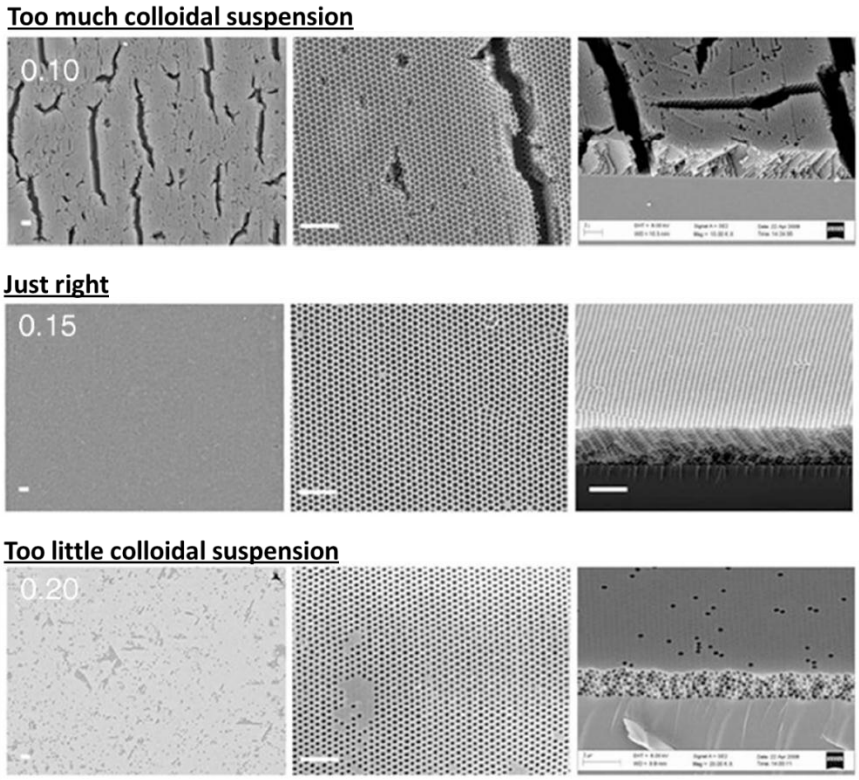

Figure A2 – Scanning electron micrographs (SEM) of IOFs grown using different ratios of colloidal suspension and TEOS solution, showing the crack-free IOFs formed when the ratio is correct (middle) when there is not enough TEOS (or too much colloidal suspension, top) and when there is too much TEOS solution (or not enough colloidal suspension, bottom) [59].

Next 0.095-1.5mL of TEOS solution was added to the vial (again, the exact amount was optimized for each new stock solution of colloids, for the desired thickness of film and film quality). This mixture was then sonicated for 1-2 min to ensure adequate mixing. A previously piranha-cleaned Si substrate was removed from the ethanol bath, blow dried and oxygen plasma-cleaned for 3min with ~10sccm of oxygen flow (Diener Electric GmbH Femto-A plasma cleaner). The cleaned substrate was suspended vertically in the vial containing the water-colloid suspension-TEOS solution (held using binder clips) and placed in an oven held at 65°C on a vibration-free table. To ensure that the relative humidity in the oven was kept roughly constant (which can affect the evaporation rate, and thus the thickness and quality of the films) the same number of vials, with suspended substrates, were placed in the oven simultaneously in all depositions (the optimization of concentration can be

done for any number in principle, as long as the same number is always used, which for us was six). The oven was left closed until the liquid had completely evaporated from the vial, leaving behind a film on the substrate. It is worth noting that opening and closing the oven during the deposition left large defect lines across the film at the height of the meniscus at the time the oven was opened (caused presumably by the resulting changes in humidity). Vibrations could cause the same effect. After removing the dry substrates from the oven, they were placed, polished-side-up in a tube furnace (connected to the air) to remove the polymer template. The temperature of the furnace was ramped up to 500°C over 5hrs, held at that temperature for 2hrs, and then ramped down to room temperature over 1 hr. After deposition and removal of the polymer spheres, samples were placed for 4 hours in a bath of acid piranha (3:1 concentrated sulfuric acid: 30% hydrogen peroxide) held at 90°C on a hot plate. After rinsing and drying, they were oxygen-plasma-cleaned for 1hr (100W, 5-10 sccm). As a final step, the IOFs were submerged in a dish filled with clean DI water overnight (for dialysis cleaning).

A.2. Spatially patterning the surface chemistry for encryption (Chapter 1)

The IOFs were exposed to vapors of 1H,1H,2H,2H-tridecafluorooctyl)trichlorosilane (13FS, Gelest, Inc.) in a vacuum chamber for 24h, followed by a 10 min bake at 150°C. Polydimethylsiloxane (PDMS) masks (2-5mm-thick) were prepared by pouring a 10:1 (wt) mixture of PDMS resin and cross-linking agent (Sylgard 184, Dow Corning) into a clean, empty tissue culture dish and curing for 3-5h at 70°C. Patterns were carved in freshly cured slabs using pre-shaped blades (e.g. cookie-cutter) or with a scalpel or razor-blade, and masks were discarded after one use. For IOFs containing *m* complex patterns (e.g. letters) with *n* different functionalities on an ROH background, the surface chemistries were first defined in a simple stripe pattern, where *m* large stripes to contain the final patterns of a given functionality were used. This allowed us to clamp large PDMS masks directly to the sample (with no overhanging cover slip) and ensuring that exposure to the oxygen plasma was the same for all mask heights and shapes. The mask could be peeled off after the exposure without damaging the structure. In each iteration of the patterning, the sample, with a PDMS mask clamped directly over the desired region is exposed to oxygen plasma (Diener Electric GmbH Femto-A plasma cleaner, O_2 flow rate 5-10sccm) for 3-10min.

In the second step, the mask was removed and the sample was exposed to vapors of a different alkylchlorosilane, either n-decyltrichlorosilane (DEC, Gelest, Inc.), 3,3,3-trifluoropropyltrichlorosilane (3FS, Alfa Aesar) (each for 24h) or chlorotrimethylsilane (TMS, Alfa Aesar) (20 min). Exposure was done under vacuum for all alkylchlorosilane depositions except for highly volatile TMS, which was done at 1atm. All exposures were followed by a 10 min bake at 150°C. In all experiments, we applied our functionalities in order of increasing wettability (13FS→DEC→3FS→TMS). After large regions containing each surface chemistry in the desired final pattern have been defined, the background was re-activated by one final exposure to oxygen plasma, masked by the desired final pattern. To ensure good contact and a well-defined pattern, the PDMS masks (e.g. letters) were held under uniform pressure from a glass cover-slip. The sample was exposed in this state to oxygen plasma for 10-30min (5-10sccm, long times used for thicker films) to impart ROH functionality on the background.

A.3. Imaging of wetting interfaces

PDMS-filling:

For interface characterization, an IOF with regions of 13FS and ROH surface groups was fabricated as described above. 10:1 PDMS resin:cross-linker (Sylgard 184, Dow Corning) was poured over the sample until it was submerged. Penetration into the ROH pores was accelerated by placing IOF immersed in PDMS precursors under vacuum for 2-3h before curing for 2-5h at 70C. The vacuum step also served to remove any trapped bubbles. After curing, the PDMS overlayer was peeled off manually and was found to break naturally at the top-surface of the IOF in infiltrated regions.

Interfaces were characterized by optical and scanning electron microscopy (JEOL, Zeiss) as well as via scanning optical spectroscopy. Figure A3 shows optical micrographs, spectral scans and SEM images of an interface visualized by selective infiltration of PDMS into the IOF. All measurements show the presence of a partially-filled transition region, whose width varied from ~5-20μm, separating the completely filled region and the completely unfilled region. To characterize the interface of the functionalized regions, an IOF was first derivatized uniformly with (1H,1H,2H,2H-perfluorooctyl)silyl (R = 13FS) groups and then etched through a rectangular mask to reveal hydrophilic polar surfaces (referred to altogether as ROH hereafter for simplicity).

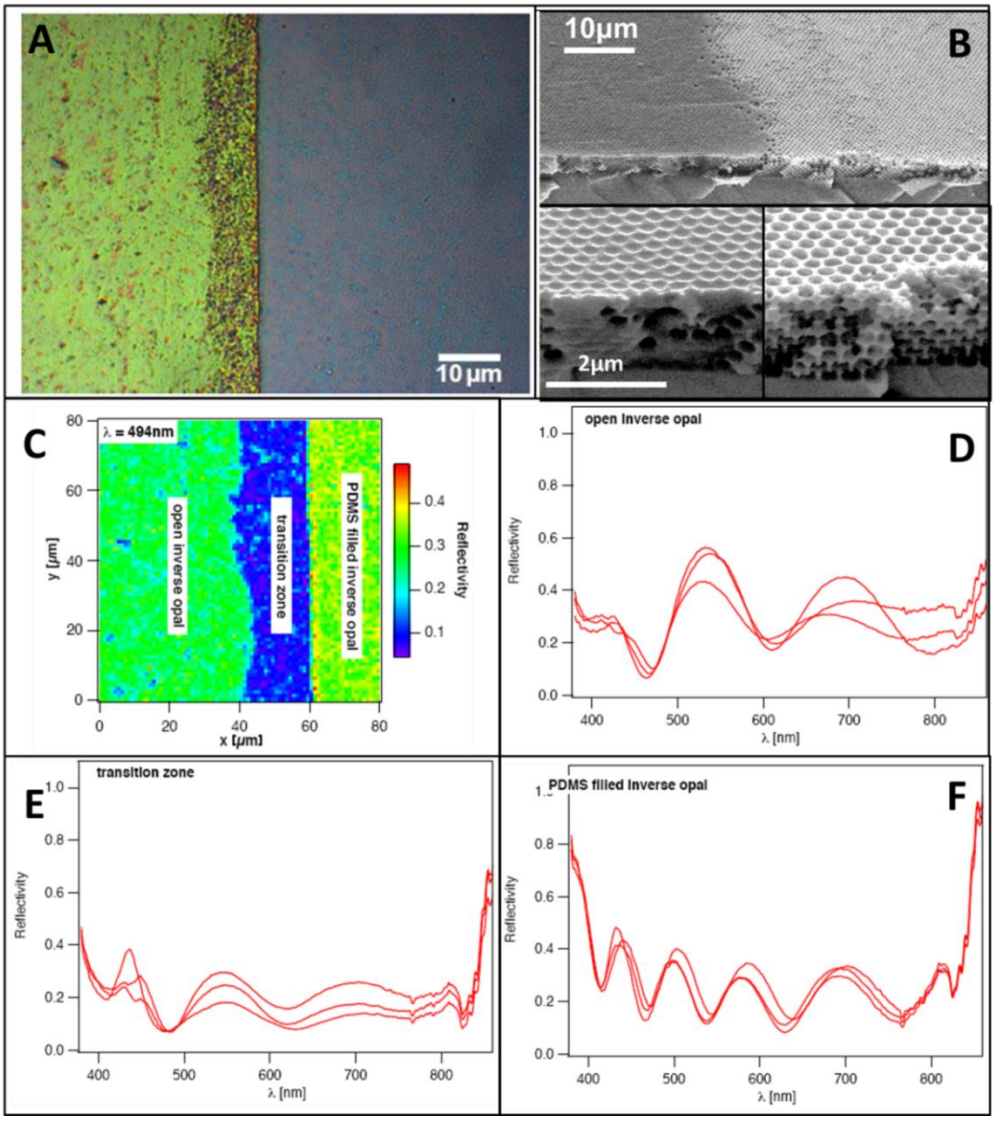

Figure A3. Optical characterization of a wetting interface visualized by the selective infiltration of PDMS into ROH-functionalized regions. Regions functionalized by 13FS were not infiltrated upon immersion in PDMS prepolymer. **A**: Optical micrograph of the interface with complete infiltration on the right. **B**: Cross-sectional SEM image of an interface corner, showing the boundary between regions filled with PDMS (ROH) and remaining empty (13FS) **C**: Scanning optical spectroscopy image at 494nm, clearly showing three distinct regions – the completely filled region, the partially filled transition region, and the completely empty region. **D-F**: A few representative spectra taken from points in each of the three regions showing the transition from a more pronounced reflection peak at ~530 nm in the non-infiltrated regions to a multi-peak thin-film interference pattern in the regions penetrated by PDMS, which is well index-matched with our sol-gel silica.

We found that the pores of the 13FS-functionalized IOF resisted infiltration by most solvents, including liquid precursors of PDMS. Selective infiltration of PDMS prepolymer into the lyophilic (ROH) regions of the crystal followed by thermal curing allowed us to freeze in place and characterize the chemical interface. Using SEM, optical microscopy and optical spectroscopy, we measured wetting interfaces to have widths of 5-20μm (see Fig. A3), which represents the resolution limit of our technique.

A.4. Functionalization procedures for Chapters 2&3

Quality Control

After calcination, and cleaning, IOFs were exposed first to vapors of n-decyl (DEC) trichlorosilane for 24h under vacuum, followed by baking at 150°C for 20 min. To test for viability before use, wetting in the IOFs was first characterized with this DEC functionality in 85% (vol) and 90% ethanol in water. In order to pass this quality control step, an IOF had to display an unfilled state in 85% and a completely filled state in 90% (using the binary definitions described in Chapters 2 & 3). In samples that satisfied these requirements, the uniform DEC functionality was erased via O_2 plasma exposure for 1hour, followed by acid piranha cleaning (4hr, 85°C), followed by a second hour of O_2 plasma exposure.

Deposition of heterogeneous (mixed) functionalities

IOFs were exposed for 24hr to mixed 13FS (1H,1H,2H,2H-tridecafluorooctyl)-, DEC-trichlorosilane vapors by placing them under vacuum in a dessicator with two small vials, each containing 200μL of a 13FS-, DEC-trichlorosilane liquid-liquid mixture and a small dish containing dry dessicant (Drierite ®). The ratios shown in Fig. 10 represent the liquid-liquid ratios in these vials. Following sliane exposure, IOFs were baked at 150°C for 20min.

Vertical Gradients of Wettability

IOFs were exposed under vacuum to vapors of 13FS-trichlorosilane for 24hr. After baking for 20 minutes at 150°C, IOFs were exposed to O_2 plasma (5-10 sccm) for 10-120s. All were then exposed to vapors DEC-trichlorosilane for 24h under vacuum, followed by baking at 150°C for 20 min.

Defining hydrophilic patterns (Guiding the Eye):

To aid in visualization, hydrophilic regions were sometimes defined in IOFs using masked O_2 plasma exposure. Polydimethylsiloxane (PDMS) masks (2-5mm-thick) were prepared by pouring a 10:1 (wt) mixture of PDMS resin and cross-linking agent (Sylgard 184, Dow Corning) into a clean, empty tissue culture dish and curing for 24h at 70C. Patterns were carved in freshly cured slabs with a scalpel or razor-blade, and masks were discarded after one use. The PDMS masks (*e.g.* letters) were held against the IOFs under uniform pressure from a glass cover-slip. The sample was exposed in this state to oxygen plasma for 10-30min (5-10sccm) to render the unmasked regions wetting to all liquids.

A.5. Methods for combinatorial Wetting in Color (Chapter 4)

Applying Vertical Gradients of Wettability.

Since 13FS was used as the base group in all elements of the array, all IOFs were first exposed under vacuum to vapors of 1H,1H,2H,2H-tridecafluoroocytl (13FS) – trichlorosilane for 24hrs. To remove potential sensitivity of the protocol to ambient humidity, IOFs were exposed after silanization to a saturated atmosphere of water vapor (done simply by submerging the hydrophobic porous IOFs in a dish filled with DI water). IOFs were then baked for 20 minutes at 150 °C under atmospheric pressure and ambient humidity. To apply the gradient, IOFs were exposed to O_2 plasma (5-10 sccm, 100W) for 30s. Samples were then functionalized with one of: n-decyl -(DEC), 3-phenylpropyl- (3PP), 3,3,3-trifluoropropyl- (3FS), pentafluorophenylpropyl- (5FP), p-tolyl- (PTOL), or trimethylsilyl (TMS) groups. Functionalization with DEC, 3PP, 3FS, 5FP and PTOL groups were done by exposing the IOF to vapors of the corresponding alkyltrichlorosilane according to the same procedure as described for 13FS. TMS-functionalization was accomplished by exposing the IOF to vapors of

chlorotrimethylsilane under atmospheric pressure and ambient humidity for 20 minutes. After silanization, all samples were post-treated as described for 13FS functionalization. All trichlorosilanes were purchased from Gelest Inc. and used without further purification. Chlorotrimethylsilane was purchased from Alfa Aesar and used without further purification. Finally, before testing, all samples are vigorously rinsed in ethanol, and air dried.

Testing

Each sample is placed in a dish of desired liquid and its colorimetric wetting response photographed. Initially samples were photographed in ethanol-water mixtures to be used as references, beginning at 100% ethanol and decreasing in increments of 5% until all samples were completely non-wetted. Each element of the array was then photographed in a variety of solvents. Importantly, to ensure that the previous solvent does not affect the wetting response of the next, all samples were carefully cleaned and re-standardized in order to verify reliability of the response. Cleaning consisted of acetone and ethanol rinsing, baking at 150°C and then a further rinsing with ethanol (air drying). To verify the quality of the cleaning, all samples were re-immersed in the 100% ethanol and 90% ethanol references and their wetting patterns were verified to exactly match the patterns produced in the original reference-liquid testing stage. This indicated passing of quality control. If quality control step failed (e.g. one of the reference liquids did not produce the expected wetting pattern in the array), the cleaning process was repeated until all samples passed before continuing on to next liquid.

Data Capture

Optical images were captured using a Canon EOS Rebel T2i Digital SLR camera equipped with a macro lens, and fixed to a tripod. All images were taken under zero magnification and at roughly the same angle under consistent ambient lighting conditions. It should be noted that while all images were captured under roughly the same conditions, this is not strictly a necessary step since all subsequent analysis is based on countable differences in wettability (visualized by a shift in the rainbow pattern corresponding to the number of unfilled layers), which are independent of angle or lighting conditions.

Reference Liquid Scoring

The reference liquids used were the ethanol-water mixtures (increments of 5% volume fraction) and isopropyl alcohol (IPA). Since IPA wetted to a greater extent than 100% ethanol in all elements of the array, the set of reference liquids produced a consistent monotonic relative wetting trend. The colorimetric wetting pattern produced by a test liquid (e.g. n-octane) in each element of the array was compared to each of the reference liquids. For a given element (e.g. 5FP→13FS) if one of the reference liquids (e.g. 85% ethanol) produced an identical wetting pattern to the test liquid, then the test liquid was assigned a score corresponding to the ethanol concentration of the matching reference liquid (e.g. a score of 85). If a test liquid produced a pattern that matched none of the reference liquids, the score was interpolated to a value ending with 2 or 7. For example, if a test liquid wets more than 85% ethanol, but less than 90% ethanol, then a score of 87 would be assigned. A liquid whose wetting pattern matched IPA was assigned a score of 110. If a liquid wetted more than 100% ethanol, but less than IPA, then a score of 105 was assigned. If a liquid wetted more than IPA, a score of 115 was assigned.

Appendix B. Mathematical and Numerical Methods

B.1. Principal component analysis (for Chapter 4)

Performing a 2D principal component analysis (PCA) facilitates graphical sorting of the different liquid types by performing a mathematical optimization of a 2D projection plane that maximizes the variability in the 6D dataset of reference liquid scores. The goal is to look at the smallest number of variables that preserves most of the information from the higher-dimensional complete set of axes. The first principal component is the linear axis on which the data is projected that gives the maximum possible variance to the data set. The second principal component is the linear axis, under the constraint of being orthogonal to the first principal component axis, which maximizes the variance of the projected data. The same optimization is done for the third axis, except it must now be orthogonal to the first two, and so on (see ref [109]). The first two principal components of our system, accounting for 98% of the variance of the data, provide some insight into which elements of the array provide the most information. In the co-ordinate system of [5FP→13FS, 3FS→13FS, DEC→13FS, PTOL→13FS, TMS→13FS, 3PP→13FS], the first two principal components axes are PC1 = [0.389638, 0.448862, 0.374264, 0.393558, 0.423698, 0.414998], PC2 = [0.041843, -0.86808, 0.314051, 0.306926, 0.166533, 0.155311] (the global mean of 88.4057971 was subtracted from the whole data set to center the data before transforming to the principal component axes).

The first principal component weights all elements nearly equally. The maximum variance in this direction reflects the trend that the degree of wetting (and thus the reference liquid scores) has a general negative correlation with surface tension of the liquids for all surface chemistry combinations. The second principal component primarily looks at the contrast between the 3FS→13FS score and the scores of the non-fluorinated elements of the array (this axis is nearly orthogonal to the 5FP→13FS axis). The principal components reflect the strong degree of correlation between the scores in the DEC→13FS, PTOL→13FS, TMS→13FS and 3PP→13FS

elements of the array (indicates redundancy in these elements), and that the 3FS→13FS element provides the most distinct information from the others. This is also reflected in the qualitative similarity between the 2D 3FS→13FS vs. DEC→13FS plot (Fig. 18A) and the 2D principal component plot including all 6 elements (Fig. 18D).

B.2. Numerical percolation simulation

In this appendix, I have included a MATLAB script that calculates pore filling profiles for an IOF wetted by a liquid. This is a variant of the one used in Chapter 2 that has been commented in detail and has an added feature that allows a user to include anisotropy to the lattice (that could be caused by vertical compression during high temperature calcination). The script also lets the user input a vertical gradient of wettability described by a cumulative normal distribution with the step-height (the amount the intrinsic contact angle increases over the depth of the structure), mean and standard deviation (the latter two parameters given as depths in number of layers) as fitting parameters. The basic inputs are a distribution of neck angles (specified by a mean and standard deviation), and a list of liquids (defined by intrinsic contact angles). Anisotropy in the pore structure can be defined by giving mna_shift and sdna_shift non-zero values. These make the in-plane and out-of-plane neck angle distributions different. The outputs are FP, which stores the filling profiles by layer (percentage of the pores filled in a layer) for each liquid, and POREMAP, which stores a complete map of all filled and empty pores in the simulated lattice. It is worth noting, that since this simulation generates the spatial map of neck-angles based on a pseudo-random number generator (the 'randn' function), the POREMAP output will be different with each running of the program, while the statistics represented by the FP output will remain more or less the same (the fluctuation in the statistics from one simulation to the next can be minimized by increasing the simulation volume). The comment section at the end of the program explains the co-ordinate system used to index the fcc lattice of pores and the necks connecting them.

MATLAB Code (Pore filling simulation)

```
clear all;
close all;
```

```
%% This program has two parts: 1 connects connectivities to
% liquid/surface/pore properties. The second connects connectivities to a
% filling profile.

%% Size inputs
l=100;
t=10; %input thickness
n=16; %number of liquids

%% Define contact angle and gradients
ca=linspace(21,25,n); %contact angles
cag=zeros(t,n); %contact angle with gradient corrections

% Cumulative normal distribution to fit the gradients
% cai, mut and sigt are fitting parameters
cai=0; %contact angle increase parameter for gradients
mut=7;
sigt=3;
for tt=1:t
   cag(tt,:)=ca+cai*0.5*(1+erf((tt-mut)/(sqrt(2)*sigt)));
end


mna=19.6; %mean neck angle in degrees for inter-layer movement
mna_shift=0; % anisotropy, this is the difference between in-plane and out-of-plane
mean neck angles
sdna=3.2; %standard deviation neck angle in degrees (inter-layer movement)
sdna_shift=0; %The change in sdna for in-plane movement


%% Calculate the connectivity upfront (in-plane and out-of plane, gradients
allowed)
conn=zeros(t,n);
conn_ip=zeros(t,n);
for nn=1:n
    for tt=1:t
    % First the (out-of-plane) connectivity
    conn(tt,nn)=1-0.5*(1+erf((cag(tt,nn)-mna)/(sqrt(2)*sdna)));
    % Second the in-plane connectivity, if different
    conn_ip(tt,nn)=1-0.5*(1+erf((cag(tt,nn)-mna-
mna_shift)/(sqrt(2)*(sdna+sdna_shift))));

    end
end

%% The pore filling simulation

% Initialize output variables
% Filling profiles
FP=zeros(t,n);

% A variable to store all of the pore coordinates
```

```
POREMAP=zeros(l,l,t,n);

% The random number generator output
R=randn(l,l,t,6);

% Start the master loop (for each liquid)
for nn=1:n
    % Set the number of open and closed necks
    P=zeros(l,l,t); % Pores
    N=zeros(l,l,t,6); % Necks

    % Set the top layer of pores to be filled
    P(:,:,1)=ones(l,l);
    for pp=1:l
        for qq=1:l
            for tt=1:t
               for rr=1:6
                   if rr>3
                       % out of plane, use conn
                       if R(pp,qq,tt,rr)<sqrt(2)*erfinv(2*conn(tt,nn)-1)
                           N(pp,qq,tt,rr)=1;
                       end
                   else
                       % in plane, use conn_ip
                       if R(pp,qq,tt,rr)<sqrt(2)*erfinv(2*conn_ip(tt,nn)-1)
                           N(pp,qq,tt,rr)=1;
                       end
                   end
               end
            end
        end
    end

    % Now the next big loop where we get to fill all the pores

    % first we need to generate a counter variable zz, and a while loop
    % variable kk to run the while loop and check for infinite loops
    kk=1;
    while kk>0
        zz=0;
        for i=1:l
            for j=1:l
                for k=1:t
                    % look at each nearest neighbor, fill all pores that are
                    % connected through an open neck (N(...)=1) to a filled
                    % pore (P(...)=1

                    % Only do this if the pore is empty to start with
                    if P(i,j,k)==0

                    % Start with pores above the test pore
                    if k~=1 %no pores above the top
                        if N(i,j,k-1,4)==1
                            if P(i,j,k-1)==1
                                P(i,j,k)=1;
```

```
            end
        end

        if j~=l
        if N(i,j+1,k-1,5)==1
            if P(i,j+1,k-1)==1
                P(i,j,k)=1;
            end
        end
        else
        if N(i,1,k-1,5)==1
            if P(i,1,k-1)==1
                P(i,j,k)=1;
            end
        end
        end

        if i~=l
        if N(i+1,j,k-1,6)==1
            if P(i+1,j,k-1)==1
                P(i,j,k)=1;
            end
        end
        else
        if N(1,j,k-1,6)==1
            if P(1,j,k-1)==1
                P(i,j,k)=1;
            end
        end
        end
    end

    % Next in plane
    % using periodic boundary conditions

    % neck #1's
    if i~=l
        if N(i,j,k,1)==1
            if P(i+1,j,k)==1
                P(i,j,k)=1;
            end
        end
    else
        if N(i,j,k,1)==1
            if P(1,j,k)==1
                P(i,j,k)=1;
            end
        end
    end
    if i~=1
        if N(i-1,j,k,1)==1
            if P(i-1,j,k)==1
                P(i,j,k)=1;
            end
        end
    else
```

```
    if N(l,j,k,1)==1
        if P(l,j,k)==1
            P(i,j,k)=1;
        end
    end
end

% neck #2's
if j~=l
    if N(i,j,k,2)==1
        if P(i,j+1,k)==1
            P(i,j,k)=1;
        end
    end
else
    if N(i,j,k,2)==1
        if P(i,1,k)==1
            P(i,j,k)=1;
        end
    end
end
if j~=1
    if N(i,j-1,k,2)==1
        if P(i,j-1,k)==1
            P(i,j,k)=1;
        end
    end
else
    if N(i,l,k,2)==1
        if P(i,l,k)==1
            P(i,j,k)=1;
        end
    end
end

% Now the neck #3's N(i,j,k,3)->P(i+1,j-1,k)
% For these we will treat the exceptions separately
if i~=l
    if j~=1
        if N(i,j,k,3)==1
            if P(i+1,j-1,k)==1
                P(i,j,k)=1;
            end
        end
    else
        if N(i,j,k,3)==1
            if P(i+1,l,k)==1
                P(i,j,k)=1;
            end
        end
    end
else
    if j~=1
        if N(i,j,k,3)==1
            if P(1,j-1,k)==1
                P(i,j,k)=1;
```

```
                end
            end
        else
            if N(i,j,k,3)==1
                if P(1,l,k)==1
                    P(i,j,k)=1;
                end
            end
        end
    end

    % Now the neck #3's N(i-1,j+1,k,3)->P(i-1,j+1,k)
    % For these we will treat the exceptions separately
    if i~=1
        if j~=l
            if N(i-1,j+1,k,3)==1
                if P(i-1,j+1,k)==1
                    P(i,j,k)=1;
                end
            end
        else
            if N(i-1,1,k,3)==1
                if P(i-1,1,k)==1
                    P(i,j,k)=1;
                end
            end
        end
    else
        if j~=l
            if N(l,j+1,k,3)==1
                if P(l,j+1,k)==1
                    P(i,j,k)=1;
                end
            end
        else
            if N(l,1,k,3)==1
                if P(l,1,k)==1
                    P(i,j,k)=1;
                end
            end
        end
    end

    % Now look at pores below the test pore
    if k~=t %no pores above the top

        if N(i,j,k,4)==1
            if P(i,j,k+1)==1
                P(i,j,k)=1;
            end
        end

        if j~=1
        if N(i,j,k,5)==1
            if P(i,j-1,k+1)==1
                P(i,j,k)=1;
```

```
                        end
                    end
                    else
                    if N(i,j,k,5)==1
                        if P(i,l,k+1)==1
                            P(i,j,k)=1;
                        end
                    end
                    end

                    if i~=1
                    if N(i,j,k,6)==1
                        if P(i-1,j,k+1)==1
                            P(i,j,k)=1;
                        end
                    end
                    else
                    if N(i,j,k,6)==1
                        if P(l,j,k+1)==1
                            P(i,j,k)=1;
                        end
                    end
                    end
                end


                if P(i,j,k)==1
                    zz=zz+1;
                end

                end %onto the next pore


            end
        end
    end
    %Print zz to check function
    zz
    if zz==0
        kk=0;
    end
end

POREMAP(:,:,:,nn)=P;
for tt=1:t
    FP(tt,nn)=sum(sum(P(:,:,tt)))/(l^2);
end
end

% plot the filling profiles
figure;
x=linspace(1,t,t)';
hold on;
plot(x,FP(:,1),'k');
plot(x,FP(:,2),'b');
```

```
plot(x,FP(:,3),'m');
plot(x,FP(:,4),'g');
plot(x,FP(:,5),'c');
plot(x,FP(:,6),'r');
plot(x,FP(:,7),'y');
plot(x,FP(:,8),'k');
plot(x,FP(:,9),'k');
plot(x,FP(:,10),'b');
plot(x,FP(:,11),'m');
plot(x,FP(:,12),'g');
plot(x,FP(:,13),'c');
plot(x,FP(:,14),'r');
plot(x,FP(:,15),'y');
plot(x,FP(:,16),'k');

% plot the connectivity
figure;
y=linspace(1,n,n);
plot(conn(1,:));



%% Description of the lattice used
%lattice vectors are 1/2*{(1,1,0);(1,0,1);(0,1,1)} -->a,b,c

% coordinates for each unit cell can be in terms of abc, define a,b as the in-plane
%ones (in-plane refers to the close-packed planes that are vertically stacked in an
%IOF

% 1/2*: (110)(101)(011)(-1-10)(-10-1)(0-1-1)(1-10)(10-1)(01-1)(-110)(-101)(0-11)

% a,b,c,-a,-b,-c,b-c,a-c,a-b,c-b,c-a,b-a

%Nearest neighbors of i,j,k are: (i+1,j,k),(i,j+1,k),(i,j,k+1),(i-1,j,k),(i,j-
%1,k),(i,j,k-1),(i,j+1,k-1),(i+1,j,k-1),(i+1,j-1,k),(i,j-1,k+1),(i-1,j,k+1),(i-
%1,j+1,k)
%Neck connecting (i,j,k) to above nearest neighbors (in the same order) are:
%(i,j,k,1),(i,j,k,2),(i,j,k,4),(i-1,j,k,1),(i,j-1,k,2),(i,j,k-1,4),(i,j+1,k-
%1,5),(i+1,j,k-1,6),(i,j,k,3),(i,j,k,5),(i,j,k,6),(i-1,j+1,k,3)

%Nearest Neighbor to (i,j,k) connected by (neck coordinates)
%(i+1,j,k) --> (i,j,k,1)
%(i,j+1,k) --> (i,j,k,2)
%(i,j,k+1) --> (i,j,k,4)
%(i-1,j,k) --> (i-1,j,k,1)
%(i,j-1,k) --> (i,j-1,k,2)
%(i,j,k-1) --> (i,j,k-1,4)
%(i,j+1,k-1) --> (i,j+1,k-1,5)
%(i+1,j,k-1) --> (i+1,j,k-1,6)
%(i+1,j-1,k) --> (i,j,k,3)
%(i,j-1,k+1) --> (i,j,k,5)
%(i-1,j,k+1) --> (i,j,k,6)
%(i-1,j+1,k) --> (i-1,j+1,k,3)
```

Bibliography

1. K.J. Albert, N.S. Lewis, C.L. Schauer, G.A. Sotzing, S.E. Stitzel, T.P. Vaid, D.R. Walt, *Chem. Rev*., **100**, 2595 (2000).
2. A.W. Martinez, S.T. Phillips, G.M. Whitesides, E. Carrilho, *Anal. Chem*., **82**, 3 (2010).
3. A.W. Martinez, S.T. Phillips, M.J. Butte, G.M. Whitesides, *Angew. Chem. Int. Ed*., **46**, 1318 (2007).
4. A.W. Martinez, S.T. Phillips, E. Carrilho, S.W. Thomas, H. Sindi, G.M. Whitesides, *Anal. Chem*., **80**, 3699 (2008).
5. A.W. Martinez, S.T. Phillips, G.M. Whitesides, *Proc. Nat. Acad. Sci. U.S.A*., **105**, 19606 (2008).
6. P. Crews, J. Rodriguez, M. Jaspars, *Organic Structure Analysis* (Oxford University Press, 1998).
7. D.K. Schroder, *Semiconductor Material and Device Characterization, 3rd Ed* (John Wiley & Sons, 2006).
8. K. Wilson, J. Walker (Eds), *Principles and Techniques of Biochemistry and Molecular Biology, 6th Ed* (Cambridge University Press, 2005).
9. Z. Takats, I. Cotte-Rodriguez, N. Talaty, H. Chen, R.G. Cooks, *Chem. Commun*., 1950 (2005).
10. K. Anderson, *Cosmetics & Toiletries*, **126**, 756 (2011).
11. T. Mosmann, *J. Immunol. Meth*., **65**, 55 (1983).
12. M. Dubois, K.A. Gilles, J.K. Hamilton, P.A. Rebers, F. Smith, *Anal. Chem*., **28**, 350 (1956).
13. R. Elghanian, J.J. Storhoff, R.C. Mucic, R.L. Letsinger, C.A. Mirkin, *Science*, **277**, 1078 (1997).
14. S.S. Zumdahl, *Chemical Principles, 6th Ed*. (Houghton Mifflin Company, 2009).
15. P. Vukusic, J. R. Sambles, *Nature*, **424**, 852 (2003).
16. J.D. Joannopoulos, S.G. Johnson, J.N. Winn, R.D. Meade, *Photonic Crystals: Molding the Flow of Light, 2nd Ed.* (Princeton University Press, 2008).

17. Y.M. Zheng, X.F. Gao, L. Jiang, *Soft Matter*, **3**, 178 (2007).

18. O. Sato, S. Kubo, Z.Z. Gu, *Acc. Chem. Res*., **42**, 1 (2009).

19. Y. Fang, G. Sun, Q. Cong, G.-H. Chen and L.-Q. Ren, *Journal of Bionic Engineering*, **5**, 127 (2008).

20. C.I. Aguirre, E. Reguera, A. Stein, *Adv. Funct. Mater*., **20**, 2565 (2010).

21. R.C. Schroden, M. Al-Daous, C.F. Blanford, A. Stein, *Chem. Mater.*, **14**, 3305 (2002).

22. K.A. Arpin, A. Mihi, H.T. Johnson, A.J. Baca, J.A. Rogers, J.A. Lewis, P.V. Braun, *Adv. Mater*., **22**, 1084 (2010).

23. J.H. Fendler, F.C. Meldrum, *Adv. Mater*., **7**, 607 (1995).

24. A. van Blaaderen, R. Ruel, P. Wiltzius, *Nature*, **385**, 321 (1997).

25. Y.N. Xia, B. Gates, Y.D. Yin, Y. Lu, *Adv. Mater*., **12**, 693 (2000).

26. G. Subramanian, V.N. Manoharan, J.D. Thorne, D.J. Pine, *Adv. Mater.*, **11**, 1261 (1999).

27. A.C. Arsenault, T.J. Clark, G. von Freymann, L. Cademartiri, R. Sapienza, J. Bertolotti, E. Vekris, S. Wong, V. Kitaev, I. Manners, R.Z. Wang, S. John, D. Wiersma, G.A. Ozin, *Nature Materials*, **5**, 179 (2006).

28. S.V. Boriskina, S. Y. K. Lee, J. J. Amsden, F. G. Omenetto, L. Dal Negro, *Opt. Express*, **18**, 14568 (2010).

29. J. J. Amsden, H. Perry, S. Boriskina, D. L Kaplan, L. Dal Negro, F. G. Omenetto, *Opt. Express*, **17**, 21271 (2009).

30. H. Fudouzi, and Y. Xia, *Adv. Mater.*, **15**, 892 (2003).

31. J.E. Smay, J. Cesarano III, J.A. Lewis, *Langmuir*, **18**, 5429 (2002).

32. H. Kim, J. Ge, J. Kim, S. Choi, H. Lee, H. Lee, W. Park, Y. Yin, S. Kwon, *Nature Photonics* **3**, 534 (2009).

33. A.M. Brozell, M.A. Muha, A. Abed-Amoli, D. Bricarello, and A.N. Parikh, *Nano Letters*, **7**, 3822 (2007).

34. R.A. Potyrailo, H. Ghiradella, A. Vertiatchikh, K. Dovidenko, J.R. Cournoyer, E. Olson, *Nature Photonics*, **1**, 123 (2007).

35. L.D. Bonifacio, D.P. Puzzo, S. Breslav, B.M. Willey, A. McGreer, G.A. Ozin, *Adv. Mater*., **22**, 1351 (2010).

36. M.C. Janzen, J.B. Ponder, D.P. Bailey, C.K. Ingison, K.S. Suslick, *Anal. Chem*., **78**, 3591 (2006).

37. J.T. Zhang, L. Wang, J. Luo, A. Tikhonov, N. Kornienko, S.A. Asher, *J. Am. Chem. Soc*., **133**, 9152 (2011).

38. K. Lee, S.A. Asher, *J. Am. Chem. Soc*., **122**, 9534 (2000).

39. J.H. Holtz, S.A. Asher, *Nature*, **389**, 829 (1997).

40. O.L.J. Pursiainena, J.J. Baumberg, K. Ryan, J. Bauer, H. Winkler, B. Viel, T. Ruhl, *Appl. Phys. Lett*., **87**, 101902 (2005).

41. Y.J. Lee, P.V. Braun, *Adv. Mater*., **15**, 563 (2003).

42. Y. Takeoka, M. Honda, T. Seki, M. Ishii, and H. Nakamura, *ACS Applied Materials and Interfaces* **1,** 982 (2009)

43. T. Endo, Y. Yanagida, T. Hatsuzawa, *Sensors and Actuators B*, **125**, 589 (2007).

44. Y.J. Lee, S.A. Pruzinsky, P.V. Braun, *Langmuir*, **20**, 3096 (2004).

45. J.M. Weissman, H.B. Sunkara, A.S. Tse, S.A. Asher, *Science*, **274**, 959 (1996).

46. A.C. Arsenault, D.P. Puzzo, I. Manners, G.A. Ozin, *Nature Photonics*, **1**, 468 (2007).

47. A.C. Arsenault, H. Miguez, V. Kitaev, G.A. Ozin, I. Manners, *Adv. Mater*., **15**, 503 (2003).

48. J. Kobler, B.V. Lotsch, G.A. Ozin, T. Bein, *ACS Nano*, **3**, 1669 (2009).

49. A.C. Arsenault, V. Kitaev, I. Manners, G.A. Ozin, A. Mihi, H. Miguez, *J. Mater. Chem.*, **15**, 133 (2005).

50. V.L. Alexeev, A.C. Sharma, A.V. Goponenko, S. Das, I.K. Lednev, C.S. Wilcox, D.N. Finegold, S.A. Asher, *Anal. Chem.*, **75**, 2316 (2003).

51. A.C. Sharma, T. Jana, R. Kesavamoorthy, L.J. Shi, M.A. Virji, D.N. Finegold, S.A. Asher, *J. Am. Chem. Soc.*, **126**, 2971 (2004).

52. R.A. Barry, P. Wiltzius, *Langmuir*, **22**, 1369 (2006).

53. S. Colodrero, M. Ocana, H. Miguez, *Langmuir*, **24**, 4430 (2008).

54. H. Fudouzi, T. Sawada, *Langmuir*, **22**, 1365 (2006).

55. J.P. Ge, J. Goebl, L. He, Z.D. Lu, Y.D. Yin, *Adv. Mater.*, **21**, 4259 (2009).

56. J.Y. Wang, Y. Cao, Y. Feng, F. Yin, J. Gao, *Adv. Mater.*, **19**, 3865 (2007).

57. F. Fleischhaker, A.C. Arsenault, F.C. Peiris, V. Kitaev, I. Manners, R. Zentel, G.A. Ozin, *Adv. Mater.*, **18**, 2387 (2006).

58. K. Busch, S. Lolkes, R.B. Wehrspohn, H. Foll, in *Photonic Crystals, Advances in Design, Fabrication and Characterization*, (Wiley-VCH, 2004).

59. B.D. Hatton, L. Mishchenko, S. Davis, K.H. Sandhage, J. Aizenberg, *Proc. Natl. Acad. Sci., U.S.A.*, **107**, 10354 (2010).

60. J.-T. Lee, M.C. George, J.S. Moore, P.V. Braun, *J. Am. Chem. Soc.*, **131**, 11294 (2009).

61. M.-H. Lin, C.-F. Chen, H.-W. Shiu, C.-H. Chen, and S. Gwo, *J. Am. Chem. Soc.*, **131**, 10984 (2009).

62. P.G. de Gennes, F. Brochard-Wyart, D. Quere, *Capillarity and Wetting Phenomena* (Springer, 2004).

63. A. Tuteja, W. Choi, J.M. Mabry, G.H. McKinley, R.E. Cohen, *Proc. Natl. Acad. Sci. U.S.A.*, **105**, 18200 (2008).

64. R.A. Potyrailo, K. Rajan, K. Stoewe, I. Takeuchi, B. Chisholm, H. Lam, *ACS Comb. Sci*., **13**, 579 (2011).

65. M.C. Lonergan, E.J. Severin, B.J. Doleman, S.A. Beaber, R.H. Grubbs, N.S. Lewis, *Chem. Mater*. **8**, 2298 (1996).

66. C.T. Clelland, V.Risca, C. Bancroft, *Nature*, **399**, 533 (1999).

67. D. Marguiles, C.E. Felder, G. Melman, A. Shanzer, *J. Am. Chem. Soc*., **129**, 347 (2007).

68. S.W. Thomas, R.C. Chiechi, C.N. Lafratta, M.R. Webb, A. Lee, B.J. Wiley, M.R. Zakin, D.R. Walt, G.M. Whitesides, *Proc. Natl. Acad. Sci., U.S.A.*, **106**, 9147 (2009).

69. J. Sagiv, *J. Am. Chem. Soc*., **102**, 92 (1980).

70. R.K. Smith, P.A. Lewis, P.S. Weiss, *Prog. Surf. Sci*., **75**, 1 (2004).

71. M.J. Lercel, H.G. Craighead, K. Parikh, K.Seshadri, D.L. Allara, *Appl. Phys. Lett.*, **68**, 1504 (1996).

72. R.D. Piner, J. Zhu, F. Xu, S.H. Hong, C.A. Mirkin, *Science*, **283**, 661 (1999).

73. J.-T. Lee, M.C. George, J.S. Moore, P.V. Braun, *J. Am. Chem. Soc.*, **131**, 11294 (2009).

74. T. Rohr, E.F. Hilder, J.J. Donovan, F. Svec, J.M.J. Frechet, *Macromolecules*, **36**, 1677 (2003).

75. K.A. Mirica, S.T. Phillips, S.S. Shevkoplyas, G.M. Whitesides, *J. Am. Chem. Soc.*, **130**, 17678 (2008).

76. K.A. Mirica, S.S. Shevkoplyas, S.T. Phillips, M. Gupta, G.M. Whitesides, *J. Am. Chem. Soc.*, **131**, 10049 (2009).

77. C.D. Lorenz, R.M. Ziff, *Phys. Rev. E*, **57**, 230 (1998).

78. M. Prat, *International Journal of Multiphase Flow*, **19**, 691 (1993).

79. B.V. Derjaguin, *Theory of stability of colloids and thin films* (Plenum, 1989).

80. C. Collins, *Methods in Biotechnology*, **23**, 99 (2007).

81. W.M. Haynes (Ed.), *CRC Handbook of Chemistry and Physics 92nd Ed.* (CRC Press, 2011).

82. I.M. Eastwood, E. Dorland, M.S. Al-Jafari, D.M. Goodall, E.T. Bergstrom, U.S. Patent No. 7,919,325 (2011).

83. Z.Z. Gu, A. Fujishima, O. Sato, *Chem. Mater.*, **14**, 760 (2002).

84. P. Jiang, M.J. McFarland, *J. Am. Chem. Soc.*, **126**, 13778 (2004).

85. Y.D. Yin, Y. Lu, B. Gates, Y.N. Xia, *J. Am. Chem. Soc*. **123**, 8718 (2001).

86. J. Aizenberg, A.J. Black, G.M. Whitesides, *Nature* **398**, 495 (1999).

87. G.M. Whitesides, B. Grzybowski, *Science* **295**, 2418 (2002).

88. I. Weissbuch, L. Addadi, M. Lahav, L. Leiserowitz, *Science* **253**, 637 (1991).

89. J.P. Yang, F.C. Meldrum, J.H. Fendler, *J. Phys. Chem*. **99**, 5500 (1995).

90. C.D. Bain, E.B. Troughton, Y.T. Tao, J. Evall, G.M. Whitesides, R.G. Nuzzo, *J. Am. Chem. Soc*. **111**, 321 (1989).

91. A. Ulman, *Chemical Reviews* **96**, 1533 (1996).

92. A. Sayari, S. Hamoudi, *Chem. Mater.*, **13**, 3151 (2001).

93. B. Hatton, K. Landskron, W. Whitnall, D. Perovic, G.A. Ozin, *Acc. Chem. Res.*, **38**, 305 (2005).

94. R. Xuan, J. Ge, *Langmuir*, **27**, 5694 (2011).

95. M.A. Palacios, E. Benito-Pena, M. Manesse, A.D. Mazzeo, C.N. LaFratta, G.M. Whitesides, D.R. Walt, *Proc. Natl. Acad. Sci., U.S.A*, **108**, 16510 (2011).

96. M. Deubel, M. Wegener, S. Linden, G. von Freymann, S. John, *Opt. Lett.*, **31**, 805 (2006).

97. A. Chutinan, S. John, O. Toader, *Phys. Rev. Lett.*, **90**, 123901 (2003).

98. A. Chutinan, S. John, *Phys. Rev. E*, **71**, 026605 (2005)

99. L. Tang, T. Yoshie, *Opt. Lett.*, **35**, 3144 (2010).

100. N. Tetrault, A. Mihi, H. Miguez, I. Rodriguez, G.A. Ozin, F. Meseguer, V. Kitaev, *Adv. Mater.*, **16**, 346 (2004).

101. T.M. Babinec, J.T. Choy, K.J.M. Smith, M. Khan, M. Lončar, *J. Vac. Sci. Technol. B*, **29**, 010601 (2011).

102. B.H. Cumpston, S.P. Ananthavel, S. Barlow, D.L. Dyer, J.E. Ehrlich, L.L. Erskine, A.A. Heikal, S.M. Kuebler, I.-Y. Sandy Lee, D. McCord-Maughon, J. Qin, H. Röckel, M. Rumi, X.-L. Wu, S.R. Marder, J.W. Perry, *Nature*, **398**, 51 (1999).

103. A. Blanco, E. Chomski, S. Grabtchak, M. Ibisate, S. John, S.W. Leonard, C. Lopez, F. Meseguer, H. Miguez, J.P. Mondia, G.A. Ozin, O. Toader, H.M. van Driel, *Nature*, **405**, 437 (2000).

104. S.A. Rinne, F. Garcia-Santamaria, P.V. Braun, *Nature Photonics*, **2**, 52 (2008).

105. B.D. Hatton, V. Kitaev, D. Perovic, G.A. Ozin, J. Aizenberg, *J. Mater. Chem.*, **20**, 6009 (2010).

106. M. Rapp, W.A. Ducker, *J. Am. Chem. Soc.*, **132**, 18051 (2010).

107. T.S. Wong, S.H. Kang, S.K.Y. Tang, E.J. Smythe, B.D. Hatton, A. Grinthal, J. Aizenberg, *Nature*, **447**, 443 (2011).

108. W. Wang, I.B. Burgess, B.D. Hatton, J. Alvarenga, J. Aizenberg, submitted (2012)

109. I.T. Jolliffe *Principal Component Analysis*, *2nd ed*., (Springer, NY, 2002).